NELSON MANDELA

UNIVERSITY

RESEARCH THESIS FOR:

Strain behaviour of an eco-car wheel rim designed through topology and composite layup optimization

SUBMITTED TO:

FACULTY OF ENGINEERING, THE BUILT ENVIRONMENT AND INFORMATION TECHNOLOGY

OF THE

NELSON MANDELA UNIVERSITY

FOR THE PROPOSED RESEARCH PROGRAMME:

Magister in Ingeniaria: MEng Mechanical

BY:

Martin Wessel Badenhorst

210000449

Submitted: July 2017

Supervisor: Prof H. Lombard

Co-supervisor: Prof R. Phillips

Declaration of academic integrity

Student Name:	Martin Wessel Badenhorst
Student Number:	210000449
Module Name and Code:	Magister in Ingeniaria: MEng Mechanical
Date:	31 July 2017

- I am aware of the Nelson Mandela University policy regarding the Promotion of Academic Integrity and Prevention of Plagiarism.

- I understand what plagiarism is and I know that it constitutes unacceptable academic behaviour.

- I declare that the work that I am submitting herewith is my own work. In so far as I have made use of other people's work, it has been duly acknowledged and properly referenced in accordance with departmental guidelines and prescriptions.

- I have not allowed, and will not allow, anyone to copy my work with the intention of passing it off as their own work.

Conferences:

Presented at the 9th European *ATC* (*Altair Technology Conference*) in Frankenthal, Germany on 26th – 28th June 2017.

SIGNATURE:

Abstract

Author: Martin Wessel Badenhorst

Title: Strain behaviour of an eco-car wheel rim designed through
               topology and composite layup optimization

This research aimed to reduce the mass of a purpose built eco-car wheel through the sequential use of structural topology and composites optimization software packages while investigating the changes in mass and strain behaviour resulting from altering component geometry, lamina shape, and stacking sequence.

The strain behaviour of a commercially available wheel constructed using pre-tensioned steel spokes was established through the comparison of measured physical and *FEA* strains resulting from applied pressure, radial, lateral, torsional, and combined loads.

Structural topology optimization software was then utilized to produce 48 different wheel geometries corresponding to a combined loading scenario consisting of pressure, radial, and lateral loads. The variables controlled during this process included the objective optimization function, safety factor, target design volume, split-draw constraint, and degrees of cyclic symmetry. The optimum geometry was determined by means of evaluating specific stiffness and potential towards being manufactured as a composite component.

Three composite wheel *FEA* base models, with uni-directional laminae stacked at different fibre orientation intervals, were created according to this geometry and lightened by means of composite free size optimization. Composite sizing and shuffling optimizations were then utilized to further enhance the mass and strain characteristics of the lightest of these three solutions

Two composite wheels were manufactured according to the wheel geometry, lamina shapes, and stacking sequences determined by means of structural topology and composites optimizations.

The physical mass and strain behaviour of these wheels were measured and compared to those corresponding to the optimized *FEA* model, as well as the commercially available wheel.

This comparison showed that structural topology and composites optimization software packages can be sequentially utilized to produce an adequately stiff composite wheel of lower mass than a commercially available wheel constructed using pre-tensioned steel spokes.

Table of contents

List of figures

List of tables

Glossary of terms

A

Altair® HyperWorks®: A simulation and optimization software platform for various engineering applications

Anisotropic material: A material having properties that vary with orientation [1]

B

Breather-bleeder: A non-woven synthetic fibre material used to absorb excess resin from an uncured composite laminate through a porous peel-ply or release film

C

Combined loading: A state of loading consisting of multiple individual loading mechanisms

Composite material: A material formed by the combination of two or more distinct materials to form a new material with enhanced properties [1]

Compression: A pushing force [2]

Cyclic symmetry: A symmetry condition where a pattern is seen to be repeated sequentially about an axis [3]

D

Dassault Systèmes® SolidWorks®: A solid modelling and simulation software platform for various engineering applications

Degrees of freedom: A variable used to describe the translational and rotational behaviour of a node [3]

Discretization: The division of geometry into nodes and elements [3]

E

Elastic: A deformation with complete rebound [2]

Elastic modulus: A ratio describing the relationship between axial stress and normal strain in a linear elastic material before the initiation of yielding [4]

F

Finite element analysis: a software based design tool utilized to predict the response of a system to some forcing function [5]

Finite element method: A method which produces approximate solutions to partial differential equations describing the behaviour of a system [5]

H

Hand-layup: A method of composite manufacturing involving the manual wetting of reinforcement material with a matrix [6]

I

Isotropic material: A material with the same mechanical properties in three mutually perpendicular directions [3]

M

Matrix material: A material which holds the reinforcement fibres of a composite material together in a structural unit [7]

O

Orthotropic: A material having three orthogonal planes of symmetry that coincide with the coordinate planes [1]

P

Peel-ply: The porous first layer that goes against an uncured composite laminate to bleed excess resin and evacuate solvents [6]

Poisson coefficient: A negative ratio between transverse and longitudinal strains [8]

Pressure loading: An evenly distributed force acting normal to a surface

S

Safety factor: A ratio between the failure load and allowable load [9]

Shear modulus: A ratio describing the relationship between shear stress and shear strain in a linear elastic material before the initiation of yielding [4]

Stiffness: A ratio describing force per unit deformation [2]

Strain: A ratio describing the change in length between two points relative to the original length between them

Strain gage: A carrier that is attached by bonding to a base material so that the resistance of the element will vary as the surface of the base material to which it is attached is deformed [10]

Stress: A ratio defining force per unit of cross sectional area [2]

Structural topology optimization: The determination of features such as the number, location, and shape of holes and connectivity within a domain [11]

T

Trace: The sum of the terms which exist on the primary diagonal of a matrix [12]

Tyre-ground contact patch: The area of contact which exists between a tyre and the ground [13]

V

Vacuum bag: A polyvinyl alcohol film used as a vacuum membrane that is sealed at the edges or to the mould itself [6]

Validity: The accuracy with which a physical problem represents reality [3]

Von-Mises failure criterion: A method of predicting when a material can be considered to have failed [3]

W

Wheel: A load bearing vehicular component consisting of a hub, spokes or disc, and rim

Wheel rim: The circumferential edge of a wheel to which a tyre is seated

Y

Yield strength: The allowable stress in a material above which yielding will occur [9]

Yielding: A breakdown of material resulting in permanent deformation [9]

Nomenclature

E_1 - Elastic modulus in fibre direction (in tensorial notation)

E_2 - Elastic modulus transverse to fibre direction (in tensorial notation)

E_{ad} - Allowable stiffness tensors to structural topology optimization

E_e - Element stiffness

E_{xy} - Stiffness tensor assigned to an element

$E^0{}_{xy}$ - Stiffness tensor of an assigned isotropic material

E_{xy} - Stiffness function

$E_{xy}(x)$ - Domain stiffness tensor

F_{2t} - Transverse tensile strength of a composite lamina

F_{cgl} - Centrifugal force experienced by the vehicle

F_{cpl} - Centripetal force experienced by the vehicle

F_N - Normal force experienced by the wheel

F_r - Vehicle weight supported by wheel

F_{rr} - Force required to overcome rolling resistance

G_{12} - Shear Modulus (in tensorial notation)

G_{Ic} - Fracture toughness

$\boldsymbol{K}$ - Domain stiffness matrix

$\boldsymbol{K}_e$ - Stiffness of an element, e

N - Sprocket Ratio

NE - Total number of elements

Np - Total number of super-plies

P_j - Percentage of a single fibre orientation in a laminate

Q_{ij} - Component of the stiffness matrix Q

$Q_{ij}{}^*$ - Component of the stiffness belonging to a master ply

$\mathbb{R}^2$ - Two-dimensional space

$\mathbb{R}^3$ - Three-dimensional space

T_{EO} - Maximum torque produced by engine

T_{fw} - Maximum torque experienced by a front wheel

T_k - Laminate thickness

T_{RW} - Maximum torque experienced by rear wheel

Tr - Trace of the stiffness matrix Q

U - Allowable kinematic displacement fields to structural topology optimization

V - Maximum volume of permissible material within Ω

V_f - Reinforcement fibre volume fraction

V_m - Matrix volume fraction

X_{ik} - Thickness of the ith super-ply of the kth element

a_p - Centripetal acceleration

$a(u, v)$ - Energy bilinear form of an elastic body

e - Finite element

$\boldsymbol{f}$ - Domain load vector

f - Internal body forces in Ω

f_r - Coefficient of rolling resistance

$f(x)$ - Objective function (general form)

g - Gravitational constant of acceleration

$l(u)$ - Load linear form

m_v - Mass of the vehicle

m_w - Mass supported by the wheel

p - Penalization factor

r - Radius

t - Surface tractive forces applied to Γ_T

t_t - Transition thickness of carbon-epoxy composites

$\boldsymbol{u}$ - Domain displacement vector

(u) - State of equilibrium

v - Linear velocity of the vehicle

(v) - Virtual displacement

Γ_T - Boundary of the domain Ω

Ω - Design space to be optimized during structural topology optimization

Ω^{mat} - Subdomain representing the presence of solid isotropic material

Ω^{void} - Subdomain representing the absence of solid isotropic material

$\varepsilon_x(u)$ - Linearized strain of the energy bilinear form

$\varepsilon_y(v)$ - Linearized strain of the energy bilinear form

θ - Wheel camber angle

μ - Coefficient of friction between the tyres and road

v^0 - Poisson coefficient of the assigned isotropic material

v_{12} - Poisson coefficient (in tensorial notation)

ρ_f - Mass density of the reinforcement fibres only

ρ_m - Mass density of the matrix only

ρ_{min} - Minimum admissible material presence density

ρ_{ply} - Lamina mass density

$\rho(x)$ - Material presence density

$\varnothing_w$ - Wheel diameter

Abbreviations

AMTC - Advanced Mechatronics Training Centre

ASTM - American Society for Testing and Materials

ATC   - Altair Technology Conference

DMO   - Discrete Material Optimization

FAA   - Federal Aviation Administration

FEA   - Finite Element Analysis

FEM   - Finite Element Method

RBE   - Rigid Body Element

SEM   - Shell Eco Marathon

SIMP - Solid Isotropic Material with Penalization

WRM - Weighted Residual Method

Chapter 1: Research proposal

1.1 Introduction

The improvement of mechanical designs is an ongoing process which promotes the competitive business practice and technological innovation to satisfy necessity dictated by global industry. Improvements are continuously being made to mechanical processes and components to enhance their efficiency and functionality.

This study investigated material strain and mass reduction achieved through the sequential application of structural topology and composites optimization techniques to a purpose built wheel which could be utilized on the *Nelson Mandela University Eco Car*. Consequently, the *FEA* strain behaviour of an optimized composite wheel designed in this way was compared against corresponding physical strain measurements obtained through manufacturing and testing.

This study expected to yield results which could be beneficial to the *Nelson Mandela University* by enhancing the performance of the *Nelson Mandela University Eco Car Project*, and providing the *Nelson Mandela University* with additional knowledge to serve local industry in the improvement of component design through structural topology and composites optimizations.

1.2 *Nelson Mandela University Eco Car Project*

The *Nelson Mandela University Eco Car Project* was established in 2014 under the *AMTC* (*Advanced Mechatronics Training Centre*), an engagement unit based within the *Nelson Mandela University*. The aim of this project was to design and manufacture a lightweight prototype vehicle, referred to as the *Nelson Mandela University Eco Car* (shown in *Figure 1*), which could compete in the first *Shell Eco Marathon (SEM)* event held in Africa.

Figure 1 – 2016 *Nelson Mandela University Eco Car* (Side view)

During this event, various African universities competed against one another in a fuel efficiency based race to determine which vehicle could travel the furthest distance on an equivalent 1 litre of petrol. The success of this event, held at *Zwartkops Raceway* (Pretoria) during October 2015, resulted in *Shell* running it on an annual basis in South Africa.

The *Nelson Mandela University Eco Car Team* spent 2016 improving the efficiency of the *Nelson Mandela University Eco Car* by reducing its mass and optimizing its engine performance. This resulted in the *Nelson Mandela University Eco Car Team* winning the prototype-gasoline category of the *2016 SEM: Africa* by achieving a fuel consumption of 127.86 km.l^{-1}. Currently (2017), the *Nelson Mandela University Eco Car Team* is attempting to improve this fuel efficiency by utilizing various structural optimization techniques to reduce the mass of components within the *Nelson Mandela University Eco Car*.

1.3 Aim and objectives

The primary aim of this research was to sequentially utilize structural topology and composites optimization software packages to reduce the mass of a purpose built eco-car wheel while investigating the changes in structural integrity resulting from altering component geometry, lamina shape, and stacking sequence.

Supporting objectives:

I. Design and manufacture a combined static load test rig to determine physical strains induced by actual loadings for the purpose of calibrating computational analyses.

II. Produce a topologically optimized alloy component of adequate stiffness which will not fail when subject to load.

III. Design and manufacture a multi-part mould for composite component fabrication.

IV. Produce a composite component of equivalent geometry which will not fail when subject to the same load.

1.4 Significance and feasibility of research

This research sought to contribute towards the knowledge base of the *Nelson Mandela University* to better assist local industry in the practice of efficient component design by reducing component material quantity, mass, and cost.

The results obtained through this research also aimed to benefit local industry by contributing towards the establishment of a high-end knowledge base in the design and analysis of composite components.

Enhancing the local high-end knowledge base pertaining to composite materials and component design optimization will aid South Africa in becoming an established global competitor in the field of product design and fabrication. This will, in turn, promote economic growth by reducing the amount of international outsourcing currently required by local businesses, and aid in the development of job creation through the expansion of local industry.

1.5 Delimitations

The following delimitations were applied in this dissertation:

I.   The wheel was to be capable of seating a tubeless *Michelin 45/75 R16* tyre as well as a standard tube-type bicycle tyre

II.   Failure of the optimized composite wheel was analysed with respect to an internal tyre pressure of 700 kPa as based on the use of *Michelin 45/75 R16* tyres

III.   Optimization was performed according to a tyre pressure of 200 kPa as per the normal bicycle tyres utilized on the *Nelson Mandela University Eco Car*

IV.   All loadings were taken as the anticipated worst case owing to no standards existing for the design of wheels to be used in the *Shell Eco Marathon*

V.   *Dassault Systèmes SolidWorks, solidThinking Inspire*, and *Altair HyperWorks* were utilized for all computational analysis and optimization processes

VI.   The damping effect of the tyre were not included in software based analyses and optimizations

VII.   All *FEA* results assumed perfect component geometry and manufacture

VIII.   All composite components were manufactured by means of hand-layup and vacuum bagging techniques

IX.   All composite components were manufactured using uni-directional carbon fibre embedded in an epoxy resin matrix

X.   The minimum variation of lamina fibre orientation angle was 15°

1.6 Hypothesis

The sequential use of computational structural topology and composites optimization software will produce a purpose built composite wheel design which is at least 10 percent stiffer and 15 percent lighter than a standard 16" alloy bicycle wheel, and will able to withstand the loadings induced by the *Nelson Mandela University Eco Car* at 45 [km.h^{-1}].

1.7 Problem statement

Design of weight critical, highly loaded composite components using traditional methods can in certain instances be sub-optimal. This research investigates systematic topology design optimisation techniques.

1.8 Sub-problems

The sub-problems contributing towards meeting the primary objective of this study are outlined in this section.

1.8.1 Formulation of wheel loading

The design of any mechanical component requires an accurate understanding of both the nature and magnitude of each applied load which it is intended to experience. In this dissertation, the forces acting on each wheel of the *Nelson Mandela University Eco Car* were determined by means of analytical calculation accounting for both acceleration during a pit line start, and cornering. Currently, no standards exist to govern the design of purpose built eco-car wheels.

1.8.2 Verification of computational analysis

The validity any software based analysis or optimization depends on how accurately the model represents reality. In this dissertation, a static load test rig was built in order to physically load a strain gaged 16" alloy wheel rim for the purpose of comparing measured physical strains to corresponding *FEA* strains. Poor correlation between physical and computational strains would have

resulted in a re-evaluation of the input constraints, loading, and discretization utilized in the computational analysis.

1.8.3 Formulation of boundary conditions

The results produced by using an optimization software package depend on the boundary conditions specified by the user. In this dissertation, boundary conditions were applied as split draw constraints to the wheel base model subjected to structural topology optimization. This ensured that that the produced wheel designs could be manufactured as composite components by means of hand-layup and vacuum bagging techniques.

1.8.4 Influence of ambient room conditions on manufacture

The ambient room conditions during composite layup were controlled to appropriate temperature and humidity so as to not hinder the structural integrity of the manufactured wheels. Wall mounted air-conditioning units were used to maintain constant ambient room conditions. It was important that all composite layups were performed under identical ambient room conditions to allow for a fair comparison between the manufactured composite wheels.

1.9 Research process

The experimental process followed in this research started with a computational analysis of the commercially available wheels currently used on the *Nelson Mandela University Eco Car*. This process involved the physical measurement of strains induced by operational loading for the purpose of calibrating computational input and physical testing methods.

Structural topology optimization software was then utilized to determine an optimum wheel geometry based on the critical load paths created by normal operation. The resultant mass and induced strains were investigated and noted.

A composite wheel was then designed according to the optimum geometry to serve as a base model for the comparison of mass and strain against each stage of composites optimization. The composite layup optimization

investigated the changes in component mass and strain as a result of optimizing the ply thickness, ply shape, and stacking sequence individually. The optimized result was then physically manufactured and tested to investigate the comparison between measured physical and *FEA* masses and strains. This process is illustrated in *Figure 2*.
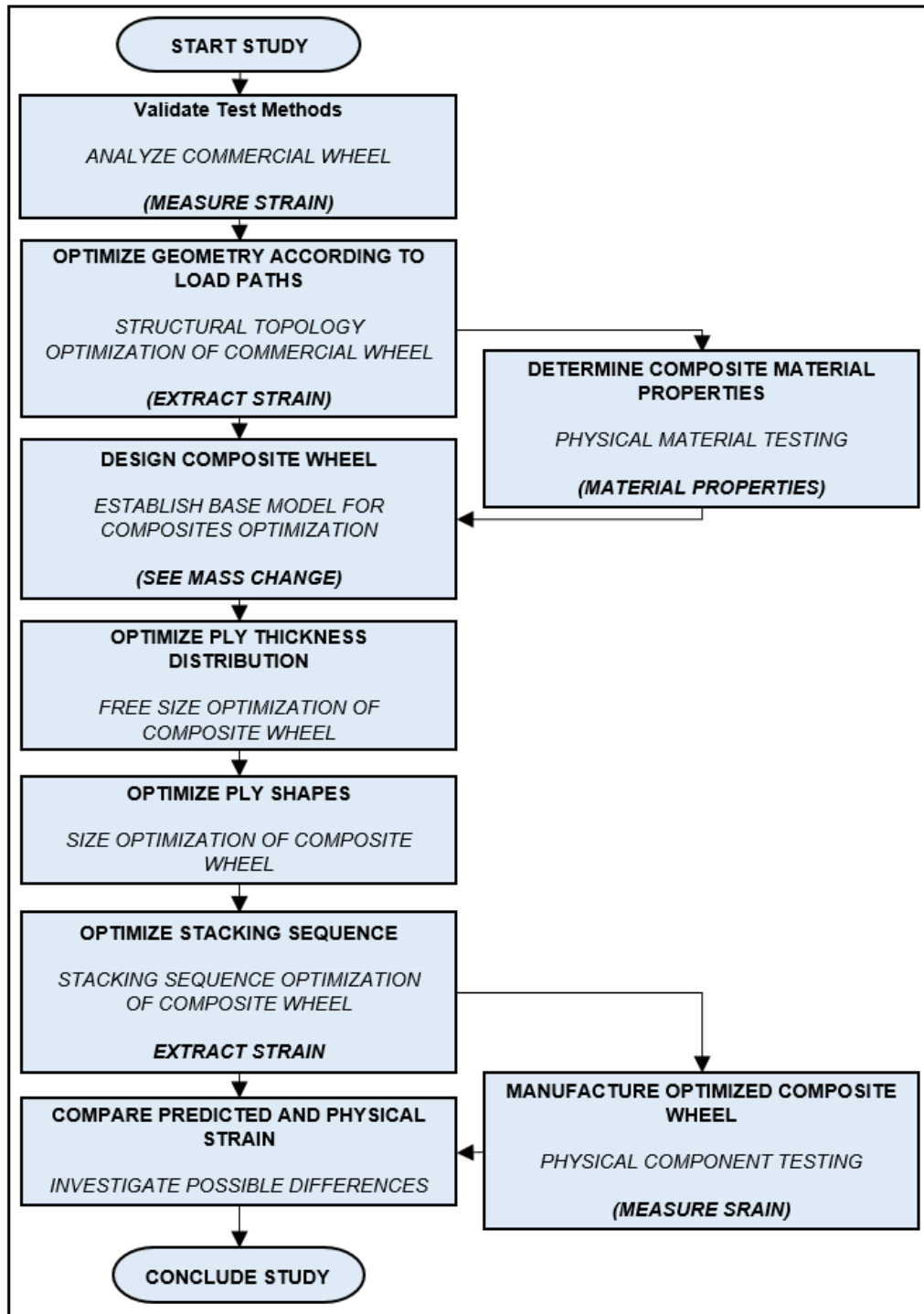
Figure 2 - Research process outline

1.10 Research project plan

The schedule adhered to during the completion of this study is shown in *Figure 3*. The critical project path is shown in red. Successful completion of this project required that all critical tasks be completed according to schedule.

	Task Name	Duration	Start	Finish	Predecessor
1	Literature Review	70 days	Tue 16-01-05	Fri 16-04-22	
2	Design Test Rig	20 days	Tue 16-01-05	Thu 16-02-04	
3	Build Test Rig	20 days	Fri 16-02-05	Tue 16-03-08	2
4	FEA Correlation Testing	20 days	Tue 16-03-08	Thu 16-04-07	3;20
5	Optimization (TL)	5 days	Fri 16-04-08	Fri 16-04-15	4
6	Computational Model + FEA	5 days	Fri 16-04-15	Mon 16-04-25	5
7	Composite Wheel Rim Design	20 days	Fri 16-04-15	Wed 16-05-18	5
8	Mould Design	5 days	Wed 16-05-18	Wed 16-05-25	7
9	Optimization (BL)	5 days	Wed 16-05-25	Thu 16-06-02	8
10	Modelling & Analysis	20 days	Thu 16-06-02	Mon 16-07-04	9
11	Opt. Comp. Manufacture	2 days	Mon 16-07-04	Thu 16-07-07	10
12	Opt. Comp. Testing	3 days	Thu 16-07-07	Tue 16-07-12	11
13	Dissertation & Editing	55 days	Tue 16-07-12	Thu 16-10-06	16;12;18;1
14	Mould Manufacture	10 days	Wed 16-05-25	Thu 16-06-09	8
15	Composite Wheel Manufacture	2 days	Fri 16-06-10	Tue 16-06-14	14
16	Composite Wheel Testing	3 days	Tue 16-06-14	Fri 16-06-17	15
17	Manufacture (Alloy Rim)	30 days	Fri 16-04-15	Thu 16-06-02	5
18	Metallic Wheel Testing	3 days	Thu 16-06-02	Tue 16-06-07	17
19	Computational Modelling	10 days	Tue 16-01-05	Wed 16-01-20	
20	Load Formulation	30 days	Wed 16-01-20	Mon 16-03-07	19

Figure 3 - Gantt chart outlining research project schedule

1.11 Project budget

The estimated project cost is outlined in *Table 1.*

Table 1 - Estimated project budget

Project Budget		
Item	**Details**	**Projected Cost**
Administration	Application Fee	R 260,00
	Registration Fee	R 950,00
Software	Altair (250HWU for 1x Year]	R 15 000,00
	3x consecutive one-on-one courses	R 10 000,00
Testing	Strain Gauges & Testing materials	R 5 000,00
	Static Test Rig	R 3000,00
Manufacture	Base Wheel Manufacture (Metallic]	R 10 000,00
	Multi-Part Mould (All Composite Manufacture]	R 10 000,00
	Initial Composite Wheel Manufacture	R 3000,00
	Optimized Composite Wheel Manufacture	R 3000,00
Submission	Journal Submission Fee	--
	Printing & Binding	R 2000,00
Total Including Already Procured Items		**R 62 210,00**

1.12 Researcher's qualifications

I.   Baccalaureus Technologiae Mechanical Engineering (BTech Mech Eng), Nelson Mandela Metropolitan University-2015

II.   National Diploma Mechanical Engineering (NDip Mech Eng), Nelson Mandela Metropolitan University-2013

Chapter 2: Literature review

2.1 Introduction

The intention of this chapter is to provide a summary of the critical theory and literature relevant to the design of a purpose built eco-car wheel by means of sequentially applied structural topology and composites optimization techniques. As such, the reviewed theory and literature presented in this chapter focuses on the fields of wheel design, finite element analysis, structural topology optimization, and composites optimization. Additionally, the fore-mentioned topics were reviewed in this chapter for the purpose of aiding in decisions made during the development of the research methodology applied during this dissertation *(presented in Chapter 3: Research method)*. Key factors which contribute towards lightweight wheel design are also discussed. This chapter is concluded with a brief summary of the critical contributions of the reviewed literature to this study.

2.2 Wheel design

The invention of the wheel, credited to the Mesopotamians in 3500 to 3200 B.C., is considered so important, that many scholars regard it as the dawn of modern civilization [14,15]. Additionally, the centuries following the invention of the wheel gave birth to numerous design improvements, transforming the wheel from a plain wooden disc used to transport chariots, to the modern wheels utilized in automotive transportation nearly five and a half centuries later [14].

During this period, the discovery of new materials, and the ever-increasing understanding of material behaviour has allowed for the design of wheels to combine enhanced strength and durability characteristics with lower mass [14]. One of the first major innovations in wheel design was the addition of an iron band to the circumference of wooden wheels so that greater loads could be transported by carts and wagons over increased distances [14].

Each innovation of the wheel produced a greater degree of component complexity and expanded knowledge. Consequently, the increased complexity

of the wheel resulted in various wheel components and characteristics becoming the subject of research serving to enhance the already vast body knowledge surrounding the behaviour and design of wheels. Two such examples include the development of characteristic tyre models by Pacajka, and the computational analysis of aluminium alloy wheels for the purpose of mass reduction by Jape et al. [13,14].

However, although the body of knowledge surrounding wheel behaviour and design is vast, this dissertation focused specifically on the strain behaviour exhibited by a purpose built, light-weight, eco-car wheel designed through sequentially applied structural topology and composites optimization techniques. Therefore, the literature of relevance to this dissertation focused on the methods pertaining to the design, analysis, and mass reduction of the modern wheel alone.

2.2.1 Overview of wheel design trends

As stated in the literary review provided by Keller in 2013, as taken from Burgoyne et al. in 1993, the design of the wheel focused on the use of wooden discs and spokes until the mid-19th century [16]. However, although this design prevailed through the years prior to 1871, it was rivalled by the introduction of the first wire-spoked wheel (commonly cited as the invention of the bicycle wheel) by Starley [16].

Starley's design was improved upon through the invention of the pneumatic tyre in 1888 [16]. This lead to a further improvement of wheel design through an adaption put forward by Welch in 1890 [16]. Welch's adaption allowed pneumatic tyres to seat more efficiently against the wheel rims to which they were attached [16].

The spoked wheel connected to a pneumatic tyre is still utilized in modern transportation to this day. Additionally, it has been the subject of research going as far back as the 1930's during which Pippard et al. theorized about the behaviour of spoked wheels induced by applied loads [16].

This work was later verified by Salamon et al., Burgoyne et al., and Gavin [16]. And, in doing so, the work performed by Gavin in 1996 highlighted the benefits of wheel rim design as a flexural beam put forward by Hetenyi [16].

Although these design approaches were validated against experimentally obtained data, the trend in modern wheel design relies heavily on the use of finite element analysis (*FEA*) to enable engineers to better understand the response of wheels to externally applied loads. An example of such a utilization of *FEA* to improve wheel design through material selection was demonstrated through the comparison of normal stresses and fatigue responses of wheels constructed from aluminium, magnesium, carbon fibre, and thermoplastic resin by Paropate et al. in 2013 [17].

Paropate et al. achieved this comparison through the use of *FEA* in which wheel loading was modelled as a static scenario accurately representing physical wheel behaviour [17]. In fact, static loading scenarios have been utilized extensively in the computational *FEA* of wheels and are, therefore, discussed later in section *2.3 Finite element analysis*.

However, the behaviour of commercial wheels as predicted using *FEA* is subject to user-induced uncertainty, and is, as such, not a sufficient means of confidently ensuring passenger safety. Therefore, commercially available wheels are required to undergo stringent physical testing to ensure that they do not fail during operation. It was stated by both Kumar et al. and Maserumele that wheels intended for commercial use are required to undergo testing according to a standard such as ISO 7141 to ensure that the they do not fail as a result of impact, radial fatigue, or rotary fatigue [18,19]. As such, the anticipated loads applicable to this study are discussed in the following section.

2.2.2 Wheel loading

The modern wheel is a load bearing component which serves as a means of connection between a pneumatic tyre and vehicle. As such, load transfer between the vehicle and ground is experienced by the wheel [2,19]. Furthermore, the nature and magnitude of each of these loads are dependent

upon the velocity, mass distribution, and trajectory of the vehicle, as well as tyre pressure and the quality of the surface upon which it is travelling [20]. Proper wheel design requires a detailed understanding of the vehicles anticipated operating conditions and mass distribution. For this dissertation, it is important to note that these operating conditions corresponded to those of a typical *SEM* race requiring the vehicle to maintain an average velocity of 25 km.h^{-1} (6.944 m.s^{-1}) while being capable of turning through a radius of 8 m [21]. Consequently, such conditions induce wheel loads of a radial, lateral, and torsional nature which were considered alongside the loading produced by tyre pressure [22]. The following subsections serve to define the fore-mentioned loading mechanisms; however, the manner in which these loads have been addressed in literature is discussed later in this chapter.

2.2.2.1 Wheel loading induced by means of tyre pressure

The inflation of pneumatic tyres as utilized on modern automotive wheels produces an enclosed volume of pressurized air which induces stress in the wheel rim to which it is seated [23]. The state of this induced stress is usually small in magnitude, and static in nature when compared to the stresses resulting from vehicle motion [23]. However, the wheel rim stress induced by tyre pressure are still important in the design and analysis of wheels as the resultant loading combination is determined through the summation of all applied loadings. Additionally, this enclosed volume of pressurized air acts normal to the surface with which it is in contact as shown in *Figure 4*.
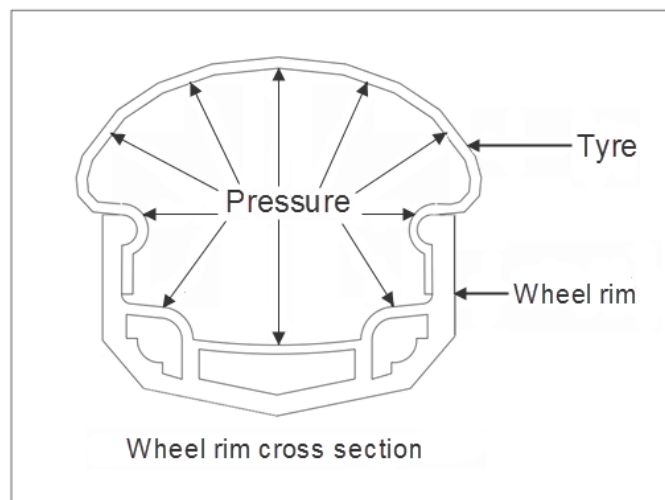
Figure 4 - Tyre inflation pressure distribution

Figure 4 illustrates that the volume of air pressurized during the inflation of a pneumatic tyre contacts both the wheel rim and tyre itself. The pressurized air which contacts the wheel rim exerts force directly on to the wheel rim. Since this force is applied directly to the wheel rim, its magnitude is usually not influenced by external factors.

However, the tyre is forced against the flange of the wheel rim by the pressurized air with which it is in contact. This results in the enclosed volume of pressurized air exerting an indirect force on the wheel rim flanges. The magnitude of this force may be influenced by the tyres material, cross sectional aspect ratio, and reinforcement material [23]. Brandt stated that the forces induced in the wheel rim as a result of tyre pressure are so dependent on the construction of the tyre that they may be completely cancelled out in some cases [2].

2.2.2.2 Wheel loading induced by means of applied radial force

The wheels function in supporting the mass of the vehicle to which it is attached results in a radial reaction force being transferred from the ground to the wheel through the pneumatic tyre [22]. The magnitude of this radial load, as experienced by each wheel during operation, may be determined using classical mechanics as the radial vector component of the product of the mass supported by each wheel at the tyre-ground contact patch and gravitational acceleration. This is shown in *Equation 2.2.1*.

$$F_N = \cos(\theta) \cdot m_w \cdot g \qquad (2.2.1)$$

Where: F_N = Normal force experienced by the wheel [N]

θ = Wheel camber angle [°]

m_w = Mass supported by the wheel [kg]

g = gravitational constant of acceleration = 9.810 m.s^{-2}

However, the vehicle mass supported by each wheel changes during cornering as a result of the induced centrifugal force produced by vehicle motion through

an arc. This centrifugal force is equal in magnitude and opposite in direction to the sum of the centripetal forces maintaining the vehicles intended direction at each tyre-ground contact patch. As such, the magnitude of this centrifugal force is equal to the product of supported mass and centripetal acceleration as shown in *Equation 2.2.2*.

$$F_{cgl} = m_v \cdot a_p \qquad (2.2.2)$$

Where: F_{cgl} = Centrifugal force experienced by the vehicle [N]

m_v = Mass of the vehicle [kg]

a_p = Centripetal acceleration [$m.s^{-2}$]

Additionally, the magnitude of this centripetal acceleration may be determined as the quotient of the squared linear vehicle velocity and the radius of the arc through which it is travelling as defined in *Equation 2.2.3*.

$$a_p = \frac{v^2}{r} \qquad (2.2.3)$$

Where: v = Linear velocity of the vehicle [$m.s^{-1}$]

r = Radius of arc [m]

However, the maximum centripetal force permissible during vehicle motion through an arc must be such that it does not allow for slipping between the tyres and road. Therefore, the magnitude of this centripetal force may be determined as the product of the total vehicle weight and the static coefficient of friction between the tyres and road as shown in *Equation 2.2.4*.

$$F_{cpl} = F_{cgl} = m_v \cdot a_p = \mu \cdot m_v \cdot g \qquad (2.2.4)$$

Where: F_{cpl} = Centripetal force experienced by the vehicle [N]

F_{cgl} = Centrifugal force experienced by the vehicle [N]

m_v = Mass of the vehicle [kg]

a_p = Centripetal acceleration [m.s^{-2}]

μ = Coefficient of friction between the tyres and road = 0.8 [22]

g = gravitational constant of acceleration = 9.810 m.s^{-2}

The maximum permissible centrifugal force determined through solving *Equation 2.2.4* allows for the radial reaction force experienced by each wheel to be determined through the summing of moments.

2.2.2.3 Wheel loading induced by means of applied lateral force

A lateral load is experienced by each wheel during operation as a result of vehicle motion through an arc. This force acts in the opposite direction to lateral vehicle motion; that is to say that if a vehicle is moving through a clockwise arc (cornering right), the lateral force will act at the tyre-ground contact patch in the direction towards the vehicles left hand side. This lateral load is of equal magnitude and opposite direction to the centripetal force defined in *Equation 2.2.4*.

When considering the effects of lateral loading applied to cambered wheels, this force must be resolved into its lateral and radial components relative to the lateral axis of each wheel at the tyre contact patch. These components are shown in *Figure 5*.
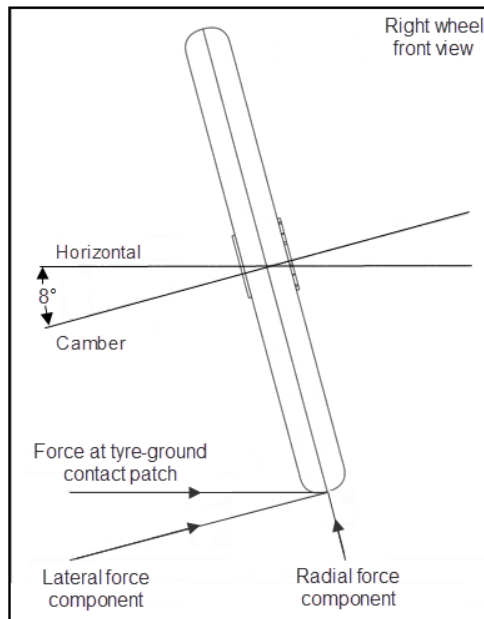
Figure 5 - Forces at tyre contact patch as a result of cornering

2.2.2.4 Wheel loading induced by means of applied torsion

A torsional load acts tangentially to each wheel at the tyre-ground contact patch as a result of the vehicles forward motion rotating each wheel. These torsional loads are a maximum at the moment that each wheel starts to rotate from a stationary position.

The rear wheel of the *Nelson Mandela University Eco Car* is the driving wheel. The rotational power output of the vehicles engine is transferred to the rear axle of the vehicle by means of a chain and sprockets. One-directional bearings connect the rear wheel and axle of the *Nelson Mandela University Eco Car*. Forward rotation of the vehicles rear axle causes its rear wheel to drive the vehicle. Therefore, the maximum torque experienced by the rear wheel may be determined by *Equation 2.2.5*.

$$T_{RW} = T_{EO} \cdot N \tag{2.2.5}$$

Where: T_{RW} = Maximum torque experienced by rear wheel [Nm]

T_{EO} = Maximum torque produced by engine [Nm]

N = Sprocket Ratio

The torque experienced by each of the front wheels is equal to the product of the wheel radius and the force required to overcome rolling resistance as shown in *Equation 2.2.6*.

$$T_{fw} = \frac{\emptyset_w \cdot F_{rr}}{2}$$ (2.2.6)

Where: T_{fw} = Maximum torque experienced by a front wheel [Nm]

F_{rr} = Force required to overcome rolling resistance [N]

$\emptyset_w$ = Wheel diameter = 0.498 m [22]

The force required to overcome rolling resistance may be taken as the product of the vehicle weight supported by each wheel and the coefficient of rolling resistance between the tyre and road as defined in *Equation 2.2.7*.

$$F_{rr} = f_r \cdot F_r$$ (2.2.7)

Where: F_{rr} = Force required to overcome rolling resistance [N]

f_r = Coefficient of rolling resistance = 0.0024 [22]

F_r = Vehicle weight supported by wheel [N]

The vehicle weight supported by each front wheel is equal to the product of the mass supported by each front wheel and gravitational acceleration.

2.3 Finite element analysis

Finite Element Analysis (FEA) is a commonly used design tool which utilizes the *Finite Element Method (FEM)* to produce approximate solutions to partial differential equations which describe the behaviour of a system [5]. These solutions allow engineers to predict the response of a system to some forcing function, so that design quality may be improved upon, while simultaneously reducing design time and cost [5]. Consequently, different response types are required to aid engineers in improving different design characteristics dependent on the nature and function of a system.

Commercially available *FEA* software packages allow engineers to perform various types of analyses, including [5]:

I.   Linear static

II.   Nonlinear

III.   Dynamic

IV.   Buckling

V.   Modal

VI.   Thermal

VII.   Fatigue

VIII.   Computational Fluid Dynamics

IX.   Crash

Vast bodies of literature addressing each of the fore-mentioned analysis types may be found in engineering journals and textbooks. However, of particular relevance to this dissertation was the work performed by Doyle, Paropate et al., and Patel et al., in which linear static *FEA*s were used to aid in the design of wheels [17,24,25]. The *FEA*s forming the basis of structural optimizations applied to wheels as performed by Das et al., Hong et al., and Jape et al., were also of a linear static nature [14,26,27].

Linear static *FEA* assumes that the material properties of the model being analysed are of a linear-elastic nature, and that the loads and constraints applied to the model do not vary with time [28]. Such an analysis allows the user to predict the nature and magnitude of each of the following response types at various positions within the system [28]:

X.   Reaction forces

XI.   Displacement

XII.   Strain (both normal and shear)

XIII.   Stress (both normal and shear)

XIV.   Factor of safety

The following subsections serve to provide an overview of the general procedure to be followed when performing a linear static *FEA*, as well as the theory and drawbacks of such an analysis.

2.3.1 Linear static *FEA* procedure [28]

Regardless of the component being analysed, or the nature of the desired response produced by means of a linear static *FEA*, the general procedure to be followed remains the same. This procedure is shown in *Figure 6*.
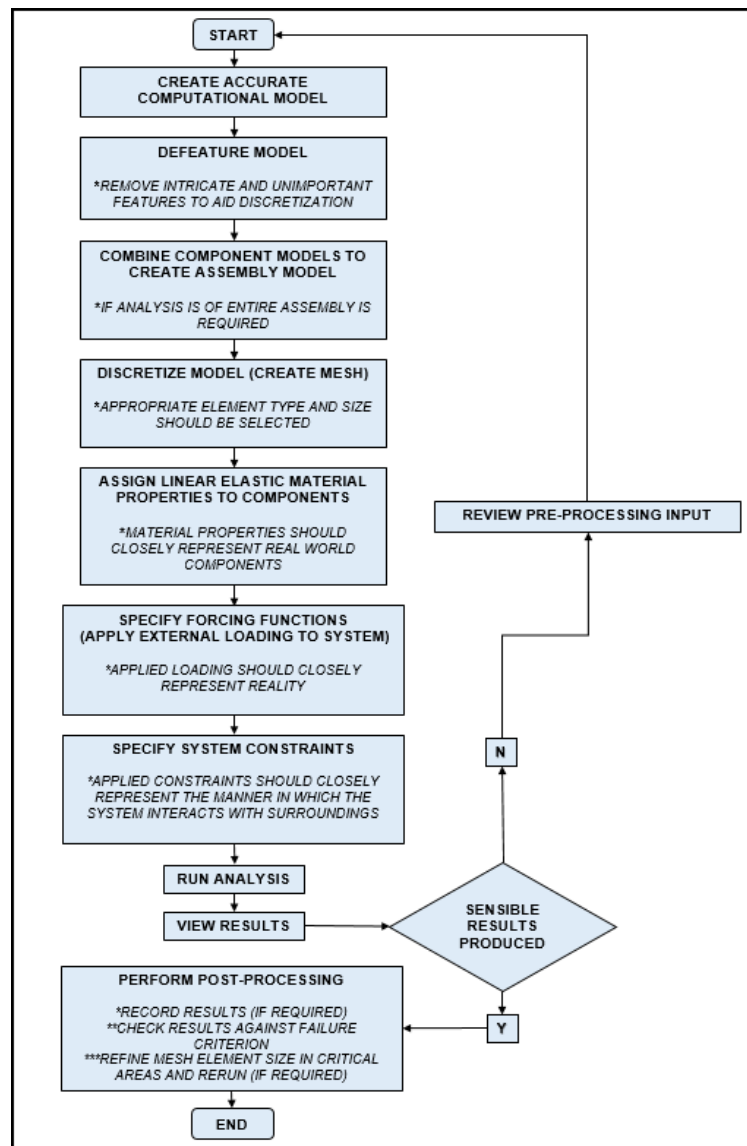
Figure 6 – Generalized linear static finite element analysis procedure as adapted from Akin [28]

Figure 6 shows that the first stage of performing a linear static *FEA* is to create an accurate software based model of the component being analysed. This stage is followed by simplifying the model through the removal of any geometric features which are unnecessary to the analysis. Doing this reduces the number of elements required to accurately represent the model. In addition, it reduces the time required to both discretize and analyse the model. If the linear static *FEA* is to be performed on a model comprising of multiple bodies which form an assembly, these parts should be appropriately combined after being de-featured. The model is then discretized into finite elements. Both the size and

type of elements specified during discretization are dependent on the model being analysed.

The following three stages required to perform a linear static *FEA* include assigning linear elastic material properties, forcing functions, and system constraints to the appropriate elements. The validity of the results obtained through linear static *FEA*s are greatly dependent on how closely these three stages represent reality.

The *FEA* is then solved, and the results reviewed. Interpreting the results accurately requires some comparative benchmark. This benchmark may be experimentally or analytically obtained data such as stress, strain, or deflection values. By comparing the *FEA* results to this benchmark, it may be investigated whether or not the *FEA* model accurately represents reality.

If the *FEA* results appear valid, they may be utilized as intended by the user. If they do not represent reality, the input corresponding to each stage of linear static *FEA* prior to solving should be re-evaluated. The analysis should then be re-solved, and the results re-checked. This process should be repeated until the linear static *FEA* results become acceptable to the user.

2.3.2 Finite element method [28]

The *FEM* is the numerical foundation upon which all *FEA*s are based. This subsection provides a brief overview of the manner in which governing differential equations are converted into matrix equations and solved using *FEM*.

However, before such solutions may be determined, the system being analysed needs to be discretized into a union of simplified geometries. This is commonly known as the process of "*meshing*"; and, in the case of a linear static stress analysis, the system to be discretized is a spatial distribution of linear elastic material subject to externally applied constraints and forcing functions. For the purpose of illustrating this process, consider the arbitrary material distribution presented in *Figure 7* (a).
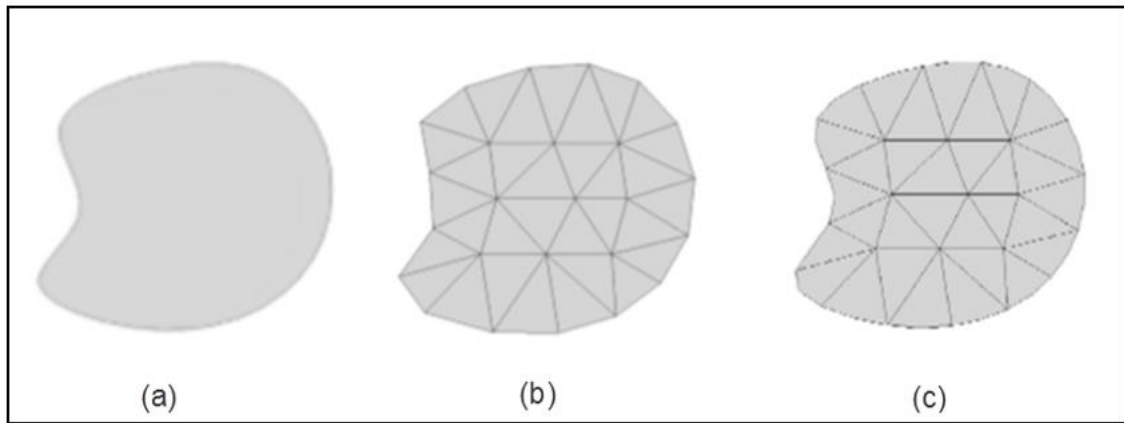
Figure 7 - Arbitrary material distribution simplified through discretization as adapted from Akin [28]

Determining a property such as the surface area of this geometry would require integration of the equations describing the boundary curves. However, although this is theoretically possible, it is computationally expensive and subject to the knowledge of the bounding curve equations. A simpler solution may be achieved through approximating the arbitrarily defined geometry with smaller simply defined geometries whose individual areas may be summed. Such approximations are shown in *Figure 7* (*b and c*).

The simplified geometries used to approximate the system being analysed are commonly referred to as *elements*, while the points of intersection at which these elements are connected are termed *nodes.*

In the same way that the area of an arbitrarily defined geometry may be approximately determined through discretization and the scalar summing of individual element areas, so too may other properties be determined. In essence, the finite element method achieves this regardless of the property being determined through the conversion of governing integral statements into matrix systems which are then solved. If the system is initially described using governing differential equations, equivalent integral statements are produced by some means of *Weighted Residual Method* (*WRM)*. The two most commonly used weighted residual methods include the *Galerkin Method*, and the *Method of Least Squares*, both of which are extensively covered in literature.

The fore-mentioned governing integral statements are formulated by most commercially available *FEA* software packages on the *Principle of Minimum Potential Energy* in order to determine the equilibrium state of the system. This principle defines the potential energy of the system as the difference between the strain energy of the system and the mechanical work done by the externally applied forces. By definition, mechanical work is the scalar product of the vectors describing the applied forces and resultant displacements, while strain energy is equal to one half of the product of the system stiffness and squared displacement vectors.

Consequently, the primary unknown to be solved for by means of interpolation between nodes is the displacement vector of the system. Once the displacement of each node in the system has been determined, it may be used to determine the strain of each node with reference to the original node position. Similarly, once the strain of each node has been determined, the nature and magnitude of stress at each node may be solved by means of applying *Hooke's Law*.

Intricate mathematical explanations of this process are readily available in literature and textbooks. As such, they are not presented in this text. It is also important to mention that in most instances, the program code used by commercially available *FEA* software packages is proprietary information often never seen by users. Rather, this section focuses on the use of *FEA* software packages from the perspective of the user. As such, commonly obtained errors associated with linear static *FEA*s are discussed in the following subsection.

2.3.3 Error associated with linear static *FEA*

The degree of accuracy associated with any linear static *FEA* results is subject to the quality of analysis pre-processing [28]. Typically, the accuracy of computational *FEA* strain values should be within 10 percent of those measured physically as stated by the *Federal Aviation Administration* (*FAA*) [29]. This quality is reduced through the inclusion of assumption and uncertainty by the user during various stages of analysis set-up [28]. *Figure 8* shows a graphical

comparison of the degrees of error most commonly introduced by the user during each stage of computational analysis.
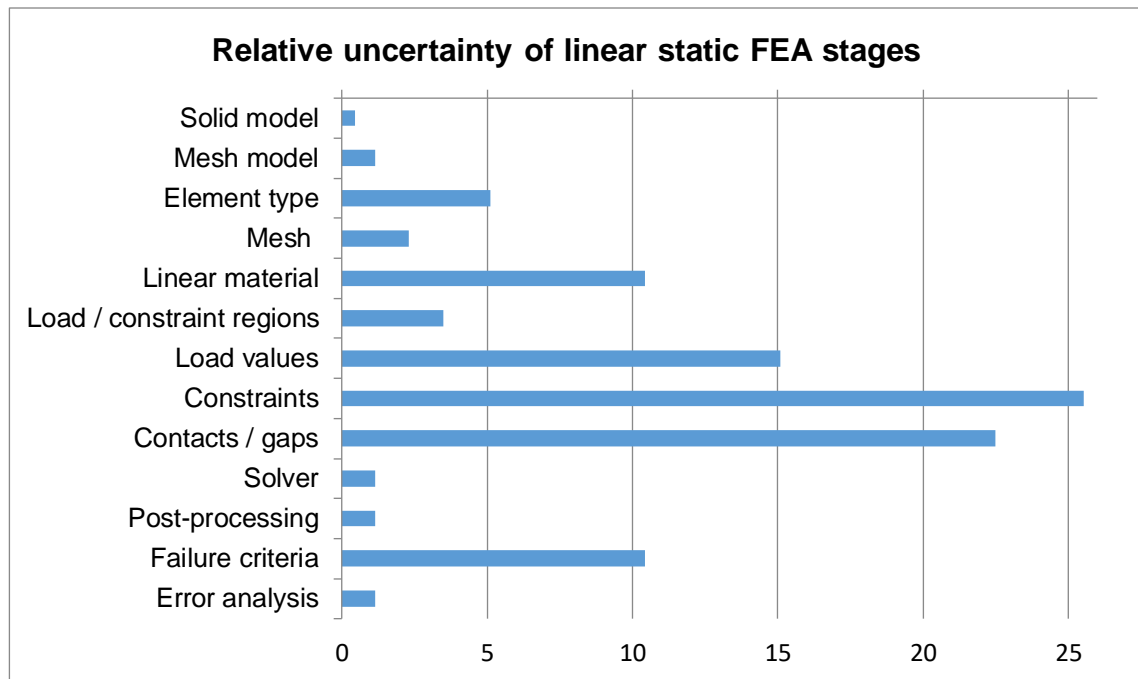
Figure 8 - Commonly introduced error during various stages of analysis as adapted from Akin [28]

It may be seen from *Figure 8* that the highest degrees of error are introduced during the meshing, material designation, loading, and constraining phases of pre-processing. These fore-mentioned errors, and the manner in which they may be reduced, are discussed in the following paragraphs.

Firstly, any curved geometry is subject to unavoidable geometric error introduced as a result of approximate domain representation by means of simplified elements during discretization. While impossible to eliminate completely, this type of error may be reduced through the selection of appropriate element type and size [28].

Elements may exist as one, two, or three-dimensional entities, each of which is well suited to specific *FEA* scenarios. One-dimensional elements are appropriate for representing lengthy entities of continuous cross section such as a beam or truss member. Two-dimensional elements, commonly referred to as *shell* elements, are well suited to representing entities where two dimensions are marginally larger than the third. Such examples include composite

laminates or sheet metal components. Lastly, three dimensional elements are required to represent entities of which all dimensional properties are significant, influential, or subject to continuous variation.

In the case of both two-dimensional and three-dimensional elements, the order of each element is commonly specified as either first or second. The use of second order elements greatly reduces the degree of geometric approximation error associated with curved entities; however, the computing resources required to produce a solution for such a system increases drastically [28]. *Figure 9* illustrates the difference in accuracy of geometric approximation by means of first-order linear elements (*a*) against second-order parabolic elements (*b*).
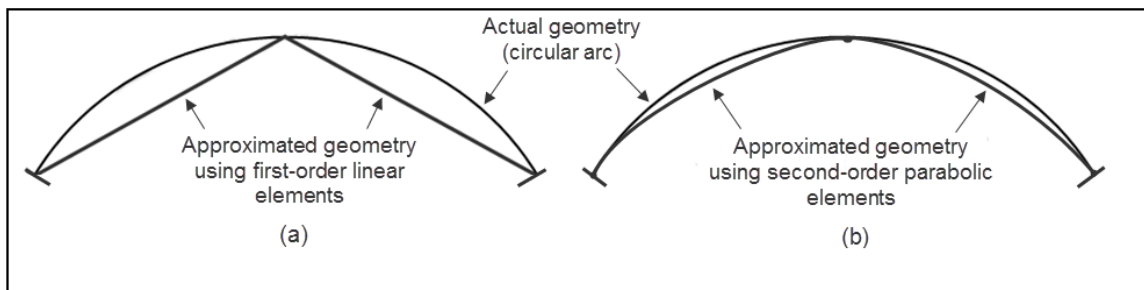
Figure 9 - Comparison of curvature by means of linear and parabolic elements as adapted from Akin [28]

The element type and specified order are equally important to the shape of the element specified by the user. The most widely specified two-dimensional and three-dimensional element shapes are shown in *Figure 10* and *Figure 11* .
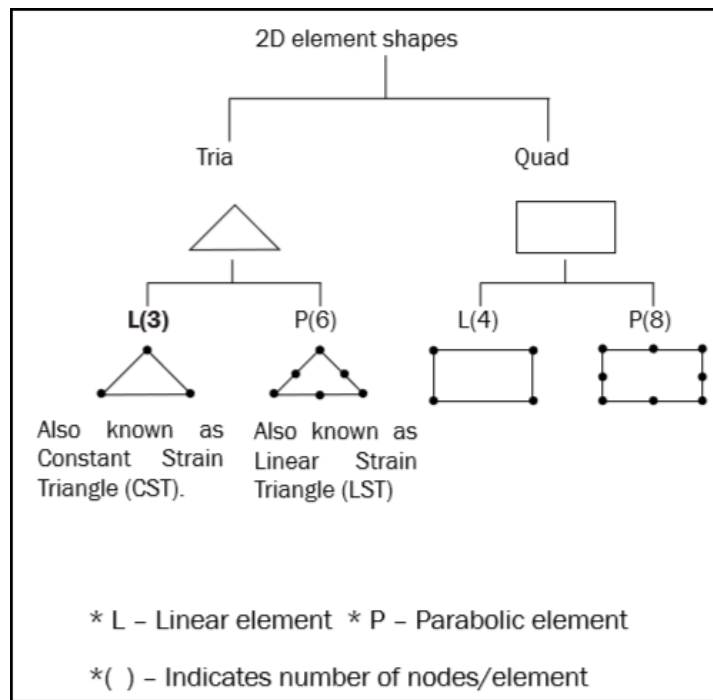
Figure 10 - Two-dimensional element shapes [5]
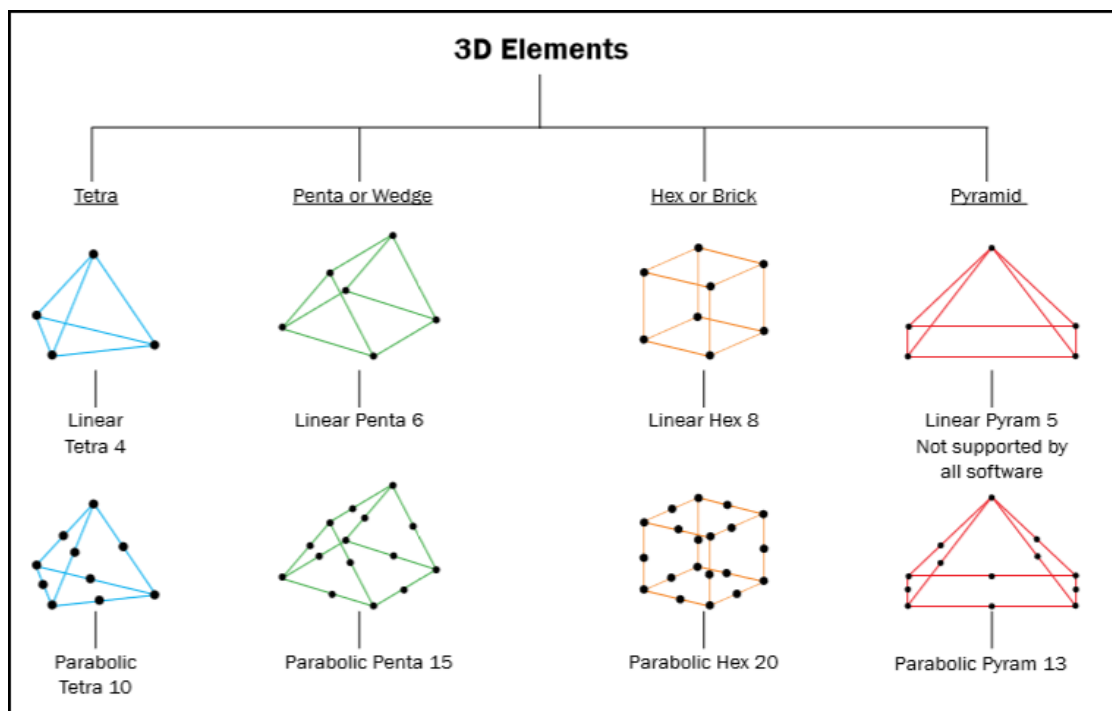
Figure 11 - Three-dimensional element shapes [5]

Although elements may exist in numerous forms, the type of element specified during analysis is particular to the degree of desired accuracy, the nature of the problem at hand, the computational resources available to produce a solution, and the types of available elements within a given software package [28].

In addition, the degree of element quality associated with discretization will not enhance the accuracy of produced results if the material properties assigned to the system being analysed are incorrect. Most modern software packages have built in material libraries which allow the user to apply generalized material properties to a computational model [28]. The term *generalized* is used in the previous statement as there is often no information pertaining to the origin of these properties, or the variation of test results upon which they are based [28]. *Figure 12* shows the distribution of typically measured material properties for steel (*a)* and cast iron (*b*), the average of which constitutes as the material properties found in a typical software based material library [28].
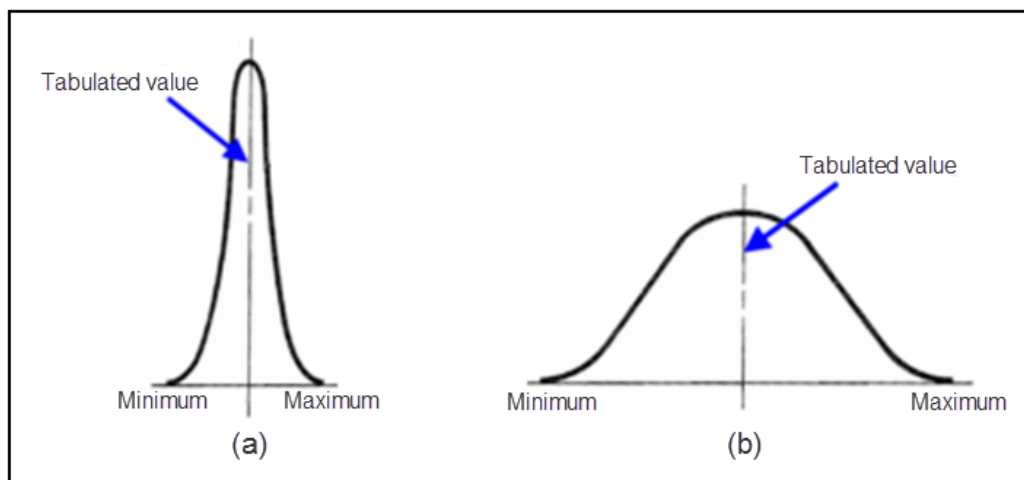
Figure 12 - Typical distributions of properties of steel (a) and cast iron (b) as adapted from Akin [28]

It should be mentioned that assigned material properties are merely averaged probability distributions with an inherent degree of associated uncertainty which may be reduced, but not eliminated, by the use of accurately measured experimental data rather than tabulated properties [28].

The final stage of analysis pre-processing during which the highest degree of error is introduced by the user is the definition of applied loads and constraints. This stage of analysis set-up is extremely sensitive to the specific problem being analysed [28]. As such, the manner in which these external loads (represented by means of Neumann boundary conditions) and constraints (represented by means of Dirichlet boundary conditions) are applied specifically to wheels is discussed in the following subsection.

2.3.4 Loads and constraints as applied to wheels during linear static *FEA*

Loads experienced by a wheel during operation exist as a result of tyre inflation pressure and vehicle motion. These loads are transferred between the ground and wheel through the tyre. Both the magnitude and manner in which these loads are transferred to the wheel may be influenced by the tyres construction and material properties. Contact between the wheel rim and tyre is non-linear, and mathematically complex to characterize [23]. In fact, this complex non-linear characterization is usually disregarded in the *FEA* of wheels.

The manner in which loads and constraints have been applied to computational wheel models in literature was relevant to the computational analyses, topology optimizations, and composites optimizations presented in this dissertation. Therefore, they are now discussed in this section.

The effects of loading by means of tyre pressure was accurately represented by Borase et al. through applying an evenly distributed load acting normal to the wheel rim surfaces affected by pressure [23]. This method was also utilized to represent tyre pressure in the *FEA* of wheels as performed by Patel et al., Radha et al., and Prasad et al. [15,25,30]. Adversely, wheel loading by means of tyre pressure was omitted entirely in numerous literary analyses including those presented by Jape et al., and Das et al. [14,26].

While loading induced by means of tyre inflation pressure is sometimes neglected in literature, wheel loads induced as a result of vehicle motion are critical, and almost always accounted for. These radial, lateral, and torsional loads are represented through various different methods in the computational design and analysis of wheels. One of the earliest methods used to represent an applied radial load to a wheel was the application of a single point load to a two-dimensional computational wheel model as performed by Brandt in 1981 [2]. While the *FEA* results determined by Brandt compared closely to experimentally measured values of spoke deflection, the manner in which radial loads have been applied to computational wheel models has differed among researchers and analysts.

Mariappan et al. in 2003 represented radial loading as a single point load applied directly to a 150 mm length of the wheel rim [31]. Keller utilized single point loads acting over one degree of the wheel rim to represent radial and torsional loading [16]. In 2014, Das represented radial loading as a point load connected to various sections of the wheel rim by means of *RBE3* (rigid) elements [26]. Further use of a single point load to represent applied radial loading to wheels was also seen in the work performed by Sabri et al. in 2015, which focused on the deformation of automotive wheels subject to different radial loads [20].

However, the point load is not the only manner in which radial, lateral, and torsional loads have been applied in literature. Xiao et al. used an evenly distributed load acting across an unspecified length of wheel rim [32]. It was not specified how these loads were applied to the wheel *FEA* in the research performed by Paropate et al. in 2013 [17]. It is possible that Paropate et al. did not utilize a point load to apply each of these loads to the *FEA* wheel model. Additionally, it was not specified how these loads were applied to the wheel models in the *FEA* work performed by Radha et al. [30].

It is apparent from the above summary that the most commonly utilized method to represent radial, lateral, or torsional loading applied to a computational wheel model has been by means of a point load connected to a small section of the wheel rim. The prevalent manner used to apply displacement constraints to computational wheel models in literature appears as the restriction of all translational and rotational degrees of freedom of the nodes in the wheel hub or surrounding bolt holes. An example of such applied constraints was seen in the 2006 work put forward by Kalyanasundaram et al. in which the composite centre of a wheel-chair wheel was computationally analysed and improved upon [33]. In 2014, Patel et al., and Hong et al. also utilized this method to constrain *FEA* wheel models [25,27]. A slightly varied form of this method was evident in the work performed by Das, who rigidly constrained the nodes in the hub of a computational wheel model to a one-dimensional element representative of the wheel axle [26].

2.4 Structural topology optimization

Topology refers to the mathematical study of the spatial distribution and geometric positions within a confined volume or area [34]. The study of topology deals primarily with properties which are preserved during the deformation of three-dimensional geometric entities [34]. These principles form the basis of structural topology optimization and allow engineers to minimise the work done by external loading on a confined volume through the efficient distribution of material [34].

Consequently, structural engineers and designers are able to produce components which are efficiently designed at a concept phase if the intended loadings and constraints of the component are known [34]. The efficiency of this material distribution, as determined using structural topology optimization, is always unique to a component and dependent on the objective optimization function and boundary conditions describing the applied loading and constraints [32]. An example of such a material distribution is shown in *Figure 13* [35]. The structural topology optimization of a roll bar by the *Force India Formula One Team* resulted in an 86 percent mass reduction [35].
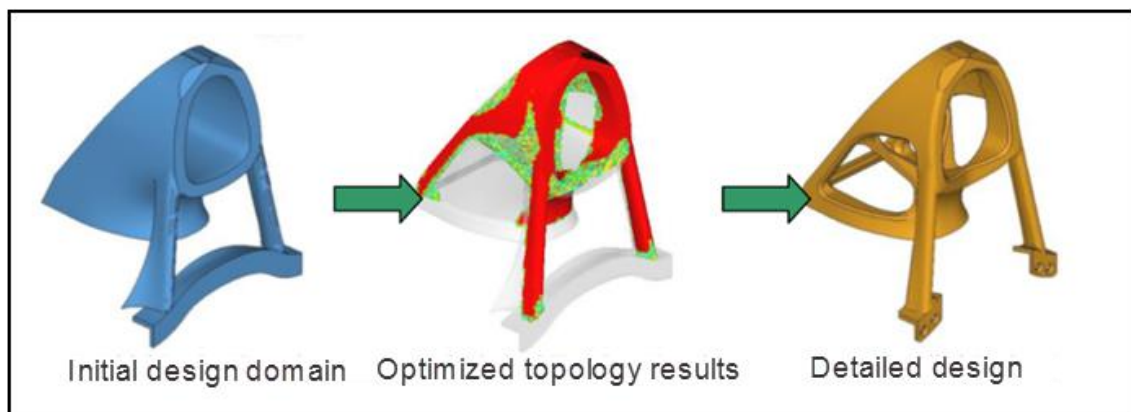
Figure 13 - Topology optimization of a roll-bar producing 86 percent mass reduction performed by *Force India Formula One Team* as adapted from Zhou et al. [35]

It is quite common for material distributions produced by means of structural topology optimisation to favour additive manufacturing processes as a result of their inherently organic nature [36]. Extensive research has been conducted in recent years to address the various problems surrounding the feasibility of using

traditional manufacturing processes to actualize the material distributions produced using structural topology optimization software.

Manufacturability and uncertainty relating to damage and nonlinear component behaviour were cited as the main drawbacks associated with the feasibility of topology optimization in a 2012 review performed by Guest et al. [37]. However, modern topology optimization software packages address these concerns by allowing structural engineers and designers to state additional boundary conditions in order to produce component geometries which are both efficient, and topologically suited to a given manufacturing process [37]. One such example includes the '*split-draw*' shape control found in the commercially available *Altair HyperWorks* suite. This constraint ensures that the geometric solution produced by means of structural topology optimization is suited to manufacturing by means of casting processes. Furthermore, this constraint may be applied as either a '*No Hole*', or *'Hole Allowed'* variant to enhance the suitability of the posed solution. Simply put, the application of a '*No Hole*' split draw constraint produces geometries which contain no through-hole features [38]. Adversely, application of the *'Hole Allowed'* split draw constraint produces geometries which may contain through-hole features [38].

Structural topology optimization has great potential to produce efficient component designs which benefit global industry and trade by allowing manufacturers to reduce the mass and material content of both new and conventionally designed components. The implications of this include [17]:

I.   improved fuel efficiency in automotive, aeronautical, and maritime transportation
II. reduced material costs during component manufacture
III. reduced transportation costs between manufacturer, distributor, and consumer
IV. improved product design

The following subsections serve to provide an understanding of the underlying numerical methods, and cases of successful application of structural topology optimization techniques relevant to this dissertation.

2.4.1 Solid isotropic material with penalization (*SIMP*) [11]

The numerical method utilized most extensively in the field of structural topology optimization to efficiently distribute material is the *SIMP* method [11,38]. When using this method, the objective optimization function to be minimized during optimization may describe either domain mass or stiffness.

An overview of the manner in which this method may be utilized to minimize domain compliance, as adapted from Bendsøe et al., is presented in this subsection [11]. This overview is presented using contracted engineering notation to explain the compliance minimization of a simplified two-dimensional continuum for the purpose of clear conceptual explanation.

Any mechanical component is a body which occupies some two or three dimensional space ($\mathbb{R}^2$ or $\mathbb{R}^3$). The volume of space occupied by such a body is viewed as a domain denoted using Ω. Therefore, the domain Ω is representative of the design space to be optimized, and may be occupied by a combination of sub-domains representing either the presence (Ω^{mat}), or absence (Ω^{void}) of a solid isotropic material. A representation of these fore-mentioned domains as subjected to external loading and displacement constraints is shown in *Figure 14*.
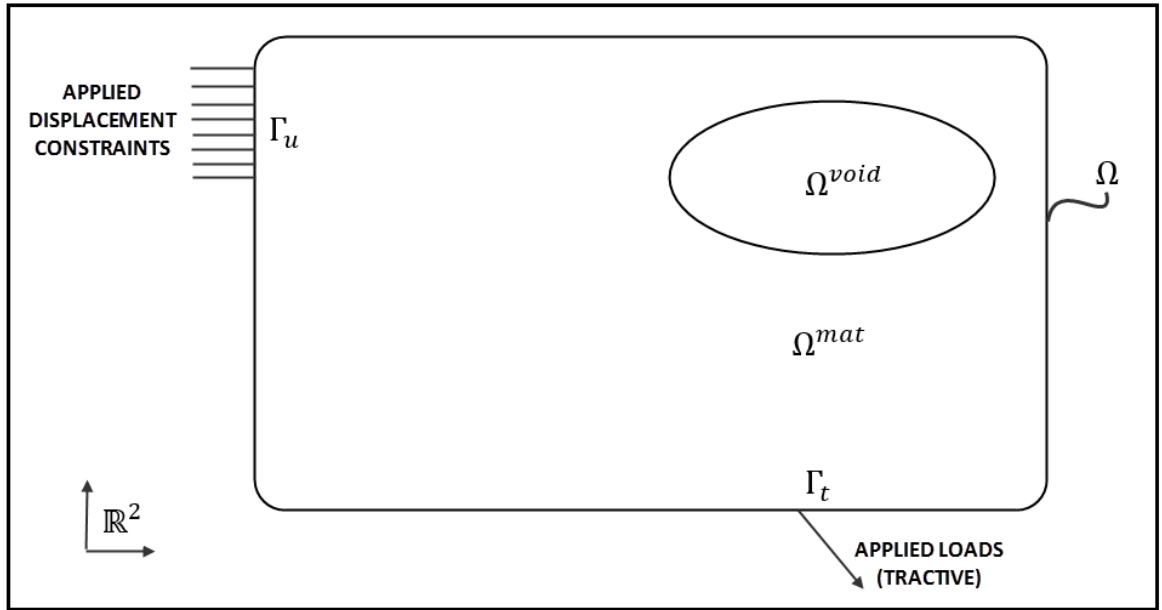
Figure 14 – Design space topology with applied tractive loads and displacement constraints as adapted from Bendsøe et al. [11]

Minimizing the compliance of such a continuum requires that the energy bilinear form of an elastic body in a state of equilibrium (u), for some virtual displacement (v), be considered as shown in *Equation 2.4.1*.

$$a(u,v) = \int_\Omega E_{xy}(x) \cdot \varepsilon_x(u) \cdot \varepsilon_y(v) d\Omega$$

(2.4.1)

Where:

$a(u,v)$ represents the energy bilinear form of an elastic body

$E_{xy}(x)$ represents the domain stiffness tensor

$\varepsilon_x(u)$ and $\varepsilon_y(v)$ represent the linearized strains of the energy bilinear form

This energy bilinear form considers the applied tractive loads and resultant internal body forces by means of the load linear form defined in *Equation 2.4.2*.

$$l(u) = \int_\Omega f \cdot u \, d\Omega + \int_{\Gamma_T} t \cdot u \, ds$$

(2.4.2)

Where:

$l(u)$ represents the load linear form

f represents the internal body forces produced in Ω

t represents the surface tractive forces applied to the boundary Γ_T

Optimization of the design function now describes the problem of determining the optimum allowable domain stiffness tensor (E_{ad}), and may be rewritten in the following form.

$$\min_{u \in U, E} l(u)$$
$$s.t.: a_E(u,v) = l(v), \quad for\ all\ v \in U$$
$$E \in E_{ad}$$

(2.4.3)

Where:

$l(u)$ represents the load linear form

$a_E(u,v)$ represents the energy bilinear form of an elastic body

U represents all allowable kinematic displacement fields

E_{ad} represents all allowable stiffness tensors

Solving *Equation 2.4.3* requires discretization of the domain Ω into finite elements which account for both displacement (u) and stiffness (E). Regarding E as a constant during discretization allows the optimization function to be rewritten as follows.

$$\min_{u, E_e} f^T \cdot u$$
$$s.t.: K(E_e) \cdot u = f$$
$$E_e \in E_{ad}$$

(2.4.4)

Where:

f represents the domain load vector

u represents the domain displacement vector

K represents the domain stiffness matrix

E_e represents element stiffness

E_{ad} represents all allowable stiffness tensors

The domain stiffness matrix, K, is defined in *Equation 2.4.5* as the sum of each individual element stiffness present in Ω. The quantity of elements which exist in Ω is denoted using e, and is dependent on the previously discussed discretization of Ω.

$$K = \sum_{e=1}^{N} K_e(E_e)$$

(2.4.5)

Where:

K represents the domain stiffness matrix

K_e represents the global element stiffness matrix

E_e represents element stiffness

The applied discretization allows the optimization function to be solved by finding the optimum distribution of material (Ω^{mat}) and voids (Ω^{void}) within Ω. Therefore, an element, e, is defined by the assignment of stiffness properties representative of either material (Ω^{mat}) or void (Ω^{void}) matter to produce a binary element density function as shown in *Equation 2.4.6*.

$$E_{xy} = \mathbf{1}_{\Omega^{mat}} \cdot E^0{}_{xy,}\ \mathbf{1}_{\Omega^{mat}} = \begin{cases} 1\ if\ x \in \Omega^{mat} \\ 0\ if\ x \in \Omega \backslash \Omega^{mat} \end{cases}$$

$$\int_{\Omega} \mathbf{1}_{\Omega^{mat}} d\Omega = Vol(\Omega^{mat}) \leq V$$

<div align="right">(2.4.6)</div>

Where:

E_{xy} represents the stiffness tensor assigned to an element

$\mathbf{1}_{\Omega^{mat}}$ represents the presence or absence of material at an element

$E^0{}_{xy}$ represents the stiffness tensor of an assigned isotropic material

V represents the maximum volume of permissible material within Ω

The assignment of either material (Ω^{mat}) or void (Ω^{void}) stiffness to the elements within Ω may be solved by replacing the associated discrete variables with continuous variables. However, doing so may introduce intermediate stiffness tensors which correspond to neither the desired material nor void matter. As such, a penalization is introduced to ensure that only stiffness tensors representing the complete presence or absence of the assigned isotropic material are produced when solving *Equation 2.4.6*. The fore-mentioned penalization is applied as follows.

$$E_{xy}(x) = \rho(x)^p \cdot E^0{}_{xy,}\ p > 1$$

$$\int_{\Omega} \rho(x)d\Omega \leq V;\ 0 \leq \rho(x) \leq 1, x \in \Omega$$

<div align="right">(2.4.7)</div>

<div align="center">such that</div>

$$E_{xy}(\rho = 0) = \rho_{min}$$
$$E_{xy}(\rho = 1) = E^0{}_{xy}$$

Where:

E_{xy} represents the stiffness tensor assigned to an element

$\rho(x)$ represents the material presence density

p represents the penalization factor

$E^0{}_{xy}$ represents the stiffness tensor of an assigned isotropic material

V represents the maximum volume of permissible material within Ω

ρ_{min} represents the minimum admissible density

The minimum admissible density is generally regarded as 10^{-3} kg.m^{-3} so as to approximate zero. Although it should theoretically be zero in order to truly represent the absence of material, doing so would produce an equilibrium associated singularity. The presence of such a singularity would render the problem unsolvable.

The introduction of the above penalization scheme now allows the posed topology problem to be viewed as a sizing problem in which the magnitude (*one or zero*) of each element density describing the presence or absence of material may be solved. It is important to mention that the required magnitude of the applied penalization factor is dependent on the type of space in which the domain Ω exists, and, as such, may be determined according to *Equation 2.4.8*.

$$p \geq max\left\{\frac{2}{1 - v^0} , \frac{4}{1 + v^0}\right\} \ [in \ \mathbb{R}^2]$$
$$p \geq max\left\{15 \cdot \frac{1 - v^0}{7 - 5v^0} , \frac{3}{2} \cdot \frac{1 - v^0}{1 - 2v^0}\right\} \ [in \ \mathbb{R}^3]$$

(2.4.8)

Where:

p represents the penalization factor

v^0 represents the Poisson coefficient of the assigned isotropic material

The initially posed problem described by *Equation 2.4.3* may be rewritten to account for the penalized binary element density function as presented in *Equation 2.4.9*.

$$\min_{u \in U, \rho} l(u)$$
$$s.t. : a_E(u, v) = l(v), \quad for\ all\ v \in U$$
$$E_{xy}(x) = \rho(x)^p \cdot E^0_{xy,}$$
$$\int_{\Omega} \rho(x)d\Omega \leq V;\ \rho_{min} \leq \rho(x) \leq 1$$

(2.4.9)

Where:

$l(u)$ represents the load linear form

$a_E(u, v)$ represents the energy bilinear form of an elastic body

E_{xy} represents the stiffness function

$\rho(x)$ represents the material presence density

p represents the penalization factor

E^0_{xy} represents the stiffness tensor of an assigned isotropic material

V represents the maximum volume of permissible material within Ω

ρ_{min} represents the minimum admissible density

Minimization of the above optimization problem as defined by *Equation 2.4.9* may now be solved using a standard *Lagrangian* approach [11]. Since standard *Lagrangian* mathematics is extensively covered in published literature and textbooks, and utilized in numerous applications, it was not discussed in this dissertation. Application of the fore-mentioned optimization process is discussed in the following section.

2.4.2 Application of topology optimization to wheels

Numerous literary studies concerned with the structural topology optimization of mechanical components exist. However, only examples which were relevant to this dissertation are presented in this subsection.

In 2013, Xiao et al. focused on the mass reduction of an automotive steel wheel by means of applying a multi-objective topology optimization approach to address stiffness and eigenfrequency requirements [32]. Application of this method yielded a wheel design with improved dynamic frequency properties and a mass reduction of 4.57 percent (0.15 kg) when compared to the initial design [32]. The manner in which all loads and constraints were applied to the computational wheel model during topology optimization and *FEA* was verified by means of a benchmark comparison between physically measured strain gage data and the computational finite element analysis of a commercially available steel wheel. This strain gage data utilized by Xiao et al. was measured according to applied radial loads only [32]. Loads representing tyre pressure, lateral cornering, and torsion were not considered. In this dissertation, these loads were included and investigated.

The constraints governing the topology optimization as defined by Xiao et al. included the angle of cyclic symmetry and minimum member size of the wheel model [32]. Cyclic symmetry concerns itself with the number of times a geometrically defined pattern is periodically repeated about some axis. As the component optimized in this dissertation was a wheel, a cyclic symmetry constraint was applied about its axis of rotation to essentially define a spoke number [32].

The minimum member size constraint defined during topology optimization controls the smallest permissible voxel size in order to reduce the effect of numerical problems including mesh dependency, and a checkerboard like distribution of material which may deem the design impossible to manufacture [32]. Voxels which are smaller than the specified minimum member size may be present in a structural topology optimization solution if they are critical to the defined load path [32].

Xiao et al. found that as the applied minimum member size increases, the produced material distribution becomes more clearly defined and less scattered; however, increasing the minimum member size too much may eradicate necessary structural details [32]. Xiao et al. determined that an optimum minimum member size of 15 mm should be applied to a model such as a wheel

by means of a comparison between material distributions obtained by applying minimum member size constraints of 5, 10, 15, 30, 60, and 80 mm to the model [32].

As reviewed by Brackett et al. in 2011, the determination of optimum minimum member size is usually a complex procedure most often dependent on the intended component scale and manufacturing process [39]. Brackett et al. focused primarily on the use of additive manufacturing processes to produce designs achieved through structural topology optimization techniques [39]. It was put forward by Brackett et al. that manufacturing processes such as 3D printing are best suited to producing topology optimization designs which are not restricted by manufacturing constraints associated with traditional manufacturing processes [39].

Adversely, the work presented by Satya Prasad et al. in 2013 did not focus on the manufacturability of the produced geometry, but rather on achieving a solution which did not fail when subject to radial fatigue testing, lateral fatigue testing, dynamic stiffness testing, and impact testing [40]. This work demonstrated the broad array of design criteria which may be specified in a topology optimization problem to produce component designs which satisfy stringent international safety standards.

The influence of topology optimization on the fatigue life of components has also been addressed in literature. In 2014, Das performed a purely computational *FEA* and topology optimization of an automotive aluminium alloy wheel to yield a 52 percent (13.85 kg) reduction in component mass [26]. The effects of altering the applied cyclic symmetry constraints were not considered by Das; rather, the number of cyclically symmetric wheel sections was maintained constant at five. The optimization by Das was performed according to a static *FEA* which considered applied radial, lateral, and bending loads only [26]. The corresponding load cases were applied at two sections of the wheel model; these sections were positioned at 36° apart from one another so as to induce load in the direct line of a wheel spoke, and exactly mid-way between two of the wheel spokes. Das went on to perform a computational damage analysis of the optimized wheel model to prove that the mass reduction

obtained through structural topology optimization can have a negligible effect on the service life of components [26].

While structural topology optimization techniques are utilized most extensively in the mass reduction of mechanical components, they have also been utilized to determine suitable component dimensions. In 2013, Kumar et al. utilized structural topology optimization software to determine the flange thickness of cast aluminium automotive wheel rims below which crack initiation would occur [18]. Kumar et al. defined the governing optimization constraint as the percentage of plastic strain induced as a result of impact testing [18].

In this dissertation, structural topology optimization techniques were utilized as a tool to produce a suitable eco-car wheel geometry which was later modelled and optimized as a composite component. It is the researcher's belief that this sequential application of topology and composites optimizations had not before been utilized in the design of a wheel.

2.5 Composites optimization

This section highlights the relevant theory and literature pertaining to the optimization of composite structures for the purpose of mass reduction. Degenhardt et al. stated that the mass reduction of structural components is particularly important to the space and aerospace industries to lower operating costs and fuel consumption [41]. One way in which such mass reduction may be achieved is through the use of composite materials in the design of lightweight components [41]. At present (2017), the use of composite materials in commercial mechanical design is seeing an annual growth of ten percent owing to the low density and anisotropic material properties of composite materials which may be manipulated to meet design requirements [41]. These anisotropic material properties were regarded by Zhou et al. as making composite materials extremely well suited to optimization technologies [42].

However, as with all optimization, the understanding of what exactly is being optimized is required before understanding the manner in which optimization is

achieved. Therefore, composite materials and their properties are discussed in the following subsection.

2.5.1 Composite material properties

A composite material is the result of a macroscopic combination of different materials to form a structural unit of greater strength and stiffness than its individual constituents [7]. The composite materials utilized in this dissertation consisted of continuous carbon fibre tows arranged in a unidirectional fashion and embedded in an epoxy based resin matrix by means of hand-layup and vacuum bagging techniques. As such, the literature reviewed in this section is particular to carbon-epoxy laminae in order to aid in accurate composites analysis and optimization according to real world scenarios.

The key factors contributing towards this include accurately defined loading, constraints, and material properties. The manner in which accurate material properties may be determined to perform a computational linear static composite *FEA* and optimization by means of the *Altair* software suite is discussed in this section. These material properties included the following:

I. ρ_{ply} Lamina mass density

II. E_1 Elastic modulus in fibre direction

III. E_2 Elastic modulus transverse to fibre direction

IV. v_{12} Poisson coefficient specific to the plane of the lamina

V. G_{12} Shear Modulus specific to the plane of the lamina

Since composites are often utilized in the design of lightweight components, the mass density of a single lamina is discussed first. The *Rule of Mixtures* is often used to analytically determine the mass density of a single lamina by means of the below equation [43].

$$\rho_{ply} = \rho_f \cdot V_f + \rho_m \cdot V_m$$

(2.5.1)

Where:

ρ_{ply} represents the mass density of a single lamina

ρ_f represents the mass density of the reinforcement fibres only

V_f represents the reinforcement fibre volume fraction

ρ_m represents the mass density of the matrix only

V_m represents the matrix volume fraction (1-V_f) assuming no voids

In *Equation 2.5.*1, the term *volume fraction* refers to the volumetric proportion of a particular constituent's presence within the composite mixture represented as a percentage. The volume fractions of the reinforcement fibres and matrix are defined according to the following *Equation 2.5.2* and *Equation 2.5.3* [43].

$$V_f = \frac{Reinforcement\ fibre\ volume}{Lamina\ volume}$$

<div align="right">(2.5.2)</div>

<div align="center">And</div>

$$V_m = \frac{Matrix\ volume}{Lamina\ volume}$$

<div align="right">(2.5.3)</div>

Where:

V_f represents the reinforcement fibre volume fraction

V_m represents the matrix volume fraction

An additional volume fraction may be defined to account for the presence of voids within the composite. However, porosity is generally disregarded owing to its usually low magnitude of less than one percent [43].

The volume fractions defined in *Equation 2.5.2* and *Equation 2.5.3* are commonly used in the analytical determination of a broad array of composite

material properties; however, this sort of conventional analytical approach, while often regarded as acceptable, tends to produce results which represent the maximum attainable material properties rather than the actual material properties [1].

A supporting example of this may be seen in the analytical determination of the transverse tensile strength of a composite lamina reinforced by means of continuous fibres according to *Equation 2.5.4* [1].

$$F_{2t} = \sqrt{\frac{G_{Ic}}{1.12^2 \cdot \pi \cdot \left(\frac{t_t}{4}\right) \cdot 2 \cdot \left(\frac{1}{E_2} - \frac{v_{12}^2 \cdot E_2^2}{E_1^3}\right)}}$$

(2.5.4)

Where:

F_{2t} represents transverse tensile strength of a composite lamina

G_{Ic} represents fracture toughness

t_t represents the transition thickness of carbon-epoxy composites

E_2 represents the transverse elastic modulus of a single lamina

v_{12} represents the Poisson coefficient of a single lamina

E_1 represents the longitudinal elastic modulus of a single lamina

The described failure mechanism resulting from transverse tension may be seen as a fracture mechanics problem in which a crack propagates and grows in the principal fibre direction to split the lamina [1]. When multiple laminae are stacked to form a composite laminate, the transverse tensile strength of each lamina changes as a result of constraints induced by the adjacent laminae [1]. Consequently, the transverse tensile strength of a lamina changes with the properties and orientation of the adjacent laminae. As a result, the governing material property should rather be seen as fracture toughness corresponding to crack propagation and growth [1].

To support the inaccuracy associated with the analytical determination of composite material properties, Barbero stated that the empirical equations published in literature are often applicable to very particular cases only since they are not derived according to the principles of fracture mechanics [1]. A more accurate and reliable means of obtaining the lamina properties required for computational analysis is through physical measurements performed on multiple test samples [1]. The following table shows each required material property and the corresponding *ASTM* standard which may be used to accurately measure it.

Table 2 - Composite material properties and corresponding ASTM testing standards as adapted from Barbero [1]

Material property		Testing standard
E_1	Elastic modulus in fibre direction	ASTM D3039
E_2	Elastic modulus transverse to fibre direction	ASTM D3039
v_{12}	Poisson coefficient	--
G_{12}	Shear modulus	ASTM D5379
F_{1t}	Longitudinal tensile strength	ASTM D3039
F_{2t}	Transverse tensile strength	ASTM D3039
F_{1c}	Longitudinal compressive strength	ASTM D695/ASTM D3410
F_{2c}	Transverse compressive strength	ASTM D695/ASTM D3410

Accurate experimental measurement of the above composite material properties is often extremely time consuming and expensive. In response to this, Tsai et al. proposed in 2014 an invariant based method for determining the stiffness properties of unidirectional laminae if the longitudinal tensile modulus of the lamina is known [12]. Use of this method requires physical measurement of the elastic modulus in the fibre direction alone, and claims that the inaccuracy of material properties determined by means of this method is 1.3 percent as opposed to the approximate inaccuracy of 3 percent obtained through proper physical measurement [12].

The underlying principle behind the method put forward by Tsai et al. is the evaluation of the normalized trace of the lamina's plane stress stiffness matrix as a material property [12]. Here, the plane stress stiffness matrix may be written to show the relationship between stress and strain in *Equation 2.5.5*.

$$\begin{Bmatrix} \sigma_x \\ \sigma_y \\ \sigma_s \end{Bmatrix} = \begin{bmatrix} Q_{xx} & Q_{xy} & 0 \\ Q_{yx} & Q_{yy} & 0 \\ 0 & 0 & Q_{ss} \end{bmatrix} \begin{Bmatrix} \varepsilon_x \\ \varepsilon_y \\ \varepsilon_s \end{Bmatrix}$$

(2.5.5)

The trace of the above stiffness matrix Q, defined as the sum of the diagonal terms, may be determined by dividing the experimentally measured principal elastic modulus by a universal constant of 0.88 [12]. This universal constant was determined by Tsai et al. during the physical testing of laminate samples to develop the invariant based method [12]. Once the trace of the stiffness matrix describing the composite material is known, all of its constituent components may be solved according to *Equation 2.5.6* [12].

$$Q_{ij} = Tr \cdot Q_{ij}{}^*$$

(2.5.6)

Where:

Q_{ij} represents a component of the stiffness matrix Q

Tr represents the trace of the stiffness matrix Q

$Q_{ij}{}^*$ represents the corresponding component of the stiffness belonging to a master ply

The term *"master ply"*, as seen above, refers to a theoretical composite ply whose trace-normalized stiffness components are taken as the median of those determined by Tsai et al. corresponding to ten different types of carbon-epoxy laminates tested [12]. The values of these trace-normalized stiffness components are shown in *Figure 15* as published by Tsai et al. [12].

Trace normalized plane stress stiffness components and engineering constants.										
Material	E_x (GPa)	E_y (GPa)	v_x	E_s (GPa)	Q_{xx}^*	Q_{yy}^*	Q_{xy}^*	Q_{ss}^*	Tr (GPa)	Q_{11}^* (45)
IM7/977-3	191	9.94	0.35	7.79	0.8825	0.0459	0.0161	0.0358	217.8	0.2759
T800/Cytec	162	9.0	0.4	5.0	0.8955	0.0497	0.0199	0.0274	182.5	0.2736
T700 C-Ply 55	121	8.0	0.3	4.7	0.8746	0.0578	0.0173	0.0338	139.2	0.2756
T700 C-Ply 64	141	9.3	0.3	5.8	0.8713	0.0575	0.0172	0.0356	162.8	0.2764
AS4/3501	138	8.96	0.3	7.1	0.8567	0.0556	0.0167	0.0438	162	0.2803
IM6/epoxy	203	11.2	0.32	8.4	0.8791	0.0485	0.0155	0.0362	232.2	0.2758
AS4/F937	148	9.65	0.3	4.55	0.8878	0.0579	0.0174	0.0271	167.7	0.2723
T300/N5208	181	10.3	0.28	7.17	0.8805	0.0501	0.0140	0.0347	206.5	0.2744
IM7/8552	171	9.08	0.32	5.29	0.8972	0.0476	0.0152	0.0276	191.6	0.2714
IM7/MTM45	175	8.2	0.33	5.5	0.9014	0.0422	0.0139	0.0282	195.1	0.2711
Std dev	25.9	1.0	0.034	1.4	0.013	0.0056	0.0018	0.0054	28.5	0.0028
Coeff var %	15.9	10.2	10.7	22.4	1.5	10.9	10.9	16.4	15.4	1.0
Master ply					0.8815	0.0499	0.0164	0.0342	185.7	

Note: Each trace-normalized parameter is defined as the respective parameter divided by the trace of the plane stress stiffness matrix.

Figure 15 - Normalized-trace master ply stiffness matrix components as published by Tsai et al. [12]

The material properties describing the stiffness of a composite material may be determined by merely expanding each of the components of the stiffness matrix Q.

These stiffness matrix components are shown alongside their expanded form below.

$$\begin{Bmatrix} \sigma_x \\ \sigma_y \\ \sigma_s \end{Bmatrix} = \begin{bmatrix} Q_{xx} & Q_{xy} & 0 \\ Q_{yx} & Q_{yy} & 0 \\ 0 & 0 & Q_{ss} \end{bmatrix} \begin{Bmatrix} \varepsilon_x \\ \varepsilon_y \\ \varepsilon_s \end{Bmatrix} = \begin{Bmatrix} \sigma_{11} \\ \sigma_{22} \\ \sigma_{12} \end{Bmatrix} = \begin{bmatrix} \frac{E_{11}}{\Delta} & \frac{E_{22} \cdot v_{12}}{\Delta} & 0 \\ \frac{E_{22} \cdot v_{12}}{\Delta} & \frac{E_{22}}{\Delta} & 0 \\ 0 & 0 & G_{12} \end{bmatrix} \begin{Bmatrix} \varepsilon_{11} \\ \varepsilon_{22} \\ \varepsilon_{12} \end{Bmatrix}$$

The elastic material properties determined by means of the invariant based normalized-trace theory put forward by Tsai et al. describe the way in which a unidirectional composite lamina will respond when influenced by external loading. However, these properties do not describe the ultimate strengths of the material which govern failure.

Failure of composite laminates may be defined using various interactive and non- interactive failure theories, examples of which include the Tsai-Wu and maximum strain failure theories [44]. These failure theories have been utilized to predict both first ply failure and last ply failure, the latter being achieved through the application of degraded ply properties [44]. Generally, first ply failure is defined as the initiation of micro-cracking within the laminate; however, this phenomenon is extremely complex to measure experimentally [44]. Furthermore, composite laminates are still capable of carrying load until the

point of last ply failure [44]. An invariant based omni-strain envelope may be utilized to predict laminate failure regardless of the laminate construction [44]. Tsai et al. found that the anchor points (*Figure 16 (a)* to (*d*)) of omni envelopes describing last ply failure produced by means of both interactive and non-interactive failure theories become coincident as the applied degradation factor approaches zero [44]. As such, Tsai et al. produced a simplified failure envelope applicable to all unidirectional composite laminae presented as a unit circle shown in *Figure 16*.
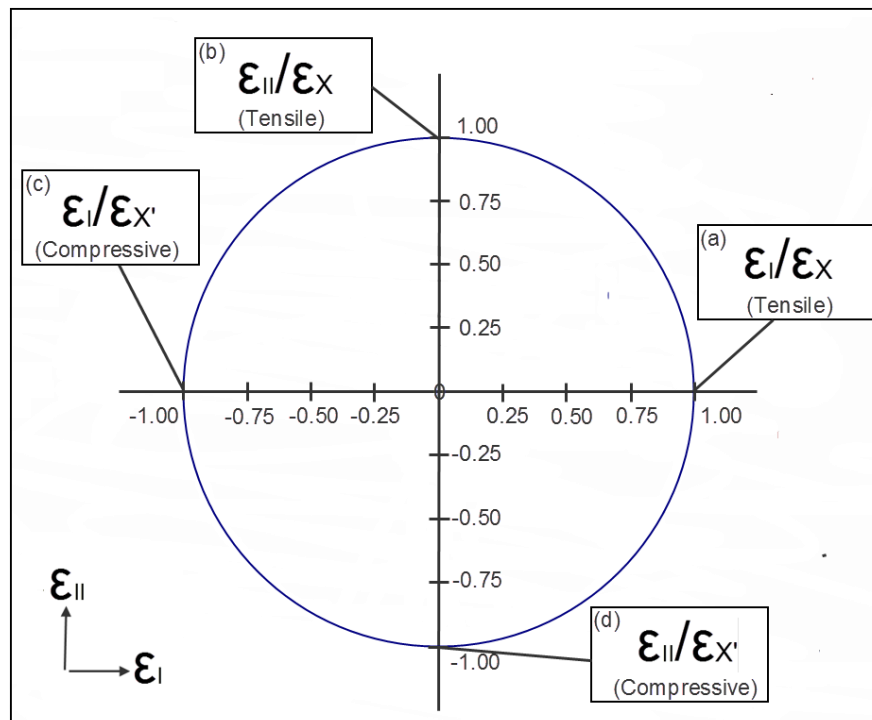
Figure 16 - Unit circle failure envelope as adapted from Tsai et al. [44]

The anchor points of the unit circle failure envelope are attainable by multiplying each unit value by its corresponding strain to failure as measured in uniaxial tension and compression testing [44]. While this failure envelope is slightly conservative, it offers both simplicity, and a reduced number of required inputs and material tests.

The material properties defined in this section were utilized in the computational analyses and composites optimizations performed in this dissertation to closely represent real world behaviour. Therefore, the composites optimization process is outlined in the following sub-section.

2.5.2 Composites optimization process

The optimization of composites is an ongoing field of research which has been addressed by numerous researchers in literature. An example of such a contribution includes the development of the Discrete Material Optimization (*DMO*) method presented by Stegmann et al. in 2005, in which both material selection and orientation problems could be solved based on the ideas of multiphase topology applied to composite shell structures [45]. This method sees the optimization of a composite laminate take the form of a material selection problem for each super-ply within the model. The term *super-ply* refers to the grouping of laminae with the same orientation to form a single lamina of equivalent thickness to the sum of the individual lamina thicknesses of which it is comprised [38,46].

Chen et al. produced a new method for the optimization of lamina stacking sequences by means of bi-level approximation and genetic algorithms [47]. Genetic algorithms were also utilized in 2005 by Toropov et al. to optimize the mass and manufacturability of composite aircraft wing ribs subject to manufacturing constraints [48]. Toropov et al. found that a mass reduction of between 12 and 36 percent was achievable depending on the applied manufacturing constraints [48].

Huang et al. developed another optimization approach addressing the microstructure of cellular or composite materials to achieve a macrostructure of maximum stiffness for a given fibre volume fraction [49]. This was achieved through the integration of the elastic properties of a material with periodic microstructure into the computational analysis of the component macrostructure based on a combined application of homogenization theory and sensitivity analysis to gradually redistribute the material base cell constituents [49].

In 2015, Allaire et al. studied the optimization of laminated composite plates by means of applying a level-set method in which the stacking sequence and in-plane geometry of composite laminae were varied [50]. This method relied on the decomposition of applied constraints into a single marginal constraint function to establish a bi-level optimization problem addressing an inner level

combinatorial stacking sequence optimization, and an outer level topology and geometry optimization of each lamina [50]. The inner level combinatorial stacking sequence optimization relied on an iterative approximation method to solve a set of linear integer problems associated with the marginal constraint function [50]. The outer level optimization combined a level-set method to describe the interfaces of laminae and the *Hadamard Method* to vary lamina boundaries through the computation of shape gradient [50]. However, of particular relevance to this study is the multiphase composites optimization process consisting of free size, sizing, and shuffling optimizations as utilized by *Altair HyperWorks*.

An early version of free size optimization of shell structures was researched in 1960 by Lucien Schmit, and is seen as the earliest form of structural optimization [46]. Schmit's version of free size optimisation applied to shell structures was superseded by the introduction of design variable linking in 1974; however, these early versions of structural optimization were limited due to a lack of computational power [46]. Further work was contributed to free size optimization in 1989 through Pedersen's study of simplified composite laminate models [46]. These laminate models comprised of individual shell elements each having a single fibre orientation which was allowed to vary continuously during optimization [46]. Pederson, in 1991, suggested that the optimization of element thickness could be combined with the optimization of fibre orientation to greatly improve laminate stiffness by allowing the model to achieve uniform energy density in conjunction to altering stress distribution [51].

Currently, *Altair HyperWorks* utilizes free size optimization techniques to continuously vary the thickness of shell elements representing each super-ply, so as to remove redundant material, add reinforcement material, and highlight reinforcement patch areas [52]. This is typically performed during the concept design and initial optimization phase of the composite material layup [46].

A generalized version of the fore-mentioned free-size optimization applied to composite material layups may be stated as per *Equation 2.5.7* [35]:

$$min\ f(x)$$
$$s.t.:\ g_j(x) - \ g_j{}^u \ \leq 0, \quad j = 1, \dots, M$$
$$X_{ik}{}^L \ \leq \ X_{ik} \ \leq \ X_{ik}{}^L, \qquad i = 1, \dots, Np, \quad k = 1, \dots, NE$$

<div align="right">(2.5.7)</div>

Where:

$f(x)$ represents a general form of the objective function

X_{ik} represents the thickness of the ith super-ply of the kth element

Np represents the total number of super-plies

NE represents the total number of elements

The constraints applicable to the above minimization of the objective function are representative of possible manufacturing and design rules or decisions [46]. Examples of such constraints include the total laminate thickness and percentage contribution of a single fibre orientation to the total laminate thickness [35]. These constraints may be stated as follows [35]:

$$T_k{}^L \ \leq \ \sum_{i=1}^{Np} X_{ik} \ \leq \ T_k{}^U, \quad k = 1, \dots, NE$$

<div align="right">(2.5.8)</div>

<div align="center">And</div>

$$P_j{}^L \leq \ \frac{X_{jk}}{\sum_{i=1}^{Np} X_{ik}} \ \leq \ P_j{}^U, \ j = 1, \dots, Np, \qquad k = 1, \dots, NE$$

<div align="right">(2.5.9)</div>

Where:

T_k represents thickness of the laminate

P_j represents the percentage of a single orientation to the total laminate thickness

The second part of the multiphase optimization of composite material layups addresses the number of laminae required for each lamina shape and fibre orientation [53]. This process essentially addresses a size optimization problem in which the geometry of individual lamina groups remains constant while the thickness of each group is minimized [53]. The optimum thickness of each lamina group is obtained by means of simulation of the addition or removal of laminae; it is, therefore, a discrete process referred to as sizing optimization [46,53].

The final part of the multiphase optimization of composite material layups addresses the stacking sequence of all laminae within the composite in order to maximize its structural performance characteristics across various load cases [53]. Altering the stacking sequence of composite laminae produces changes in the structural integrity of a component including [53]:

I.   Bending stiffness

II.   Torsional stiffness

III.   Stress factors

IV.   Component strain

V.   Reserve factor

Optimization of the composite laminae stacking sequence provides a user with the optimized ply book recipe to be utilized during manufacture; therefore, it is important that all phases of composite material optimization adhere to the specific manufacturing constraints identified by the user at the beginning of this multiphase process [46].

The above-mentioned process produces efficiently detailed and optimized results. It should be noted, however, that the efficiency of this multiphase process is dependent on user interpretation of the obtained lamina geometry [53]. Patten put forward that although the results obtained through this process are regarded as optimum, it is possible to lighten the design further through the addition of plies and enhancement of lamina geometry complexity; however,

doing so may render the design infeasible with respect to cost and manufacturability [53]. As such, the following topics of further research were identified by Patten to enhance the process described in this section [53]:

I.   The inclusion of lamina strain targets in sizing and shuffling optimization

II.   The coupling of composite material optimization to the alteration of stringer shapes in aircraft wings

III.   The effects of subjecting the optimization process to a broader set of load cases

IV.   The inclusion of lamina drop off targets to prevent large changes in thickness between adjacent elements

V.   The iteration of sizing and shuffling optimization to further reduce component mass

2.5.3 Composites optimization of mechanical components

Various mechanical components have been subject to the application of composites optimization techniques in recent literature. In 2014, Hong et al. optimized a composite bicycle wheel rim using the commercially available *Altair HyperWorks* software suite [27]. However, the study performed by Hong et al. focused on determining the optimum stacking sequence of a composite bicycle wheel rim connected to the hub using wire spokes according to a minimized Tsai-Wu failure index [27].

Composites optimization has also been performed on the basis of other optimization functions, an example of which may be seen in the work put forward by Patten in 2009 [53]. In this study, Patten applied composites optimization techniques to a composite aircraft wing to increase stiffness while reducing mass [53]. Similarly, further use of composites optimization in the aerospace industry was seen in the optimization of another aircraft wing structure as discussed by Zhou et al., and the commercial incorporation of the composites optimization process to aerospace component designs by *Bombardier* [42].

It is apparent that the optimization of composite structures is being increasingly adopted by various industrial and research based entities. However, it appears that the composite components optimized in literature are very rarely taken further than a purely computational basis. Therefore, this study aimed to contribute to this effort by applying composites optimization to a purpose built wheel model whose predicted *FEA* strain behaviour was compared against that of its physically manufactured counterpart.

2.6 Chapter summary and conclusion

The literature reviewed in this chapter indicated that the wheel has been considered as one of the most important load bearing components in automotive transportation for nearly five and a half centuries. During this period, various research efforts have focused on improving the design of wheels by combining enhanced strength and durability characteristics with reduced component mass. Currently, efforts are still being made to improve the design of modern wheels while contributing to the body of knowledge surrounding their behaviour as load bearing components.

It was indicated that although *FEA* software is utilized extensively in the design of modern commercial wheels, it has not entirely replaced physical testing. Modern wheels are required to undergo physical testing according to stringent international safety standards for the purpose of investigating whether or not they will fail as a result of the loading which they experience during operation. This loading was identified as a combination of radial, lateral and torsional forces resulting from vehicle motion, as well as pressure resulting from tyre inflation. Additionally, it was shown that the magnitude of each of these loads can be determined using classical mechanics equations.

The previous work done on the *FEA* of wheels indicated that in most cases, they were modelled using linear-elastic material properties, and analysed according to static loading scenarios. These analyses corresponded to linear static type *FEA*s. The *FEA*s and optimizations performed in this dissertation were of a linear static nature.

The stages of performing a linear static *FEA* in which error is most commonly introduced by the user were identified as the discretization, assignment of material properties, and the application of loads and constraints to the model. Literature indicated that the error associated with geometric approximation resulting from discretization could be reduced if second order parabolic elements were utilized instead of first order linear elements. Reducing this error could improve the accuracy of results obtained through *FEA*. The *FEA* and optimization models in this dissertation were discretized into second order parabolic elements.

Additionally, literature indicated that the behavioural characteristics of tyres are mathematically complex and not included in linear-static *FEA*s performed on wheel models. Although loads are transferred to the wheel through the tyre, it was shown that accurate *FEA* results could be obtained if loading was applied directly to the wheel model rim. In previous research, pressure was most commonly represented as an evenly distributed force acting normal to the surfaces affected by it. The most common method utilized to represent radial, lateral, and torsional loading in previous wheel *FEA*s was shown to be by means of a point load applied to a small section of the wheel rim model circumference. These wheel models were constrained by restricting all 6 degrees of freedom at the nodes in the wheel hub bore or bolt holes (depending on the type of wheel being analysed). These methods were utilized to represent the applied loads and constraints in the *FEA*s and optimizations performed in this dissertation.

Additionally, literature indicated that structural topology optimization software has been utilized to reduce the mass of modern commercial wheels by producing efficient distributions of isotropic material within a specified domain. It was mentioned that although designs produced using structural topology optimization software tend to favour additive manufacturing processes such as 3D printing, constraints can be specified by a user to ensure that the produced results may be manufactured using alternative processes.

A manufacturing constraint applicable to this dissertation was identified as a "*split-draw*" constraint. This constraint was utilized to ensure that the wheel

designs produced using structural topology optimization software could be manufactured as moulded components. This was important as the optimum wheel design produced through structural topology optimization in this dissertation was later modelled and optimized as a moulded composite component. It was indicated that this constraint could be applied as either a 'Hole Allowed' or 'No Hole' variant. Both variants were applied in this dissertation.

Additional variables influencing the results produced through the structural topology optimization of wheels were identified as the objective optimization function, safety factor, target design volume, number of cyclic symmetry degrees, and minimum member size. Previous work done on the structural topology optimization of wheels indicated that the optimum minimum member size corresponded to 15mm. In this dissertation, a minimum member size of 15 mm was utilized.

Literature indicated that the mass of wheels has been reduced through the utilization of different materials, and that the composite components can be significantly lighter than metallic components of the same geometry. It was also indicated that the material properties of a carbon fibre laminate can be easily determined using an invariant based normalized trace theory. Additionally, it was shown that this theory has been proven to produce accurate results, and requires that only tensile testing be performed on a test sample in the principal fibre direction. Literature indicated that the failure of a composite laminate can be easily evaluated according to last ply failure by using a unit circle failure envelope. Both the invariant based normalized trace theory and unit circle failure criteria were utilized in this dissertation.

Lastly, it was indicated by literature that significant mass reduction has been achieved through using composites optimization software to optimize the shape and stacking sequence of laminae within a composite component. However, it appeared that the results produced using composites optimization software were very rarely manufactured and tested to investigate whether or not they behaved as predicted.

It seems that structural topology and composites optimization software packages have never been utilized sequentially in the design of a wheel. These optimization techniques were utilized sequentially in this dissertation. The optimized composite wheel produced in this way was physically manufactured and tested to investigate whether or not it behaved as predicted.

Chapter 3: Research method

3.1 Introduction

Wheel functionality is usually addressed by ensuring that wheel designs meet the requirements of stringent safety standards. Although, while such standards ensure that commercial automotive wheels possess enough structural integrity to be deemed safe, no such standards exist to govern the design of purpose built eco-car wheels. As such, an alternative approach was utilized to ensure that the wheel designs produced by means of the optimization techniques applied in this dissertation were sufficiently suited to performing their intended function.

The primary function of a wheel is to transfer load between the ground and vehicle to which it is attached. Additionally, the wheel should maintain sufficient structural integrity to be capable of rotating during the transfer of such load. Therefore, component functionality was evaluated by considering the measurement of an entity which is representative of both failure and structural integrity.

In considering the aspect of component failure, the unit circle failure envelope put forward by Tsai et al. presented an accurate and simplified approach to predicting the failure of any unidirectional carbon fibre laminate. This failure envelope exists in strain space, and therefore, requires that only component strain be evaluated to predict failure. Additionally, the structural integrity of a component may be evaluated by means of stiffness. Currently, the wire-spoked aluminium wheels utilized on the *Nelson Mandela University Eco Car* are sufficiently stiff to transfer the loads induced by driving between the ground and vehicle. Therefore, it was required that the wheel designs produced by the sequentially applied optimization techniques in this dissertation were at least as stiff as these. The literature reviewed in sections *2.3.1* and *2.4.1* of *Chapter 2* indicated that component stiffness governs the resultant displacement induced by an applied force. As strain is representative of the ratio between displaced

length and original length, it served as a suitable means of evaluating component stiffness in this dissertation.

Therefore, the experimental method followed in this dissertation focused on the measurement of component mass as well as the strain behaviour induced by normal eco-car driving conditions for the purpose of establishing a fair comparison between the wheel designs produced by means of the sequentially applied structural topology and composites optimization techniques. The four major sequential stages of the research method followed in this dissertation, each of which is discussed in detail in the following sub-sections, include:

I.   Establishment of benchmark strain behaviour

II.   Verification of computational analysis methods

III.   Design of wheel through structural topology optimization

IV.   Design of wheel through composites optimization

3.2 Establishment of benchmark strain behaviour

The existence of any comparison relies on the establishment of some reference state against which difference may be evaluated. In this dissertation, the mass and induced strain behaviour of wheel designs produced during the sequential application of structural topology and composites optimization techniques were compared to those of a commercially available wheel of the same diameter. Therefore, it was required that the mass and stiffness properties of the commercially available wire-spoked aluminium wheels currently utilized on the *Nelson Mandela University Eco Car* be determined. As such, the next sub-section addresses the manner in which the physical strain behaviour of these wheels was established to serve as a comparative benchmark by means of the following stages:

I.   Application of strain gages

II.   Application of loading mechanisms

III.   Measurement of induced strains

3.2.1 Application of strain gages

Two 120 Ω *HBM* uniaxial strain gages, *A* and *B,* of 1.5 mm grid length were applied tangentially to the rim of a commercial wheel as shown in *Figure 17*. These strain gages were selected due to availability, and the fact that the uniaxial strains measured with these gages could be easily determined through *FEA* software. They were applied to the wheel rims by using *ASTM E1237-93 R03* as a guideline. The strain gage number and product batch number corresponding to these strain gages are 1-LY41-1.5/120, and 812067057 respectively. Additionally, the accuracy of the strain measurement system was verified as being within 0.80 percent by means of shunt calibration.

Figure 17 - Uniaxial strain gages applied to the rim of a commercial wheel

3.2.2 Application of loading mechanisms

The most commonly considered loading mechanisms relating to the computational analysis and optimization of wheels include:

I.   Pressure

II.   Radial

III.   Lateral

IV.   Torsional

The physical strain behaviour of the commercial wheel rim being tested in this dissertation was established by applying each of these loading mechanisms to

it. The magnitude of each of these loading mechanisms was determined by first measuring the vehicle and driver mass distribution experienced by each wheel on the vehicle (shown in *Table 3*) before applying *Equation 2.2.1* through *Equation 2.2.7*.

Table 3 - Nelson Mandela University Eco Car wheel mass distribution

Wheel	Mass [kg]
Front (Right)	37.00
Front (Left)	35.00
Rear	40.00

In utilizing each of these masses to determine the magnitudes of each loading mechanism produced as a result of vehicle motion, moments were taken about the point *P* (shown in *Figure 18*) to account for mass transfer between the front wheels resulting from vehicle motion through an arc. This mass distribution was determined according to the maximum permissible vehicle velocity through an arc at the instant of slippage between the tyre and ground.
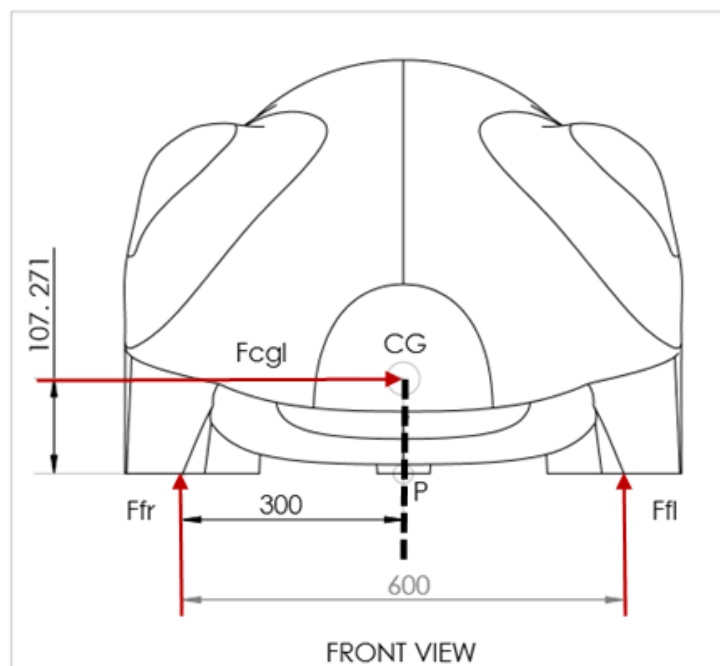
Figure 18 - *Nelson Mandela University Eco Car* **front view for mass distribution during cornering**

The magnitudes of each radial and lateral reaction force determined by means of the above was resolved into components relative to each wheel in order to account for the 8° camber of the front wheels. Consequently, the magnitudes of

the loading mechanisms experienced by the front left wheel were selected with the *Nelson Mandela University Eco Car Team* as being the greatest owing to the influence of the radial and lateral load magnitudes. These magnitudes, along with those experienced by both the front right and rear wheels are presented in *Table 4*.

Table 4 - Resultant loading combination experienced by each wheel during operation

Wheel	Radial Load [N]	Lateral Load [N]	Torsional Load [Nm]
Front (Right)	277.8	234.9	0.4
Front (Left)	500.3	423.0	0.4
Rear	393.5	314.0	59.4

However, these normal and lateral loadings were determined for forward vehicle motion through a clockwise arc (right turn). Therefore, the loads experienced by the front left wheel in such a scenario would be experienced by the front right wheel during vehicle motion through a counter-clockwise arc (left turn). It was not of importance to this dissertation which wheel these loading mechanisms acted on; rather, it was important to note that these loadings would act on the outer-most wheel during vehicle motion through an arc.

Referring to the purpose of this stage of the applied research method, the strain behaviour of the commercial wheel rim was determined for the purpose of establishing a comparative benchmark against which the strain behaviour of all other wheel models produced by means of optimization could be compared. This strain behaviour served as a means of validating the manner in which each of the loading mechanisms was computationally applied during the *FEA*s and optimizations performed in this dissertation. Each of these loading mechanisms was individually applied to the wheel at the various magnitudes presented in *Table 5*. The manner in which each individual loading mechanism was applied to the wheel is presented in the following subsections.

Table 5- Applied physical loads

Pressure [kPa]	Radial Load [N]	Lateral Load [N]	Tangential Load [N]
180.0	111.6	94.4	0.8
200.0	200.0	169.1	1.4
250.0	300.0	253.6	2.1
--	400.0	338.2	2.8
--	500.3	423.0	3.5

3.2.2.1 Pressure loading

Wheel loading by means of tyre inflation pressure was conducted using an analogue tyre pressure gage as shown in *Figure 19*. Additionally, while applying this load, the wheel axle was raised so as to fully suspend the wheel to ensure that the induced strain magnitudes were not influenced by localized tyre deformation.
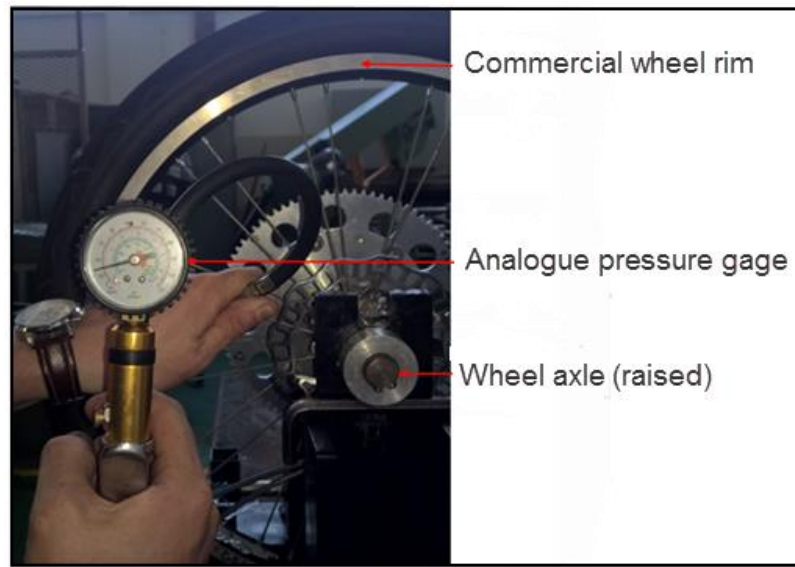
Figure 19 – Analogue pressure gage utilized to inflate the suspended commercial wheel during physical testing

3.2.2.2 Radial loading

Wheel loading by means of applied radial force was conducted by supporting the wheel assembly in a static load test rig and placing known masses on both ends of the wheel axle as shown in *Figure 20*. During this process, the wheel was supported so as to allow free vertical translation of the wheel only. This free vertical translation allowed the applied masses to force the tyre against a part of the test rig referred to as the "*horizontal slide block*" (representing ground) so as to produce a reaction force acting radially through the wheel.
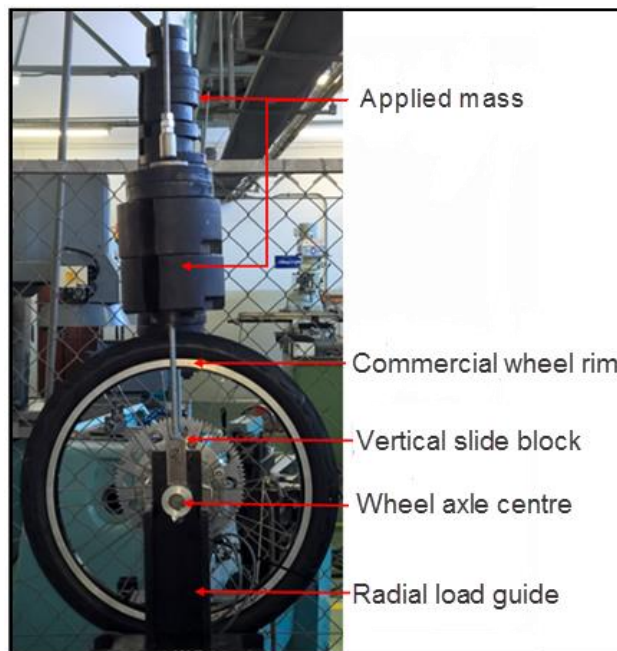
Figure 20 – Physical application of radial loading

3.2.2.3 Lateral loading

Wheel loading by means of applied lateral force was conducted by supporting the wheel assembly in the static load test rig and using a known suspended mass to laterally displace the horizontal slide block shown in *Figure 21*. During this process, the wheel was supported so as to restrict all degrees of freedom at the wheel hub and axle. Additionally, the lubricated horizontal bars of the static load test rig shown in *Figure 21* allowed near free translation of the horizontal slide block representing ground so as to induce a lateral load in the wheel by forcing the flange of the horizontal slide block against the tyre of the wheel.
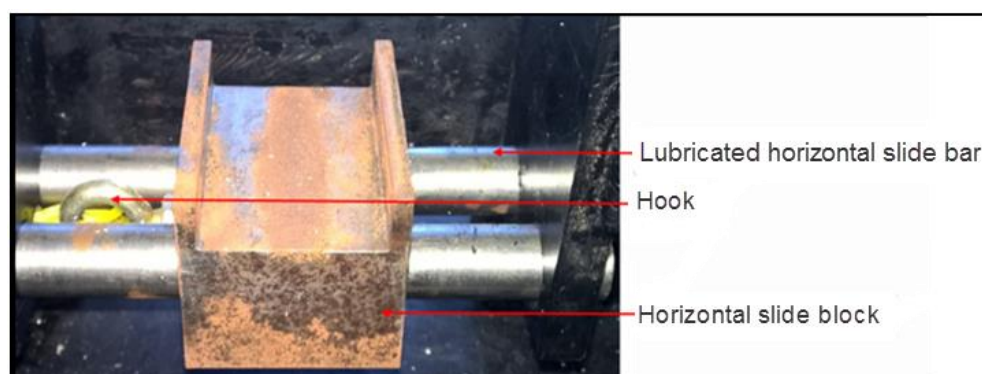
Figure 21- Horizontal bars and slide block of static load test rig

3.2.2.4 Torsional loading

Wheel loading by means of applied torque was conducted by supporting the wheel assembly in the static load test rig and applying a force to the 170 mm diameter sprocket rigidly connected to the wheel axle. This should have induced a 0.4 Nm torque in the wheel being tested. However, in doing so, it was found that the applied torque magnitude was too small to induce any form of measurable wheel rim strain. A larger magnitude of torque was not applied to the wheel as the determined torque magnitude corresponding to the selected loading scenario was 0.4 Nm. As such, loading by means of torque was not considered further in this study.

3.2.2.5 Combined loading

A static combined loading scenario representative of the worst case wheel operating conditions selected with the *Nelson Mandela University Eco Car Team* was created by simultaneously applying the previously mentioned loads (excluding torsion) to the wheel. The magnitudes of the applied loading mechanisms correspond to those as previously determined for the front left wheel and are shown in *Table 6*.

Table 6 - Combined loading constituents and magnitudes

Pressure [kPa]	Radial Load [N]	Lateral Load [N]
200	500	423

3.2.3 Measurement of induced strains

The wheel rim strains induced by each of the loading mechanisms were measured by connecting the 1-LY41-1.5/120 strain gages to a P3 strain amplifier. All measured strains were set to zero before any loading was applied to the wheel. Doing this ensured that the measured physical strains in this dissertation were produced by the applied loading mechanisms alone. Each loading mechanism was then applied to the wheel and the induced strain recorded at tangential strain gage orientations of 0°, 90°, and 180° relative to the tyre-ground contact patch (see *Figure 22*). For the purpose of verifying repeatability, this procedure was conducted a total of 30 times for each

individual loading mechanism according to the magnitudes presented in *Table 5*. Similarly, this process was repeated a total of five times in the case of the applied combined loading scenario at each of the previously stated strain gage orientations.
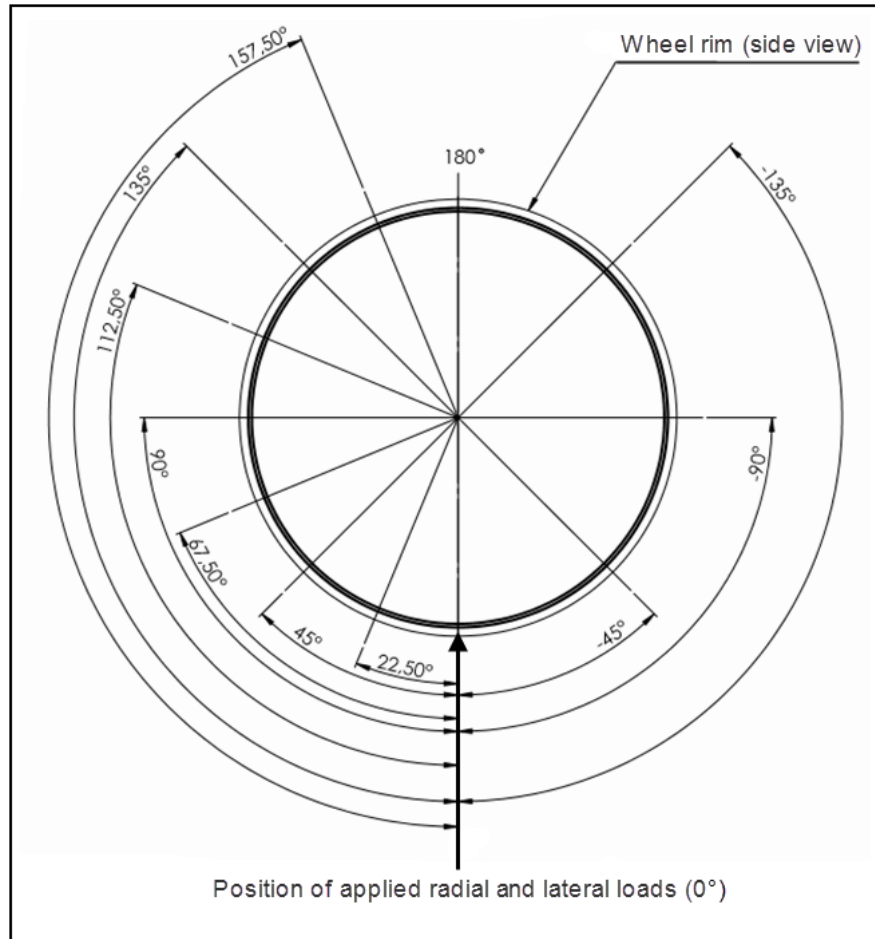
Figure 22 - Tangential strain gage positions utilized during radial loading

The results corresponding to this part of the research method are presented in *Chapter 4*. In the next section, the manner in which computational loads and constraints were applied to the commercial wheel *FEA* model is discussed. The *FEA* strains determined using these applied loads and constraints were compared to the measured physical strains obtained as per the method discussed in this section for the purpose of investigating the quality of the results obtained using the static load test rig, as well as how closely the *FEA* loads and constraints applied in this dissertation represented the physical wheel behaviour.

3.3 Verification of computational analysis methods

The highest degree of error associated with computational *FEA* is introduced by the user during the definition of applied loads and constraints. Since the quality of any result produced by computational optimization is dependent upon these loads and constraints, it is vital that they are truly representative of reality. Therefore, the sole purpose of this research stage was to perform computational *FEA*s which accurately represented the physical strain measurements obtained as per the method described in the previous section.

According to the analysis acceptability criteria of 10 percent allowable deviation between measured physical and *FEA* strains put forward by the *FAA*, the computational analyses performed in this section could be deemed as being acceptably accurate if the predicted *FEA* strain values were within ten percent of the physically induced strains recorded as per the method described in the previous section. Consequently, the methods of computational load and constraint application utilized in the topology and composites optimizations performed in this dissertation could be deemed as credible. Additionally, the wheel designs produced during these optimizations could be seen as being truly and properly optimized according to validated real world conditions. Therefore, this section discusses the computational input required to accurately establish a linear static *FEA* which represented the physical strain measurements performed in the previous section by addressing:

I.   The finite element model

II.   Application of constraints

III.   Application of loading

3.3.1 Finite element model

As per the finite element analysis procedure discussed in section *2.3.1*, a geometric model should be created, discretized, and assigned material properties before being analysed according to externally applied forcing functions and system constraints. Therefore, this subsection addresses the

manner in which these steps were followed during the creation of the commercial wheel model analysed in this section.

3.3.1.1 Creation of geometric model

The computational model forming the subject of this section was created using *Dassault Systèmes SolidWorks 2015 x64 Bit Edition Service Pack 2.1/2* to represent the commercial wheels currently utilized on the *Nelson Mandela University Eco Car*. Similar to the literature reviewed in section *2.3.4* of *Chapter 2*, this model did not include a tyre, and consisted only of the wheel rim, wheel spokes, and wheel hub combined into an assembly model. These components interacted with one another by means of applied contact sets which allowed no penetration between them at the areas in which they were in contact. This geometric wheel model is shown in *Figure 23*.

Figure 23- Computational *FEA* model of commercial wheel (*Dassault Systèmes SolidWorks*)

3.3.1.2 Discretization

The use of second order elements greatly reduces the degree of geometric approximation error associated with curved entities. Therefore, since the models being analysed in this study consisted almost solely of curved entities, a 2nd order curvature based solid tetrahedral mesh was utilized to discretize the commercial wheel model being analysed. Consequently, the model was discretized into 377517 nodes and 194625 elements as shown in *Figure 24*.

Figure 24 - Mesh Properties (Commercial wheel model, *Dassault Systèmes SolidWorks*)

The mesh details shown in *Figure 24* were not representative of a generalized discretization applied to the model only. A linear static *FEA* is solved by means of interpolation between nodes. Therefore, since the predicted strains were of particular importance at the positions corresponding to the physically applied strain gages discussed in the previous section, the nodes at the corresponding positions were refined within the discretized model.

This refinement entailed representing the strain gages applied to the wheel rim during physical testing as "*split lines*" created on the surface of the wheel rim. Once defined, the element size and distance between the nodes existing within the vicinity of these split lines was reduced by the application of a localized mesh refinement of 0.25 mm element size, and 1.5 aspect ratio. This mesh refinement, and its associated properties, are respectively shown in the *Figure 25* and *Figure 26*.
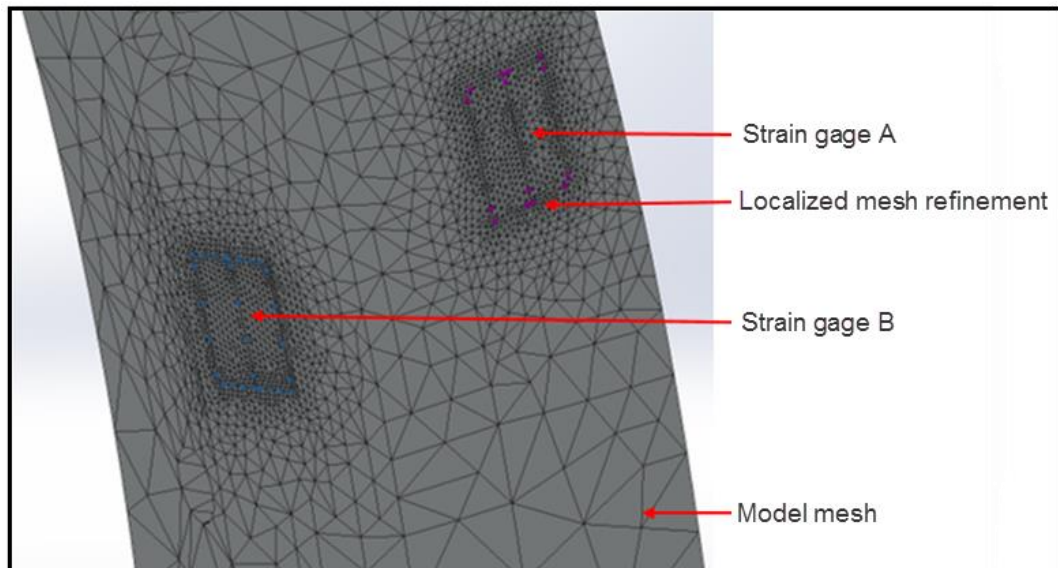
Figure 25 - Mesh refinement at strain gage positions (*Dassault Systèmes SolidWorks*)

Figure 26 - Mesh Refinement properties (*Dassault Systèmes SolidWorks*)

3.3.1.3 Material properties

The linear elastic material properties assigned to the computational model of the 606-T6 Aluminium Alloy wheel rim, 7075-T6 Aluminium wheel hub, and AISI-304 steel wheel spokes are shown in *Figure 27*, *Figure 28*, and *Figure 29* respectively. These properties were utilized as found in the *Dassault Systèmes SolidWorks 2015 x64 Bit Edition Service Pack 2.1/2* material library. Physical material testing would have been performed if the *FEA* strains determined according to the method described in this section did not correlate to the measured physical strains determined as per the method described in section *3.2*.

Property	Value	Units
Elastic Modulus	69000	N/mm^2
Poisson's Ratio	0.33	N/A
Shear Modulus	26000	N/mm^2
Mass Density	2700	kg/m^3
Tensile Strength	124.08	N/mm^2
Compressive Strength		N/mm^2
Yield Strength	55.15	N/mm^2
Thermal Expansion Coefficient	2.4e-005	/K
Thermal Conductivity	170	W/(m·K)
Specific Heat	1300	J/(kg·K)
Material Damping Ratio		N/A

Figure 27 – 6061 Alloy Material Data (Wheel Rim, *Dassault Systèmes SolidWorks*)

Property	Value	Units
Elastic Modulus	72000	N/mm^2
Poisson's Ratio	0.33	N/A
Shear Modulus	26900	N/mm^2
Mass Density	2810	kg/m^3
Tensile Strength	570	N/mm^2
Compressive Strength		N/mm^2
Yield Strength	505	N/mm^2
Thermal Expansion Coefficient	2.36e-005	/K
Thermal Conductivity	130	W/(m·K)
Specific Heat	960	J/(kg·K)
Material Damping Ratio		N/A

Figure 28 - 7075-T6 Material Data (Wheel Hub, *Dassault Systèmes SolidWorks*)

Property	Value	Units
Elastic Modulus	190000	N/mm^2
Poisson's Ratio	0.29	N/A
Shear Modulus	75000	N/mm^2
Mass Density	8000	kg/m^3
Tensile Strength	517.02	N/mm^2
Compressive Strength		N/mm^2
Yield Strength	206.81	N/mm^2
Thermal Expansion Coefficient	1.8e-005	/K
Thermal Conductivity	16	W/(m·K)
Specific Heat	500	J/(kg·K)
Material Damping Ratio		N/A

Figure 29 - AISI-304 Material Data (Wheel Spokes, *Dassault Systèmes SolidWorks*)

3.3.2 Specification of forcing functions

The forcing functions applied to the computational finite element models being analysed and optimized in this dissertation were representative of the externally applied physical loading mechanisms used to establish the benchmark wheel rim strain behaviour. Additionally, they were seen as the loading mechanisms most considered in the literature reviewed *Chapter 2*, namely:

I.   Pressure

II.   Radial

III.   Lateral

IV.   Torsional

The method in which each of these loading mechanisms was applied to the *FEA*s and optimizations performed in this dissertation is outlined in the following subsections. However, before the above is discussed, the matter of considering any induced stress in the *FEA* model resulting from spoke pre-tension should be addressed.

All of the spokes in the commercial wheel tested as per the method described in section *3.2* were equally tensioned by a local business, *Cyclopro.* The measured physical strains in this dissertation corresponded to the effects of applied loading only. That is to say that the strains induced by spoke tensioning during wheel construction were not measured by the physical strain gages applied to the wheel rim in the previous section. To allow for a fair comparison between the measured physical strains in the commercial wheel rim and those determined through *FEA*, spoke pre-tension was not included in the commercial wheel *FEA* model.

3.3.2.1 Modelling of pressure induced loading

Loading by means of tyre inflation pressure was applied to the inner flange walls of the computational wheel rim model being analysed as per the method utilized by Borase et al., Patel et al., Radha et al., and Prasad et al. in the reviewed literature [15,23,25,30]. The inner flange walls to which the pressure load was applied in each analysis are highlighted by blue in *Figure 30*.
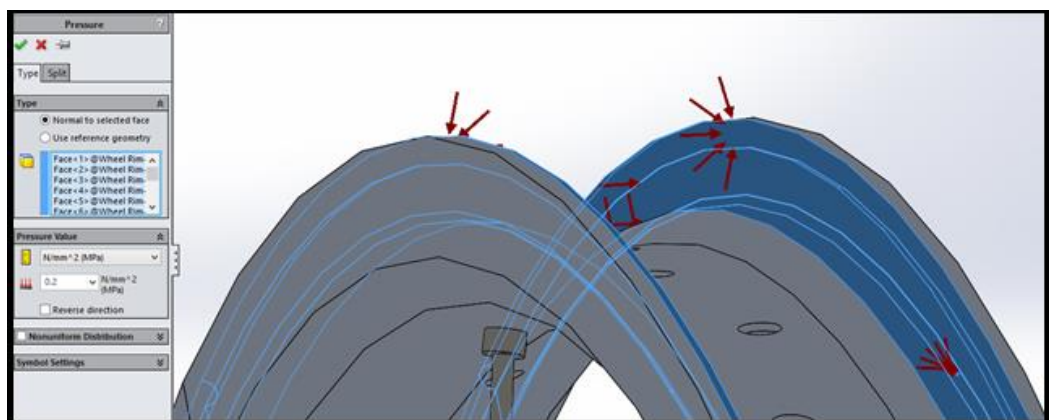
Figure 30 - Applied pressure load for computational analysis (*Dassault Systèmes SolidWorks*)

The induced strains were determined by means of linear static *FEA* according to the following pressure magnitudes:

I.   180 kPa

II.   200 kPa

III.   250 kPa

3.3.2.2 Modelling of radial loading

The wheel rim was radially loaded by means of a *"Remote Load"* applied to a point located at the lateral centre of the wheel rim, and a radial distance of 250 mm from the wheel centre. The position of this point was chosen so as to represent the tyre-ground contact patch. The applied load was connected to the wheel rim model by means of a "*Rigid Connection*" applied to a 24° section of the wheel rim and a 32° section of each inner wheel rim flange bead as shown in *Figure 31*.
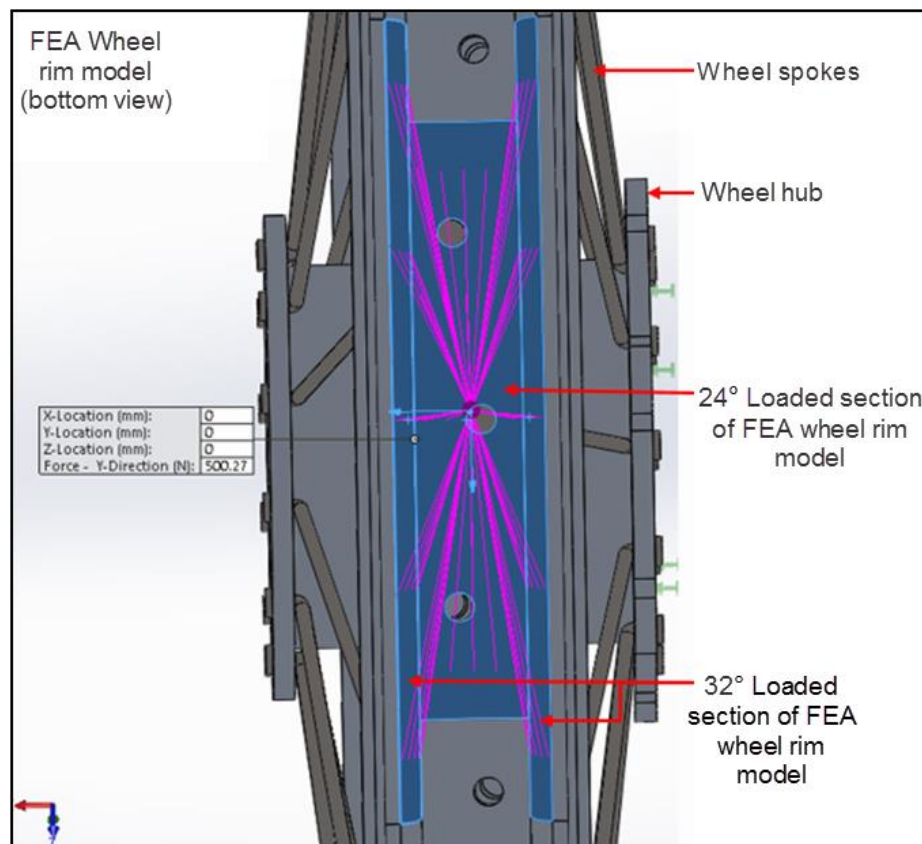
Figure 31 -Bottom view of radial load applied to wheel model (*Dassault Systèmes SolidWorks*)

The induced strains were predicted by means of linear static *FEA* according to the following radial load magnitudes:

I.   111.64 N

II.   200.00 N

III.   300.00 N

IV.   400.00 N

V.   500.27 N

3.3.2.3 Modelling of lateral loading

A lateral load was applied to the wheel model by means of a *"Remote Load"* as per the location and connections discussed in section *3.3.2.2*. *Figure 32* shows the means of lateral loading as applied to computational wheel model.
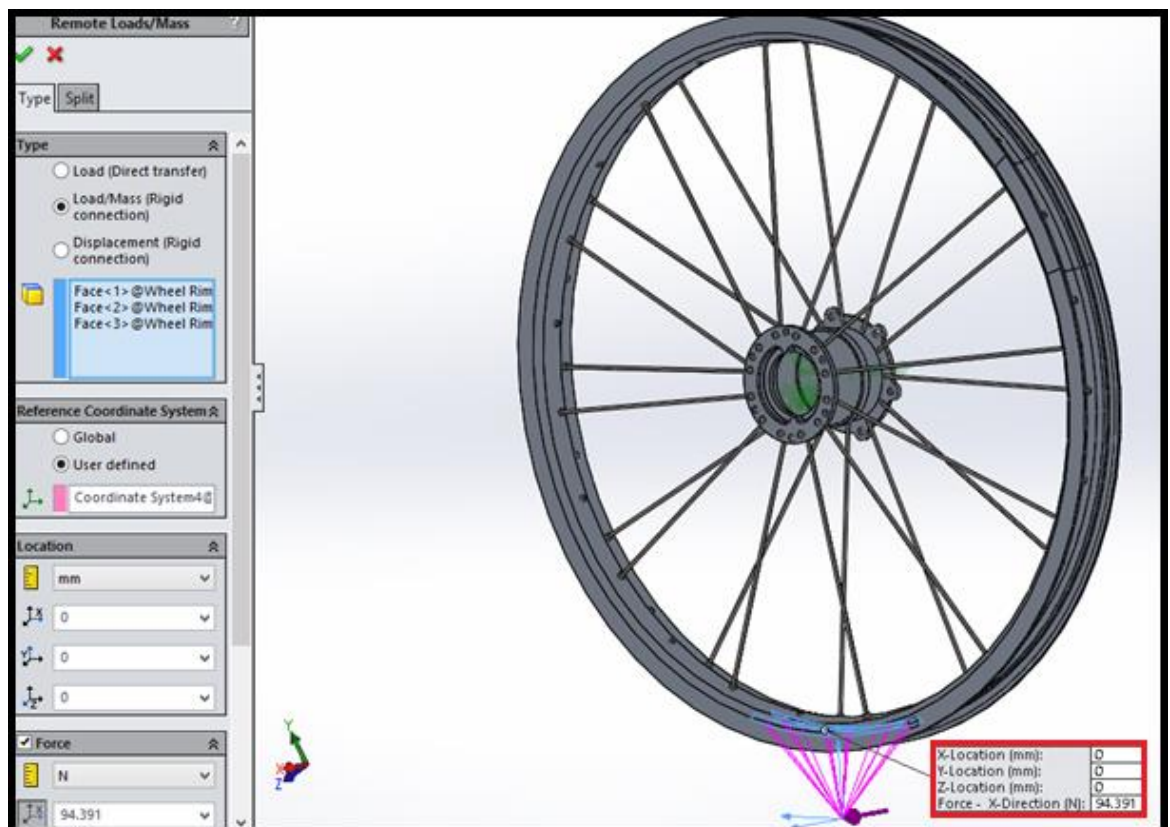
Figure 32 - Lateral load applied to wheel model (*Dassault Systèmes SolidWorks*)

The induced strains were predicted by means of linear static *FEA* according to the following lateral load magnitudes:

I.   94.39 N

II.   169.10 N

III.   253.64 N

IV.   338.19 N

V.   422.97 N

3.3.3 Application of constraints

The computational wheel model being analysed was constrained for all analyses using a "*Fixed Geometry*" constraint applied to the bore of the wheel hub as shown in *Figure 33*. This constraint was applied to all of the faces of the wheel hub bore which physically contacted the wheel bearings. The applied constraint restricted all six degrees of freedom for each node on the constrained surfaces, while closely representing the manner in which the wheel was physically constrained.
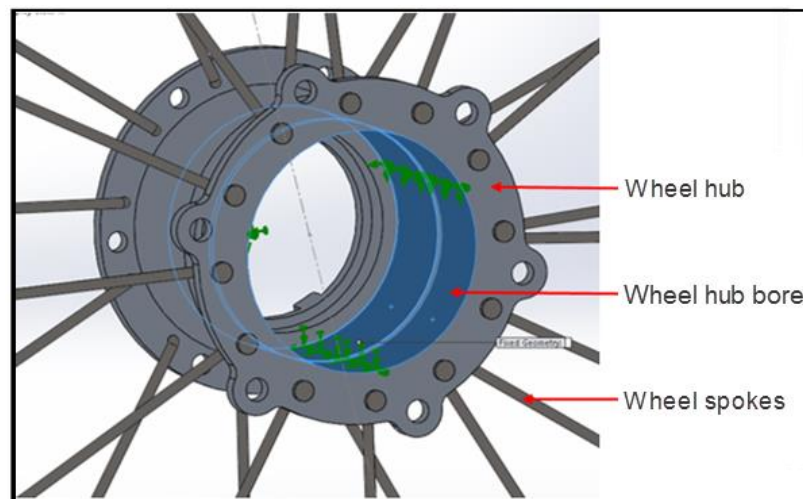
Figure 33 - Computational constraint applied to wheel hub bore during linear static *FEA* (*Dassault Systèmes SolidWorks*)

The results corresponding to this part of the research method are presented in *Chapter 4*. In the next section, the manner in which structural topology optimization software was utilized to produce an optimized wheel geometry

according to the computational loads and constraints discussed in this section is presented.

3.4 Design of wheel through structural topology optimization

This section details the manner in which structural topology optimization software was utilized to produce an efficiently designed wheel geometry, which could be manufactured and optimized as a composite component in the following stage of research. This wheel geometry was produced according to the computational input methods (representative of the combined loading mechanisms discussed in section *3.2.2.5 of Chapter 3*) established in the previous section.

3.4.1 Creation of wheel base model for structural topology optimization

The space to be optimized is represented by the domain, Ω. The potential of structural topology optimization techniques to produce efficient solutions increases when the design space, Ω, is maximized. As such, this sub-section discusses the choices made during the creation of the design space optimized in this study.

Structural topology optimization is usually always applied to existing wheel models in order to determine how a design may be improved upon through the removal material. However, this approach would have been ineffective if applied in this dissertation owing to relatively small design space volume occupied by the pre-tensioned spokes. Here, the design space was regarded as the volume occupied by the pre-tensioned spokes since, as with all wheels, both the wheel hub and tyre bead are crucial to functionality, and should therefore not be altered. Rather, it is the connection between these two entities which may be altered. As such, the design space subject to optimization was maximized through the creation of a solid disc-like connection between the wheel hub and tyre bead. The computational wheel model optimized in this chapter (shown in *Figure 34*) was defined as a solid entity combining the tyre bead and hub of the commercial wheel.
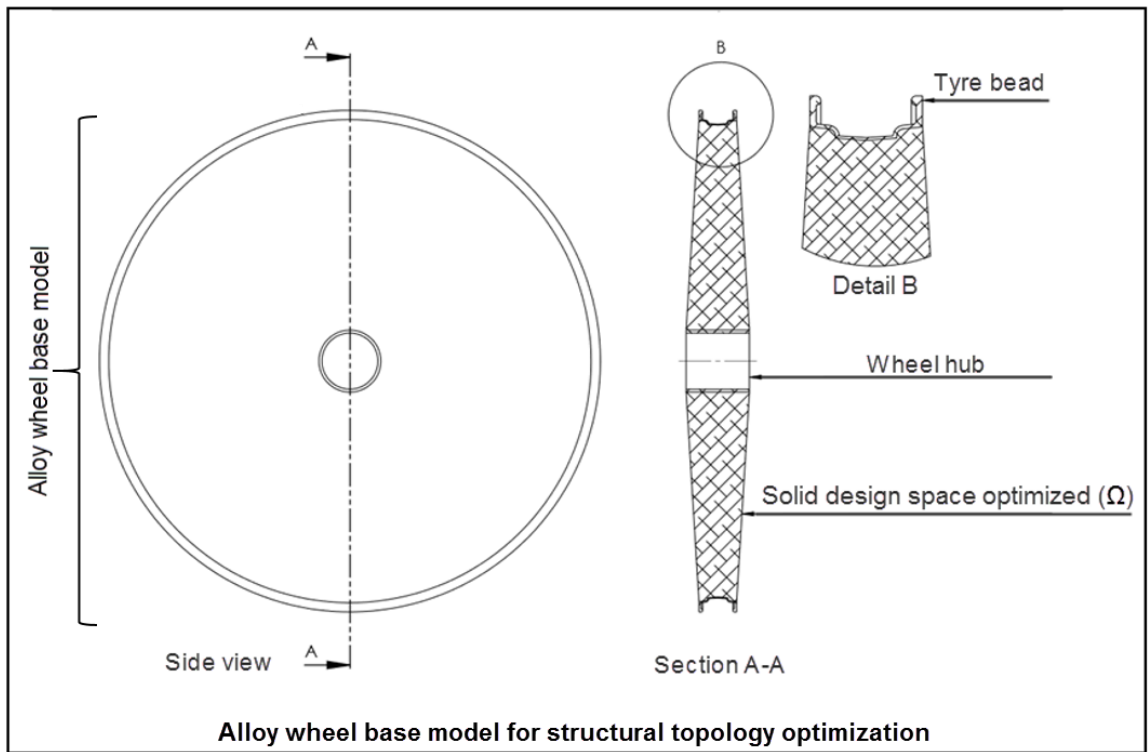
Figure 34 - Solid disc-like wheel model to be optimized

The material properties assigned to this wheel design space corresponded to a 6061-T6 aluminium alloy as shown in the *Figure 35*. These material properties were assigned to the design space being optimized in this section so that any comparison of wheel rim strain behaviour between the optimized wheel geometries produced in this section and the commercially available wheels currently utilized on the *Nelson Mandela University Eco Car* could be credited to the influence of geometry alone.

Property	Value	Units
Elastic Modulus	69000	N/mm^2
Poisson's Ratio	0.33	N/A
Shear Modulus	26000	N/mm^2
Mass Density	2700	kg/m^3
Tensile Strength	124.08	N/mm^2
Compressive Strength		N/mm^2
Yield Strength	55.15	N/mm^2
Thermal Expansion Coefficient	2.4e-005	/K
Thermal Conductivity	170	W/(m·K)
Specific Heat	1300	J/(kg·K)
Material Damping Ratio		N/A

Figure 35 - 6061 Aluminium Alloy material properties as assigned to wheel model being optimized (*Dassault Systèmes SolidWorks*)

3.4.2 Increasing the range of posed solutions

A solution produced by means of structural topology optimization is unique to the loads according to which it is formed, the nature of the objective function, and any other boundary conditions specified by the user to influence its outcome. Therefore, in order to increase the potential of this process to produce a geometric wheel solution with the lowest possible mass and greatest stiffness, these factors were applied in various combinations to produce 48 different solutions. However, before these combinations are presented, the factors themselves are discussed in the following sub-sections.

3.4.2.1 Loads and constraints

The loading mechanisms and constraints according to which the design space was optimized were applied as per the methods described in sections *3.3.2* and *3.3.3*. These mechanisms were applied as a static combined loading scenario representative of the worst case anticipated operating conditions.

3.4.2.2 Objective optimization function

The objective function to be minimized during optimization may describe either domain mass or compliance. Therefore, the structural topology optimization studies performed in this dissertation were conducted so as to minimize both of these separately. However, doing so required additional design targets to be specified in conjunction with each objective function. In the case of specifying component mass as the objective design function to be minimized, a minimum component safety factor as shown *Figure 36* was required as an additional design target. The structural topology optimizations performed in this dissertation were conducted according to the following stress-based minimum safety factors:

I.   1.2

II.   1.6

III.   2.0
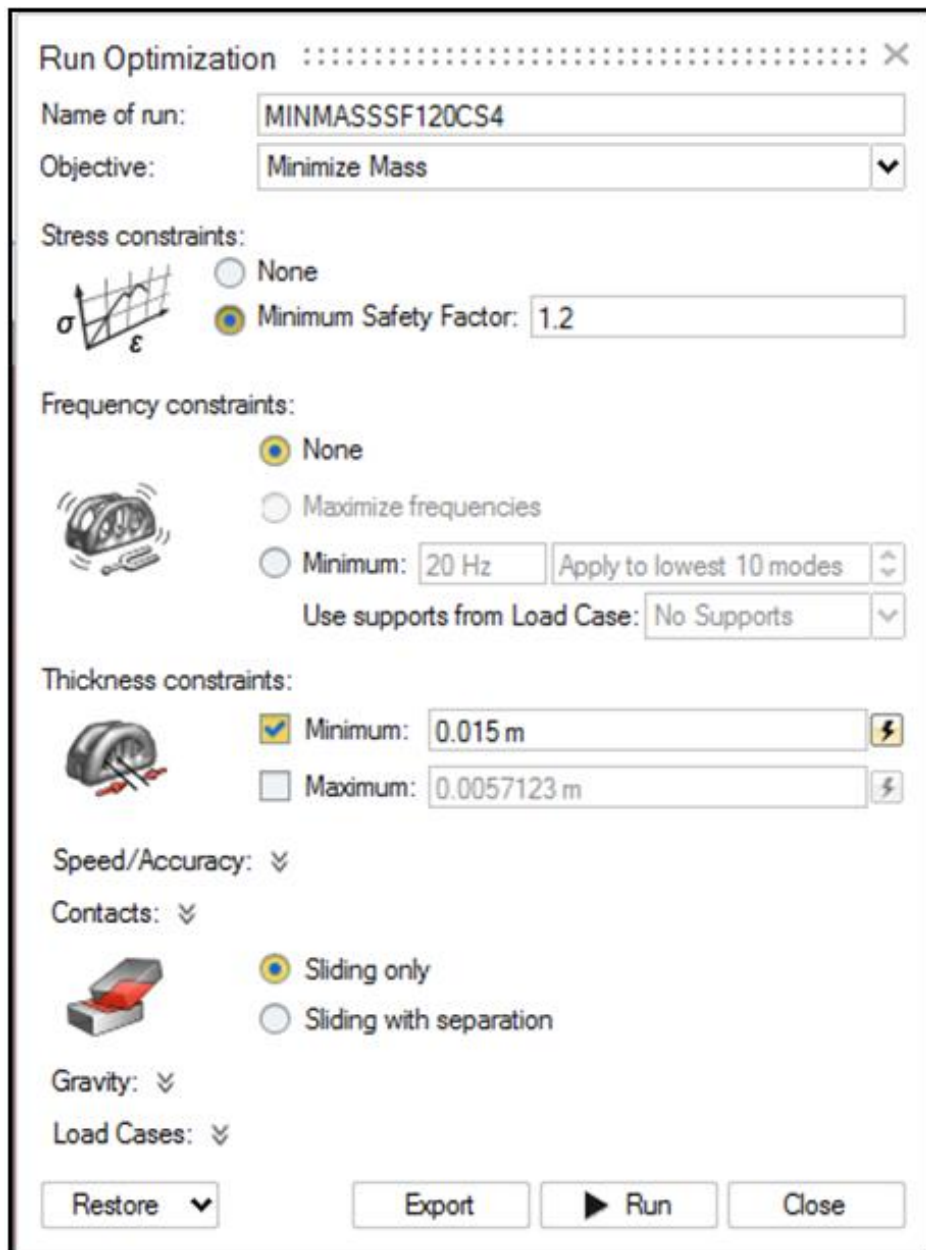
Figure 36 - Required input for minimum mass topology optimization (*solidThinking Inspire*)

Similarly, structural topology optimizations conducted for the purpose of maximizing component stiffness required the definition of a target solution design volume. The default target solution design volume selected by s*olidThinking Inspire 2016.1 5557* was set to 30 percent as shown in *Figure 37*.
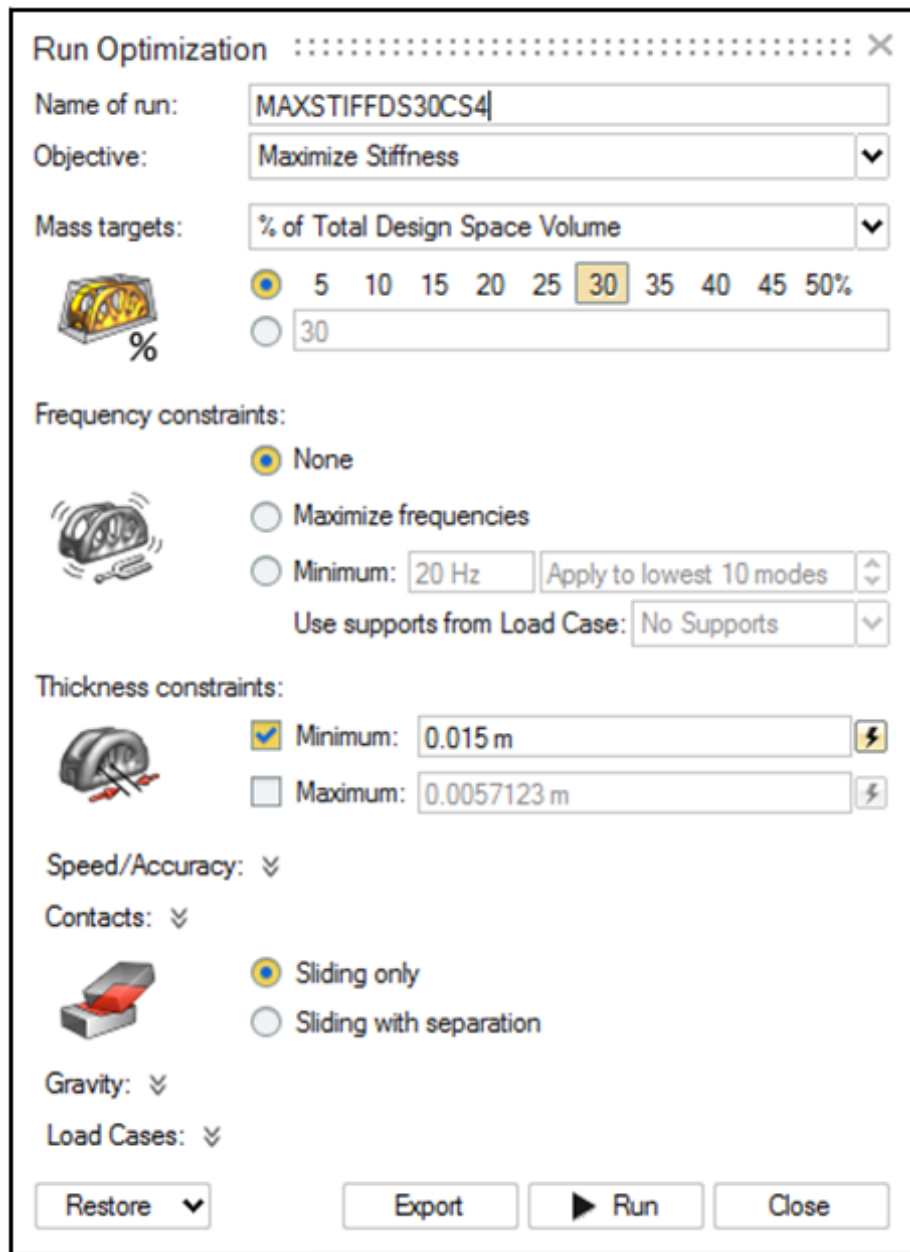
Figure 37 - Required input for maximum stiffness topology optimization (*solidThinking Inspire*)

However, this may be altered by either entering a user defined target, or by selecting one of the alternative target value buttons between 5 and 50 percent. The following target design volumes were applied to the structural topology optimizations intending to maximize component stiffness in this dissertation:

I.   5 percent

II.   25 percent

III.   50 percent

3.4.2.3 Additional boundary conditions

Modern topology optimization software packages enable structural engineers and designers to apply boundary conditions to the optimization process to ensure that solutions which are both efficient and topologically suited to a given manufacturing process are produced. In this dissertation, the applied shape controls were required to ensure that the produced solutions could be manufactured as moulded composite components capable of maintaining structural integrity during rotation. Therefore, those applied to the structural topology optimizations performed in this dissertation included a split-draw constraint to ensure solution manufacture as a moulded component, and cyclic symmetry constraints to ensure that structural integrity would be maintained during operation.

The degree of cyclic symmetry applied to the topology optimizations performed in this dissertation was not kept constant. Instead, it was varied between the following degrees of cyclic symmetry:

I.   Four

II.   Five

III.   Six

IV.   Seven

3.4.2.4 Solution range

Since the externally applied loads and constraints according to which optimization was performed remained constant, the range of geometric solutions produced by means of structural topology optimization in this dissertation was increased by controlling each of the factors discussed in sections *3.4.2.2* Objective optimization function and *3.4.2.3* Additional boundary conditions. As such, 48 different wheel designs were produced according to the possible combinations of governing factors shown in Table 7.

Table 7 - Factors influencing solutions produced by means of structural topology optimization

Governing factor	Objective optimization function	Associated design objective	Cyclic symmetry shape control	Split draw shape control
Number of Possible variations	2	3	4	2
Description	Minimize mass or maximize stiffness	Minimum component safety factor of either 1.2, 1,6, or 2.0 in the case of minimum mass study Target design volume of either 1.2, 1,6, or 2.0 in the case of maximum stiffness study	4, 5, 6, or 7 degrees of applied cyclic symmetry	"Hole allowed" or "No Hole" type split draw control

3.4.3 Selection of optimum wheel geometry

The 48 different wheel designs produced by means of structural topology optimization techniques were compared against one another on the basis of mass and stiffness. During this process, the wheel design with the lowest mass and greatest stiffness was identified as being the solution most suitable to this study. While both component mass and stiffness were key factors in identifying this solution, the potential suitability of this solution towards being manufactured as a composite component was also considered.

However, it should be noted that the solutions produced by means of structural topology optimization were not smoothly defined. Therefore, the optimized solution selected as the most suitable to this dissertation required geometric refinement so that it could be modelled, optimized, and manufactured as a composite component in the following research stage. This geometric refinement is discussed in the following sub-section.

3.4.4 Refinement of optimum wheel geometry

The refinement of the wheel geometry discussed in the previous sub-section was performed by creating an entirely new computational model consisting of well-defined geometric features. The dimensions of these geometric features were determined by measuring the dimensions of the unevenly-defined geometry (discussed in the previous subsection) at various positions. These

measurements were then utilized to create anchor points to which well-defined and smoothly-curved geometric features could be fitted.

The structural integrity of the wheel geometry produced by this method was checked by means of linear static *FEA*. Consequently, it was found that the refined wheel geometry failed when subjected to the combined loading scenarios upon which the structural topology optimizations performed in this section were based.

As such, the wheel geometry was further refined by increasing the diameter of various fillets within the design such that it did not fail. The wheel geometry produced in the second refinement was selected as the wheel geometry produced by means of structural topology optimization techniques to be modelled, optimized, and manufactured as a composite component in the following research stage.

The results corresponding to this part of the research method are presented in *Chapter 5*. In the next section, the manner in which composites optimization software was utilized to produce an optimized composite wheel design corresponding to the geometry obtained by means of this structural topology optimization is discussed.

3.5 Design of wheel through composites optimization

This section serves to detail the manner in which the wheel geometry produced by means of structural topology optimization was modelled, optimized, and manufactured as a composite component. Ultimately, the mass and strain behaviour of the composite wheel produced in this research stage was compared against the mass and strain behaviour of the commercial wheels currently utilized on the *Nelson Mandela University Eco Car*

3.5.1 Composite material properties

The stiffness properties of the unidirectional carbon fibre/epoxy laminae utilized in this study were determined by means of the invariant based method put forward by Tsai et al. in 2014.

These material properties are:

I. E_1 Elastic modulus in fibre direction

II. E_2 Elastic modulus transverse to fibre direction

III. v_{12} Poisson coefficient

IV. G_{12} Shear Modulus

As such, an *Instron 8801* was utilized to perform tensile tests on three specimens according to *ASTM D3039* to determine the elastic modulus of each specimen in the principal fibre direction. These specimens were constructed by means of hand laminating and vacuum bagging four successive uni-directional 12K HR T700 carbon tape laminae with an epoxy based AR600 (resin) and AH203 (hardener) matrix at an absolute pressure of -80 kPa. Additionally, the orientation of each of these laminae was such that the principal fibre direction was parallel to the longitudinal axis of the specimens so that the measured elastic moduli were representative of the elastic modulus in the fibre direction only.

The average elastic modulus of these three specimens was then utilized to determine the normalized trace of the stiffness matrix, and the remainder of the above listed material properties describing the unidirectional carbon fibre/epoxy laminae utilized in this dissertation. Additionally, the average ultimate tensile strength (according to last ply failure) recorded in these three tensile tests was utilized to describe the failure behaviour of the material according to the unit circle failure envelope. The material properties determined in this way are presented in *Table 8*.

Table 8 - Material properties for laminated 12K HR T700 carbon tape and AR600 & AH203 matrix

E_1	Elastic modulus in fibre direction	101.5	GPa
E_2	Elastic modulus transverse to fibre direction	5.8	GPa
v_{12}	Poisson coefficient	0.33	--
G_{12}	Shear modulus	4.0	GPa
F_{1t}	Longitudinal tensile strength	1.4	GPa
F_{1c}	Longitudinal compressive strength**	1.4	GPa

**The tabulated longitudinal compressive strength was determined analytically. The deviation between this analytically determined value and the physically recorded longitudinal tensile strength was less than 5 percent. As such, the longitudinal compressive strength utilized in this study was taken as being of equal magnitude to the longitudinal tensile strength recorded during physical testing.

3.5.2 Creation of wheel base model for composites optimization

The material properties determined in the previous section were utilized to create three computational composite wheel base models consisting of laminae stacked at respective fibre orientation intervals of 15°, 30°, and 60°. The geometry of these composite wheel base models was taken as that of the wheel geometry produced using structural topology optimization. However, each of these models was generated as an enclosed hollow surface instead of a solid body owing to the manner in which *Altair HyperWorks* utilizes free size optimization to vary the thickness of two-dimensional shell elements as discussed in section *2.5.2*. Each of these composite wheel base models was discretized into 12664 two-dimensional quadrilateral shell type elements of a second order nature as shown in *Figure 38*.
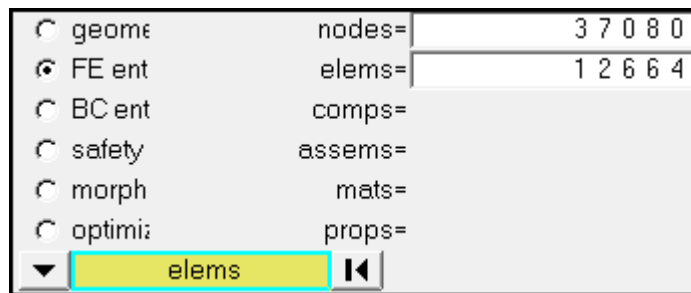
Figure 38 - Mesh Properties (Composite wheel base model, *Altair Hypermesh*)

Following on from the above model discretization, the quality of the produced finite elements was increased using the *"Quality Index"* tool built into *Altair Hypermesh*. During this process, the geometric properties of individual elements were manipulated so as to minimize any geometric inaccuracies

produced as a result of discretization. The quality of the achieved mesh representing the three computational wheel base models is shown in *Figure 39*.
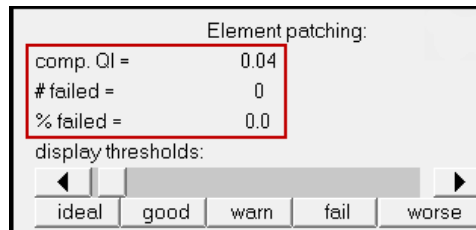
Figure 39 -Achieved mesh quality of composite wheel base model (*Quality Index* tool, *Altair Hypermesh*)

The material properties shown in *Table 8* were then applied to the elements produced in the preceding paragraph to represent these computational wheel base models as laminated composite components. As such, each of these composite wheel base models was considered as two separate entities consisting of the circumference to which the tyre is seated, and the hollow body of the wheel connecting this circumference to the wheel hub. Composite free size optimization was utilized to investigate which of these three base models could be lightened the most during the composites optimization process. In doing so, it was found that the composite base model corresponding to laminae varied at fibre orientation intervals of 30° could produce the lightest solution. The fibre orientations corresponding to this base model are shown in *Figure 40*.
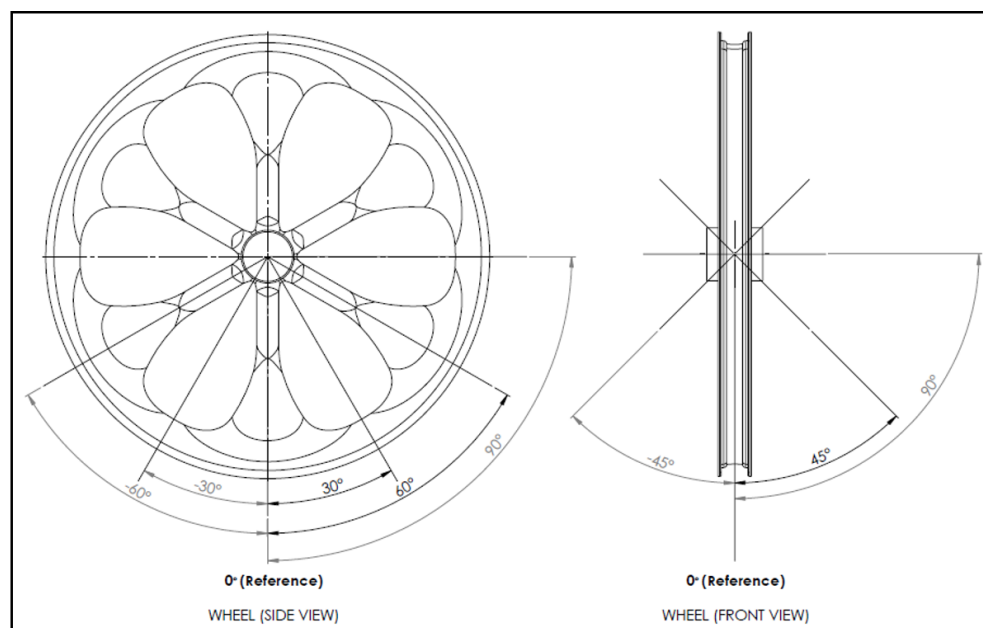
Figure 40 - Fibre orientations for composite wheel base model

Additionally, the stacking sequences of the laminates comprising wheel body and circumference of this composite wheel base model is presented in *Table 9*. In this table, the order of the stacking sequence progresses such that the first lamina forms the external surface of the component.

Table 9 - Stacking sequence of composite wheel base model

Wheel body	
Lamina	Orientation [°]
1	0
2	30
3	-30
4	60
5	-60
6	90
Wheel rim circumference	
Lamina	Orientation [°]
1	0
2	45
3	-45
4	90

Furthermore, the thickness of each of these laminae was set to 2 mm. While this is much thicker than an individual physical lamina, this practice is common in composites optimization to enhance the potential scope of the optimization process. These lamina thicknesses were varied during the composites optimization process discussed in the following sub-section. However, before these composites optimization techniques were applied, the mass and strain behaviour of the optimization base model discussed in this section was identified by means of linear static *FEA* according to the combined loading scenario presented in *Table 6*. These *FEA* loads and constraints were also applied to the composite wheel models discussed in the following sub-section.

3.5.3 Application of composites optimization

The resultant wheel design produced by means of composite free size optimization applied to the composite wheel base model corresponding to fibre orientation intervals of 30° was further optimized by means of composite sizing and shuffling optimizations. The *FEA* wheel mass and rim strain behaviour corresponding to each of these stages of composites optimization were

compared against one another to investigate the changes in component mass and stiffness resulting from this process.

As discussed in section *2.5.2*, various user defined manufacturing constraints may be applied to the composites optimization process to manipulate the produced results. However, these constraints are most commonly applied for the purpose of controlling the thickness of the produced laminate, as well as the number of consecutively permissible laminae of the same orientation. Since the composite wheel design being optimized was not governed by any standards or rules, no such constraints were applied during the optimization process. In the next sub-section, the process utilized to manufacture two wheels according to optimized result is discussed.

3.5.4 Manufacture of optimized composite wheel

The first stage in the manufacture of the resultant composite wheel consisted of the definition of lamina shapes. These shapes were defined by individually editing the element groups representative of each lamina such that they were practical to manufacture. This process involved the removal or addition of any element groups representative of geometric features within each lamina which were not practical to manufacture. Additionally, this procedure was performed such that the element groups defining the laminae between each plane of cyclic symmetry were symmetric in both shape and fibre orientation about the wheel centre. Consequently, since the finite element model produced by means of the applied composites optimization techniques had been manipulated to better represent a component which could be practically manufactured, linear static *FEA* was utilized to ensure that it did not fail when subjected to the combined loading mechanisms upon which it was formed. Failure was investigated by means of a unit circle failure envelope. After it was shown that the optimized composite wheel design containing refined laminae geometries would not fail, physical lamina templates were generated from the fore-mentioned element groupings by means of the procedure outlined in the following steps.

I. A two dimensional plane was created in *Altair Hypermesh* such that it was parallel to side of the wheel model

II.   The major dimensions of each geometric feature defining the element groups representative of each lamina were measured

III.   A two dimensional plane was created in *Dassault Systèmes SolidWorks* alongside a model of the wheel geometry such that it was identical to the previously defined plane in *Altair Hypermesh*

IV.   The previously measured dimensions of each geometric feature within a laminate were sketched on to the plane defined in the previous step

V.   A series of smoothly curved lines were fitted to the sketch according to the previously sketched lamina dimensions

VI.   The produced sketch was then projected on to the curved surfaces of the wheel model such that it represented the lamina geometry as it would exist when placed into a physical mould

VII.   The lamina projection was then flattened into a two-dimensional sketch which accounted for the curved surfaces of the wheel model and draping required for manufacture

VIII.   The previously described steps IV to VII were repeated for each of the lamina shapes required to manufacture the optimized composite wheel

Hereafter, these lamina templates were printed and utilized to hand-cut each of the uni-directional 12K HR T700 carbon tape laminae required to manufacture two composite wheels according to the optimized design. Some of these hand-cut laminae are shown in *Figure 41*. The following paragraphs describe the layup process utilized to manufacture one composite wheel.

Figure 41 – Example of some of the dry carbon fibre laminae hand-cut according to the optimized composite wheel design containing refined lamina geometries

After all of the dry laminae had been cut out according to templates, a *Mikon W64+* release agent was applied to the various parts of the wheel body and wheel rim circumference moulds as per the manufacturer's instructions. The two halves of the wheel body mould and the six precision machined aluminium split rings forming the wheel rim circumference mould are respectively shown in *Figure 42* and *Figure 43*.

Both halves of wheel body mould for six-fold cyclic symmetry

Figure 42 - Both halves of wheel body mould before layup or assembly

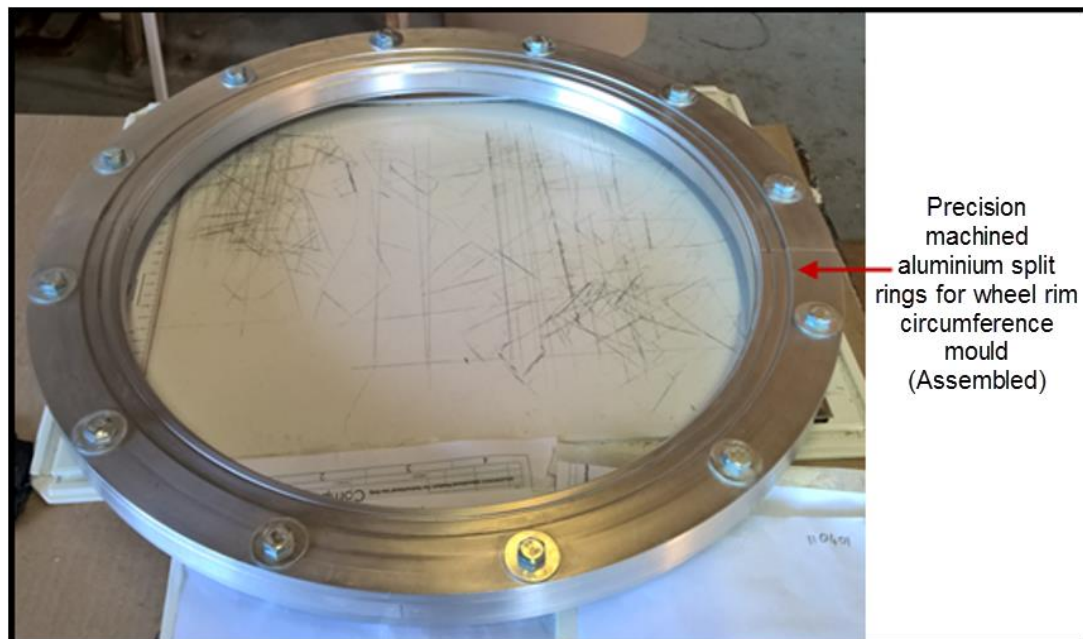Precision machined aluminium split rings for wheel rim circumference mould (Assembled)

Figure 43 - Six precision machined aluminium split rings assembled to form wheel rim circumference mould

After release agent was applied to these moulds, appropriate pieces of peel-ply, release film, and breather-bleeder were neatly cut out and stored in a dry space. An *AH203* hardener was then mixed with an epoxy based *AR600* resin

as per the manufacturer's instructions to form the matrix material. Once mixed, a clean paintbrush was utilized to apply the matrix material to the mould. The laminae were then placed in to the mould as per the positions, fibre orientations, and stacking sequence produced during the optimization process. In doing this, the same paintbrush was used to saturate each lamina with matrix material once it had been placed in the mould.

Once all of the laminae were saturated with matrix material and correctly placed into the appropriate moulds, pieces of peel-ply were laid on to the exposed side of each laminate such that they too were saturated, and no composite material was visible. The release film and breather-bleeder were then placed consecutively on top of the peel ply. Next, each mould was placed into a separate vacuum bag which had been sealed with vacuum bag sealant tape, and to which a vacuum line connected to a vacuum pump had had been fitted. These laminates were allowed to cure for three hours at an absolute (vacuum) pressure of -80 kPa as shown in *Figure 44*.
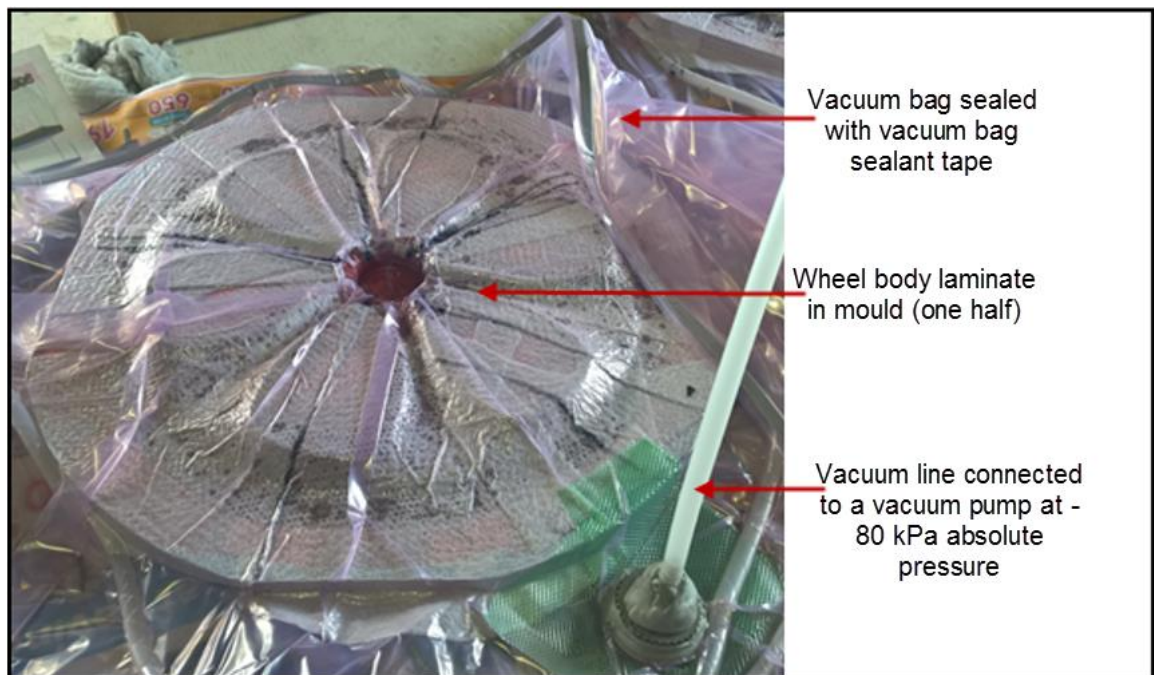
Figure 44 – One half of wheel body laminate curing in -80 kPa vacuum

After this, they were removed from the vacuum bags, and the breather-bleeder, release film, and peel-ply was removed from each laminate. The three mould components, together with their respective laminates, were then assembled to

one another as shown in *Figure 45*, and allowed to cure at ambient room temperature for a further 24 hours. During this process, the mould was assembled by means of bolted connections such that the three laminates were forced against one another for the remainder of the curing process. It was advised by local composites experts that doing this would allow the still chemically active matrix to bond the three laminates together.
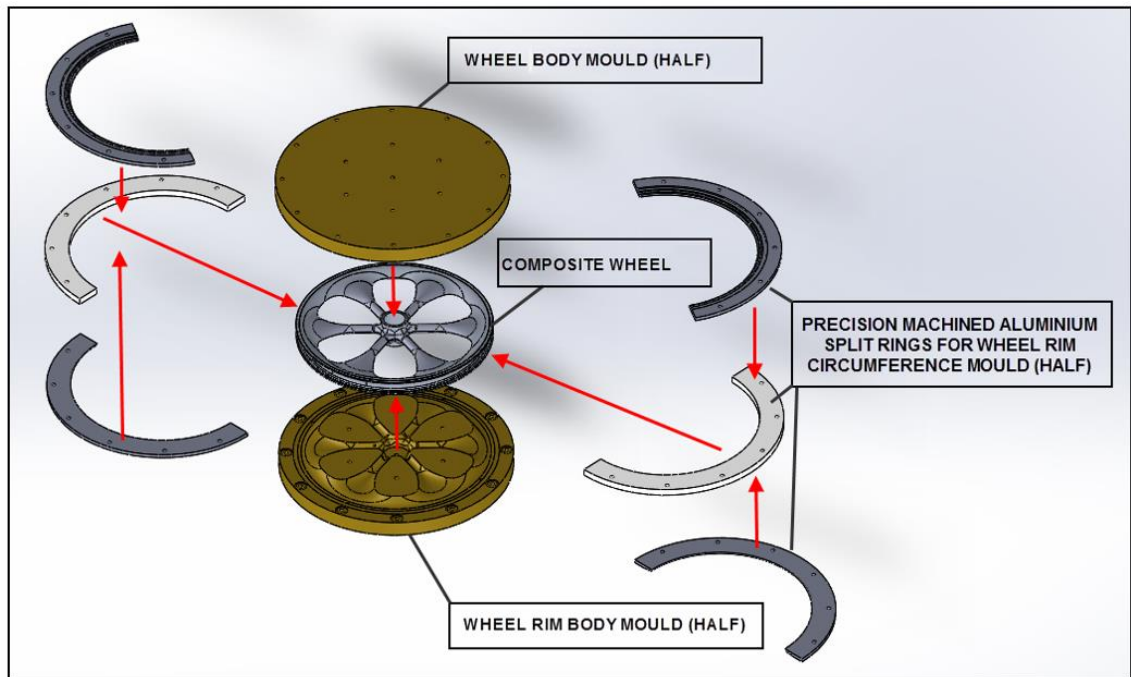
Figure 45 – Assembly of various mould components during the second stage of curing (*Dassault Systèmes SolidWorks*)

Once the laminates were fully cured, the mould was disassembled so that the composite wheel could be removed from the mould. This layup process was then repeated to manufacture the second composite wheel. These composite wheels are shown as produced in *Figure 46*.
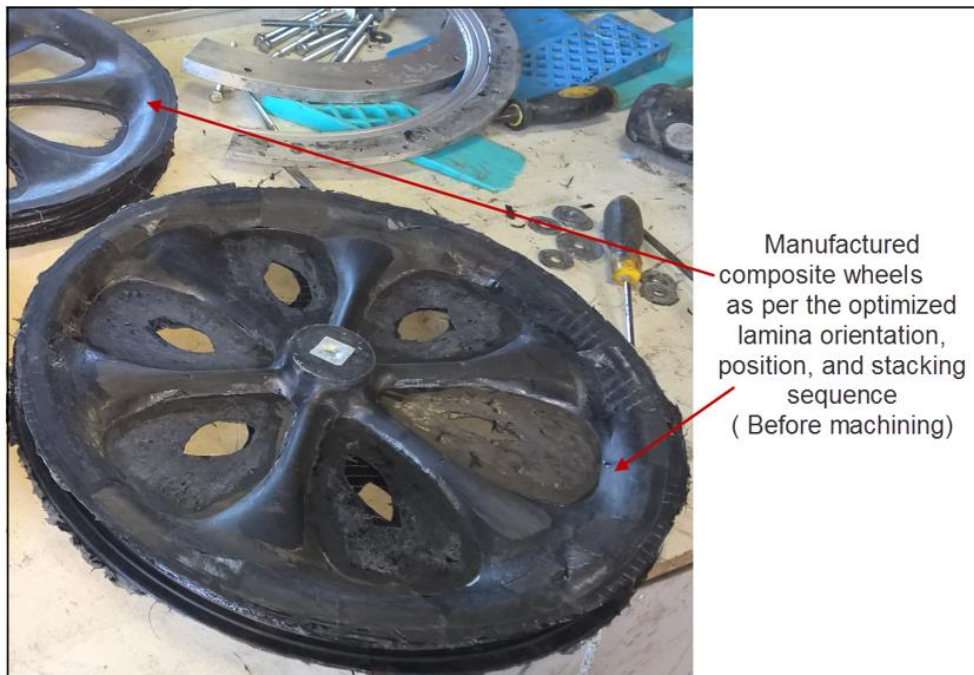
Figure 46 – Composite wheels as removed from mould (Before machining)

These wheels were then machined to remove all excess material resulting from manufacture. One of the machined composite wheels is shown in *Figure 47*.
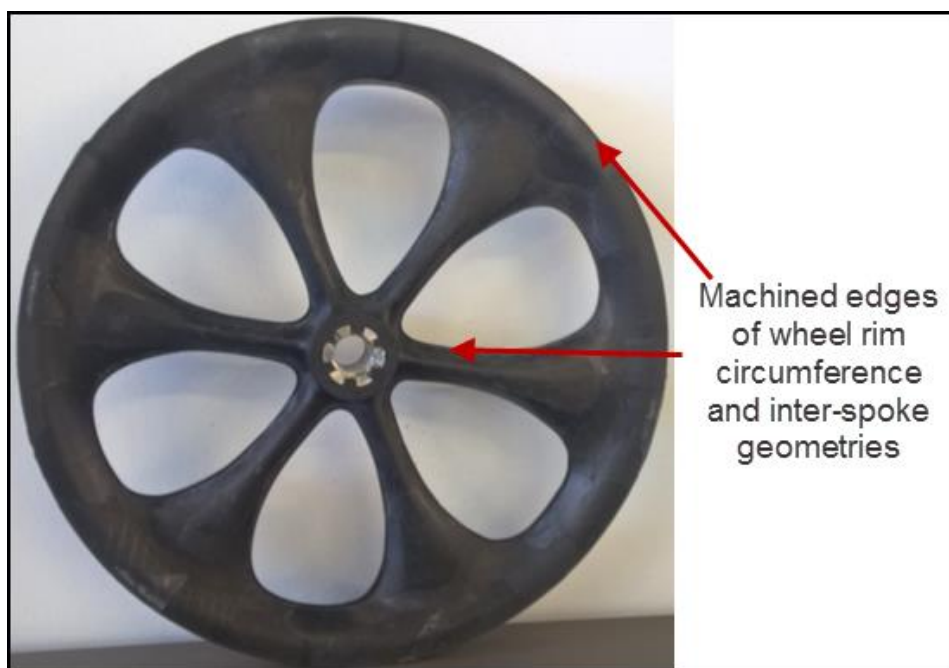
Figure 47 – One of the manufactured composite wheels after machining

The strain behaviour of both of these manufactured composite wheels corresponding to the combined loading scenario shown in *Table 6* was

measured as per the methods described in sections *3.2.1* through *3.2.3*. However, owing to the geometry of this wheel rim as determined in section *3.4*, physical strain measurements were recorded at tangential orientations of 0°, 90°, and 180° relative to the tyre-ground contact patch according to the position of *gage A* (see section *3.2.1*) only.

The measured physical strains and masses corresponding to these wheels were compared against those of the software based optimized model as well as those of the commercial wheel model. The results of this research stage are presented in *Chapter 6*.

Chapter 4: Strain behaviour of commercial wheel rim

4.1 Introduction

In this chapter, measured physical strains induced in a commercial metal wheel rim are compared against corresponding *FEA* strains to establish a benchmark against which the mass and strain behaviour of all other wheel designs produced in this dissertation may be compared. These results also serve to identify the degree of accuracy with which the applied computational *FEA* loads and constraints represent reality, as well as the validity of the methods used to physically apply each loading mechanism.

The fore-mentioned loading mechanisms include pressure, radial, lateral, and combined loads. Each physical strain value presented in the following three sub-sections is the average of thirty recorded measurements induced according to the various applied load magnitudes.

4.2 Wheel rim strain behaviour induced by tyre inflation pressure

A comparison between the physically induced and *FEA* strains in the commercial wheel rim resulting from tyre inflation pressure is shown in *Table 10* and *Figure 48.* The magnitude of each error bar half-width shown in *Figure 48* is presented in *Table 10* as 2 standard deviations of the physical strain measurements for a 95 percent confidence.

Table 10 – Measured physical and *FEA* strains induced in commercial wheel rim by pressure

Pressure [kPa]	Strain gage	Measured physical strain [μm/m]	Standard deviation of physical strain measurements [μm/m]	Error bar half-width [μm/m]	*FEA* strain [μm/m]	Difference between physically measured and *FEA* strains [μm/m]	Percentage difference between physically measured and *FEA* strains*
180	A	-57.60	1.43	2.86	-57.03	0.57	1.00
	B	-17.23	1.55	3.10	-18.70	1.47	7.86
200	A	-75.71	2.12	4.24	-71.75	3.96	5.52
	B	-23.66	2.49	4.98	-26.17	2.51	9.59
250	A	-137.83	3.23	6.46	-131.24	6.59	5.02
	B	-39.10	1.88	3.76	-39.86	0.76	1.91

*Percentage difference between physically measured and *FEA* strains determined relative to *FEA* strain
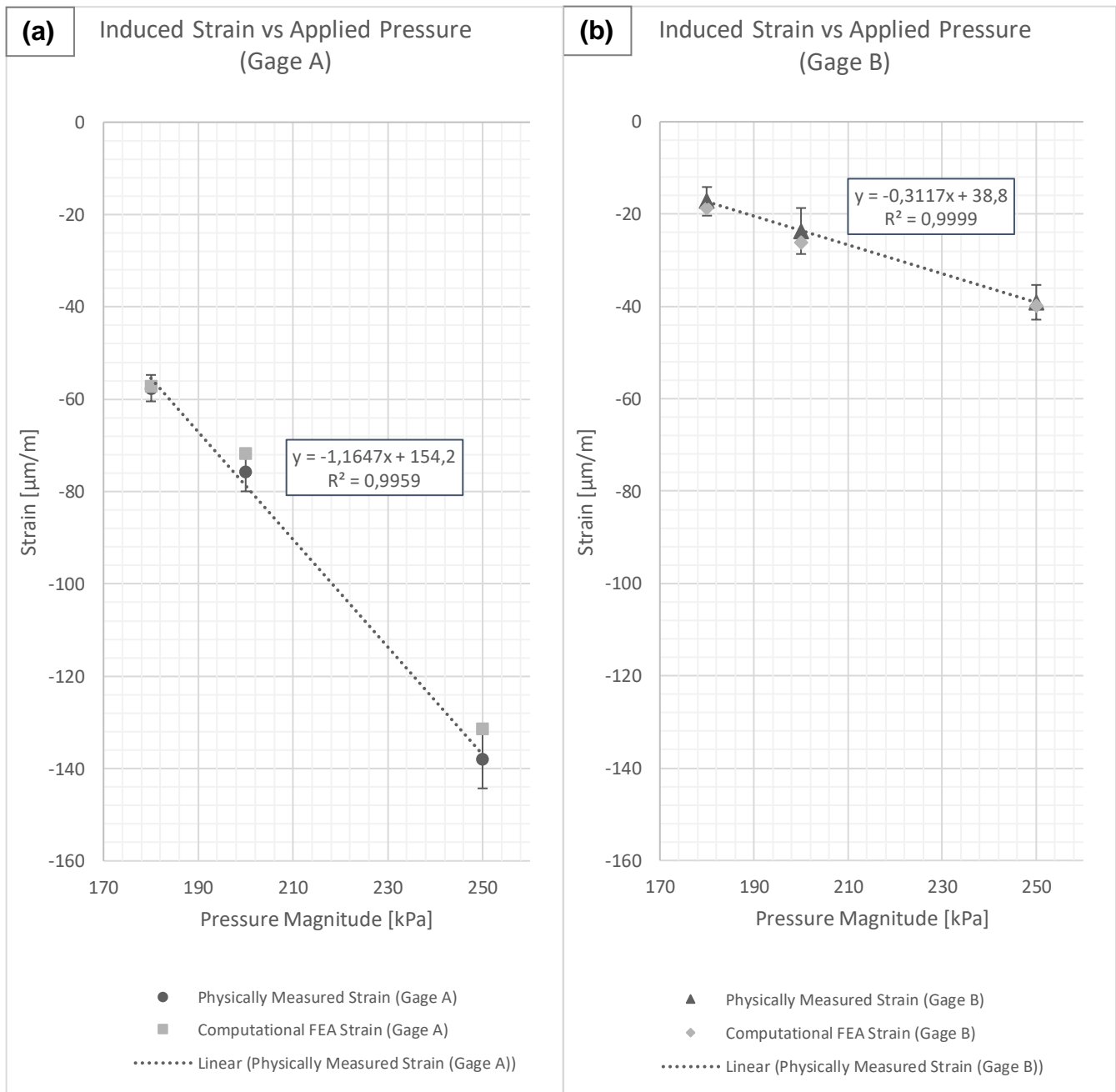
Figure 48 (a) - Measured physical strain against applied pressure as recorded by *strain gage A*

(b) - Measured physical strain against applied pressure as recorded by *strain gage B*

Although previous researchers have indicated that it is debatable whether or not it is necessary to include pressure loading in the computational *FEA* of wheels, the strain values presented in *Table 10* and *Figure 48* put forward that pressure does play a significant role in the strain variation of this model and does need to be included.

These results show an inversely proportional relationship between the magnitudes of applied pressure and strain induced in the wheel rim for both gages A and B. Figure 48 indicates that for a total increase in pressure of 70 kPa, the physically induced strain for gages A and B respectively decreased by 80.23 μm/m and 21.87 μm/m. This corresponds to an increase in compressive strain of approximately 2.4 and 2.3 times the original strain magnitude (gage A = -57.60 μm/m and gage B = -17.23 μm/m) in the pressure range from 180 kPa to 250 kPa.

Additionally, inspection of the gradients defining the applied linear regressions shown in Figure 48 suggests that an increase in applied pressure of 1 kPa decreased the induced strains at gage A and gage B by 1.165 μm/m and 0.312 μm/m respectively. These rates of change may be utilized to quantify the influence of possible inaccurately read pressure magnitudes during physical testing. Using an analogue pressure gage of 10 kPa demarcation can result in an incorrect strain reading of up to 11.65 μm/m and 3.12 μm/m for Gages A and B respectively.

The coefficients of determination corresponding to these regressions are indicated in Figure 48 (a) and (b) as 99.59 percent and 99.99 percent for gages A and B respectively. These coefficients indicate the percentage of strain variation which may be estimated from the applied pressure by the regression model.

Such estimates are presented in Table 11 for 5 kPa intervals in the pressure range of 180 kPa to 250 kPa. They were utilized to determine the presented confidence and prediction interval half-widths corresponding to a 95 percent certainty. These intervals were utilized to describe both experiment repeatability and the accuracy of strain magnitudes estimated using the regression equations.

Table 11 – Confidence and prediction intervals for regressions modelling strain induced by pressure load

Pressure load [kPa]	Gage A			Gage B		
	Strain magnitude estimated using regression [μm/m]	95% CI half-width for regression repeatability [μm/m]	Prediction interval half-width for 95% confidence [μm/m]	Strain magnitude estimated using regression [μm/m]	95% CI half-width for regression repeatability [μm/m]	Prediction interval half-width for 95% confidence [μm/m]
180.00	-55.44	39.95	62.81	-17.31	1.51	2.37
185.00	-61.26	36.71	60.80	-18.87	1.38	2.29
190.00	-67.09	33.83	59.11	-20.43	1.28	2.23
195.00	-72.91	31.41	57.76	-21.99	1.18	2.18
200.00	-78.73	29.55	56.77	-23.55	1.11	2.14
205.00	-84.56	28.38	56.17	-25.10	1.07	2.12
210.00	-90.38	27.98	55.97	-26.66	1.05	2.11
215.00	-96.20	28.38	56.17	-28.22	1.07	2.12
220.00	-102.03	29.55	56.77	-29.78	1.11	2.14
225.00	-107.85	31.41	57.76	-31.34	1.18	2.18
230.00	-113.67	33.83	59.11	-32.90	1.28	2.23
235.00	-119.50	36.71	60.80	-34.46	1.38	2.29
240.00	-125.32	39.95	62.81	-36.02	1.51	2.37
245.00	-131.14	43.47	65.11	-37.57	1.64	2.45
250.00	-136.97	47.21	67.66	-39.13	1.78	2.55

The confidence interval half-widths presented in *Table 11* indicate that repeating the experiment should yield regression lines which do not differ from those presented in *Figure 48 (a)* and *(b)* by more than 47.21 μm/m and 1.78 μm/m respectively. This means that repeating the experiment is likely to yield strain measurements which are closest to those in this dissertation for *gage B* in the range of applied pressures.

Additionally, the prediction interval half-widths presented in *Table 11* show that strain magnitudes estimated using the regression equations in *Figure 48 (a)* and *(b)* should be within 67.66 μm/m and 2.55 μm/m of corresponding measured physical strains. These values imply that the regression equation describing *gage B* is likely to produce strain values which are closer to physically measured values than those estimated according to the equation describing *gage A*.

In comparison to the measured physical strains, the *FEA* strains showed similar compressive strain variation of 2.3 and 2.1 times respectively for *gages A* and *B* within the pressure range of 180 kPa to 250 kPa. Although there is a difference between the computational *FEA* strain values and those measured physically,

according to the acceptability criteria of 10 percent allowable deviation between measured physical and *FEA* strains put forward by the *FAA*, these results may be deemed acceptable. All computational *FEA* strain values presented in *Table 10* were obtained without any additional software processing alterations.
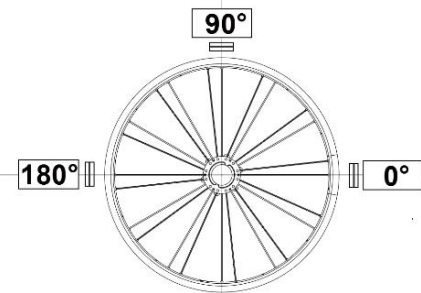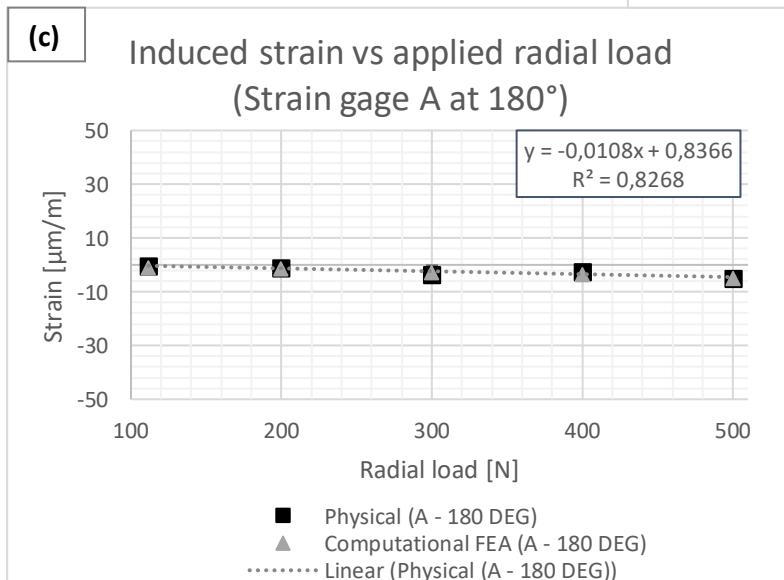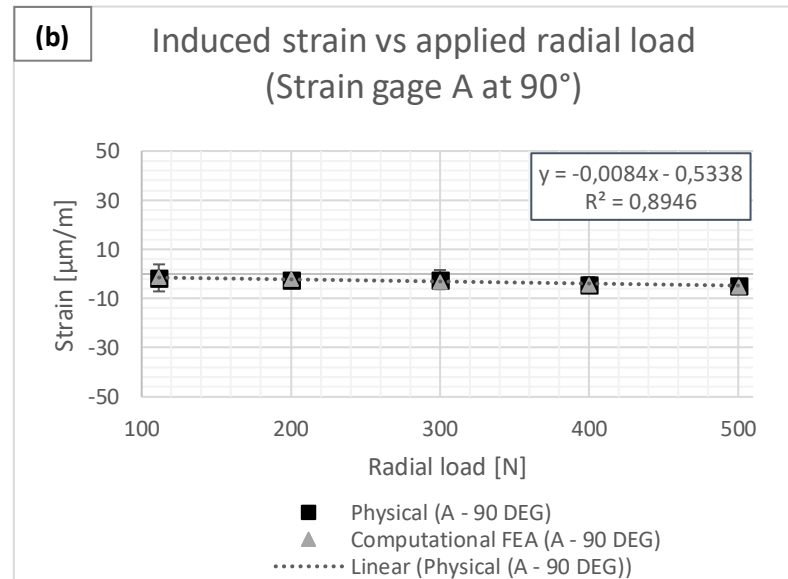
4.3 Wheel rim strain behaviour induced by applied radial loading

The physical and *FEA* wheel rim strains induced in the commercial wheel by means of applied radial load are compared against one another in *Table 12*, *Figure 49,* and *Figure 50.* Each error bar half-width presented in *Table 12* corresponds to a 95 percent confidence interval.

Table 12 – Measured physical and computational *FEA* strains induced in the commercial wheel rim by radial loading at tangential orientations of 0°, 90°, and 180°

Radial load [N]	Gage	Physically measured strain [μm/m]	Standard deviation of physical strain measurements [μm/m]	Error bar half-width [μm/m]	Computational *FEA* strain [μm/m]	Difference between physically measured and *FEA* strains [μm/m]	Percentage difference between physically measured and *FEA* strain*
Radial loading 0 degrees							
111.643	A	-12.07	1.28	2.56	-12.4	0.33	2.66
	B	12.53	1.17	2.34	12.29	0.24	1.95
200.000	A	-17.10	1.32	2.64	-17.54	0.44	2.51
	B	15.30	5.76	11.52	15.29	0.01	0.07
300.000	A	-26.80	1.44	2.88	-26.86	0.06	0.22
	B	29.70	1.58	3.16	29.56	0.14	0.47
400.000	A	-32.73	2.55	5.10	-32.55	0.18	0.55
	B	42.30	1.02	2.04	42.36	0.06	0.14
500.270	A	-43.77	1.59	3.18	-43.75	0.02	0.05
	B	43.37	1.24	2.48	43.49	0.12	0.28
Radial loading 90 degrees							
111.643	A	-1.60	2.80	5.60	-1.43	0.17	11.89
	B	-1.43	0.50	1.00	-1.92	0.49	25.52
200.000	A	-2.40	0.72	1.44	-2.20	0.2	9.09
	B	-2.30	0.47	0.94	-2.38	0.08	3.36
300.000	A	-2.31	3.18	6.36	-3.29	0.98	29.79
	B	-2.67	0.61	1.22	-6.14	3.47	56.51
400.000	A	-4.33	1.58	3.16	-4.38	0.05	1.14
	B	-3.33	0.71	1.42	-7.07	3.74	52.90
500.270	A	-4.73	0.83	1.66	-5.14	0.41	7.98
	B	-4.60	0.62	1.24	-5.76	1.16	20.14
Radial loading 180 degrees							
111.643	A	-0.40	1.19	2.38	-0.89	0.49	55.06
	B	-1.13	0.86	1.72	-2.24	1.11	49.55
200.000	A	-0.87	0.82	1.64	-1.50	0.63	42.00
	B	-3.60	0.77	1.54	-4.02	0.42	10.45
300.000	A	-3.47	1.63	3.26	-2.96	0.51	17.23
	B	-1.97	0.93	1.86	-4.46	2.49	55.83
400.000	A	-2.53	0.78	1.56	-3.71	0.35	31.81
	B	-7.17	0.91	1.82	-8.37	1.20	14.34
500.270	A	-4.83	0.99	1.98	-5.01	0.18	3.59
	B	-10.13	0.68	1.36	-10.89	0.76	6.98

*Percentage difference between physically measured and FEA strains determined relative to computational *FEA* strain

(b) Induced strain vs applied radial load (Strain gage A at 90°)

y = -0,0084x - 0,5338
R² = 0,8946

Strain [μm/m]
Radial load [N]

■ Physical (A - 90 DEG)
▲ Computational FEA (A - 90 DEG)
········ Linear (Physical (A - 90 DEG))

(c) Induced strain vs applied radial load (Strain gage A at 180°)

y = -0,0108x + 0,8366
R² = 0,8268

Strain [μm/m]
Radial load [N]

■ Physical (A - 180 DEG)
▲ Computational FEA (A - 180 DEG)
········ Linear (Physical (A - 180 DEG))

(a) Induced strain vs applied radial load (Strain gage A at 0°)

y = -0,081x - 2,0025
R² = 0,9892

Strain [μm/m]
Radial load [N]

■ Physical (A - 0 DEG)
▲ Computational FEA (A - 0 DEG)
········ Linear (Physical (A - 0 DEG))
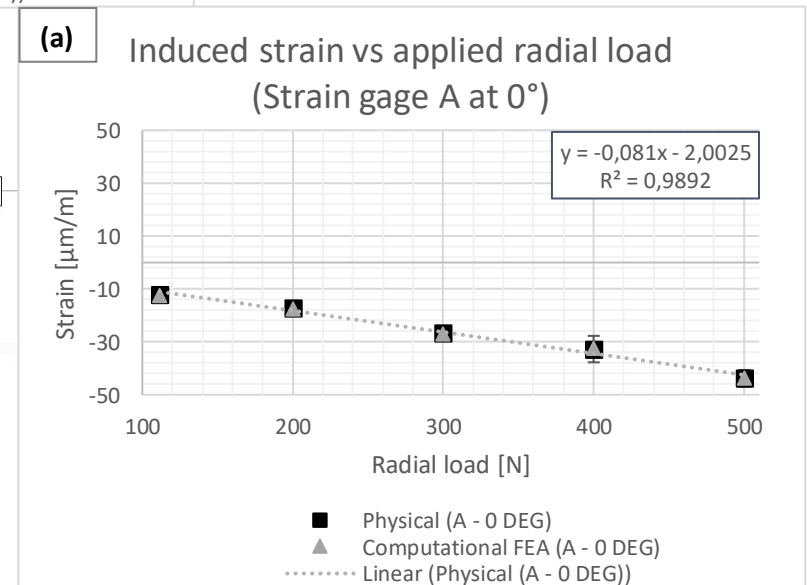
90°
180°
0°

102

Figure 49 (a) - Measured strain against applied radial load (strain gage A; tangential orientation 0°; commercial wheel rim)
(b) - Measured strain against applied radial load (strain gage A; tangential orientation 90°; commercial wheel rim)
(c) - Measured strain against applied radial load (strain gage A; tangential orientation 180°; commercial wheel rim)

Induced strain vs applied radial load (Strain gage B at 90°)

Strain [μm/m] vs Radial load [N]

y = -0,0074x - 0,6324
R² = 0,955

- Physical (B - 90 DEG)
- Computational FEA (B - 90 DEG)
- Linear (Physical (B - 90 DEG))

(c) Induced strain vs applied radial load (Strain gage B at 180°)

Strain [μm/m] vs Radial load [N]

y = -0,0221x + 1,8949
R² = 0,8226

- Physical (B - 180 DEG)
- Computational FEA (B - 180 DEG)
- Linear (Physical (B - 180 DEG))

(a) Induced strain vs applied radial load (Strain gage B at 0°)

Strain [μm/m] vs Radial load [N]

y = 0,0909x + 1,1592
R² = 0,9371

- Physical (B - 0 DEG)
- Computational FEA (B - 0 DEG)
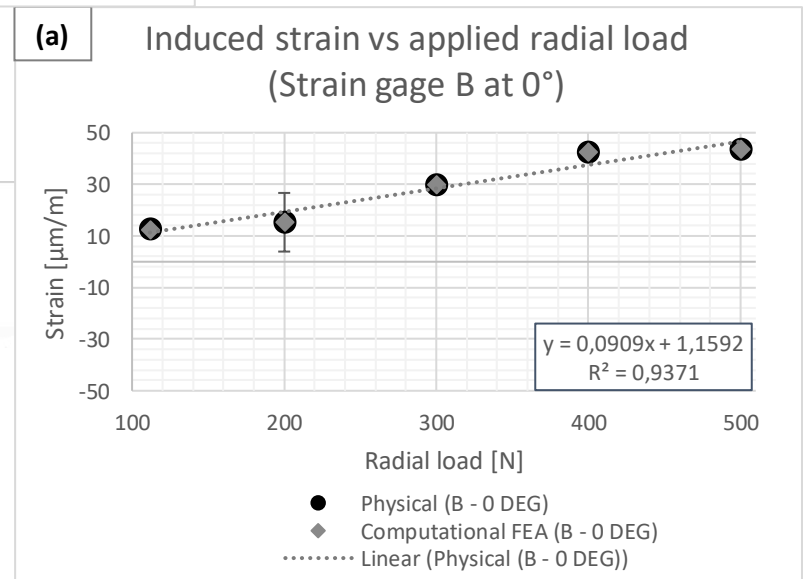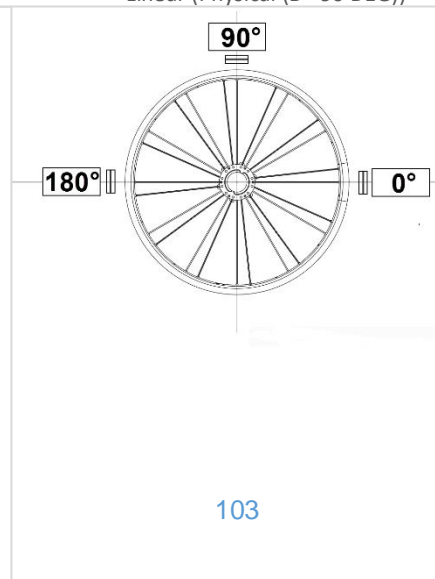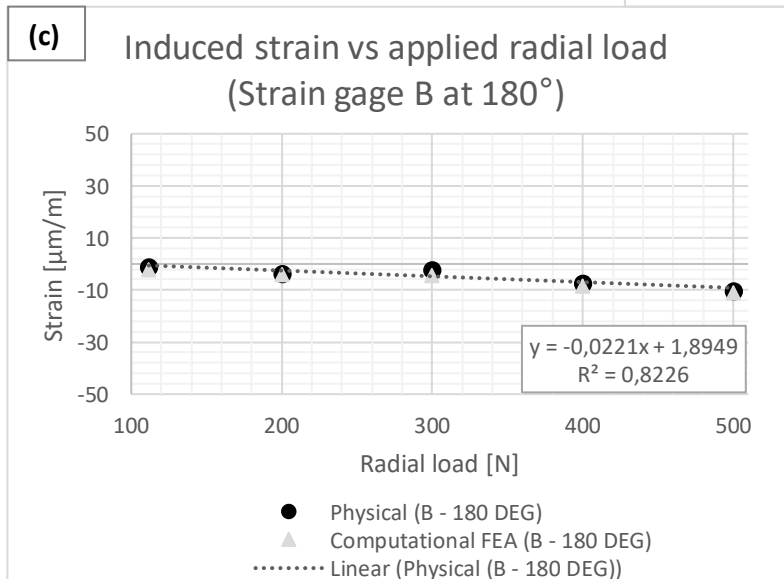- Linear (Physical (B - 0 DEG))

90° / 180° / 0°

103

Figure 50 (a) - Measured strain against applied radial load (strain gage B; tangential orientation 0°; commercial wheel rim)
(b) - Measured strain against applied radial load (strain gage B; tangential orientation 90°; commercial wheel rim)
(c) - Measured strain against applied radial load (strain gage B; tangential orientation 180°; commercial wheel rim)
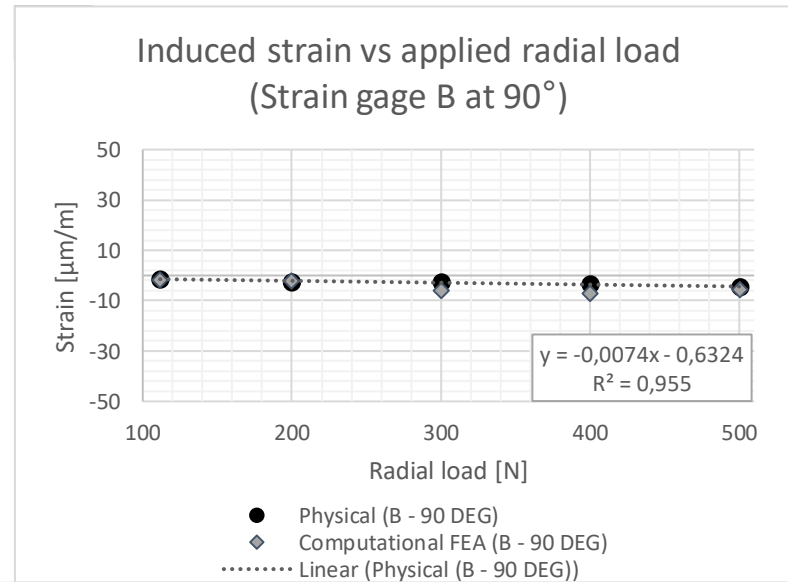
The results presented in *Table 12* and *Figure 49* show a directly proportional relationship between the magnitudes of applied radial load and compressive strain induced in the wheel rim for *gage A*. *Figure 49 (a)* illustrates that the physically induced strain for *gage A* at 0° decreased by 31.70 µm/m as the magnitude of applied radial load increased by 389 N.

Additionally, *Figure 49 (b)* and *(c)* show that for *gage A* at 90° and 180°, the same increase in applied radial load respectively decreased the measured physical strains by 3.13 µm/m and 4.43 µm/m. This indicates respective increases in compressive strain of approximately 3.6, 2.9, and 10.8 times those of the original strain magnitudes (0°= -12.07 µm/m, 90°= -1.60 µm/m, and 180°= -0.40 µm/m) in the radial loading range from 111.64 N to 500.27 N.

For *gage B* at 0°, *Table 12* and *Figure 50 (a)* indicate that the fore-mentioned increase of applied radial load resulted in the physically induced strain becoming more tensile by 30.84 µm/m. Conversely, *Figure 50 (a)* and *(b)* show that the respective magnitudes of measured physical strains for *gage B* at 90° and 180° grew more compressive by 3.17 µm/m and 9.00 µm/m. These changes correspond to respective increases in tensile and compressive strain magnitudes of approximately 3.5, 3.2, and 9.0 times those of the initial strain values (0°= 112.53 µm/m, 90°= -1.43 µm/m, and 180°= -1.13 µm/m) in the range of applied radial loads.

These results indicate that the applied radial load has the greatest influence on the induced strains for both gages at 0°. This could mean that the wheel is most likely to fail at this tangential position if the applied radial load is large enough to induce failure.

These physical strain measurements were dependent on the accuracy with which the wheel was aligned with respect to angle position in the testing apparatus. As such *Figure 51* and *Figure 52* illustrate the respective variations in physically measured strain for *gages A* and *B* at each applied radial load with respect to tangential strain gage position.
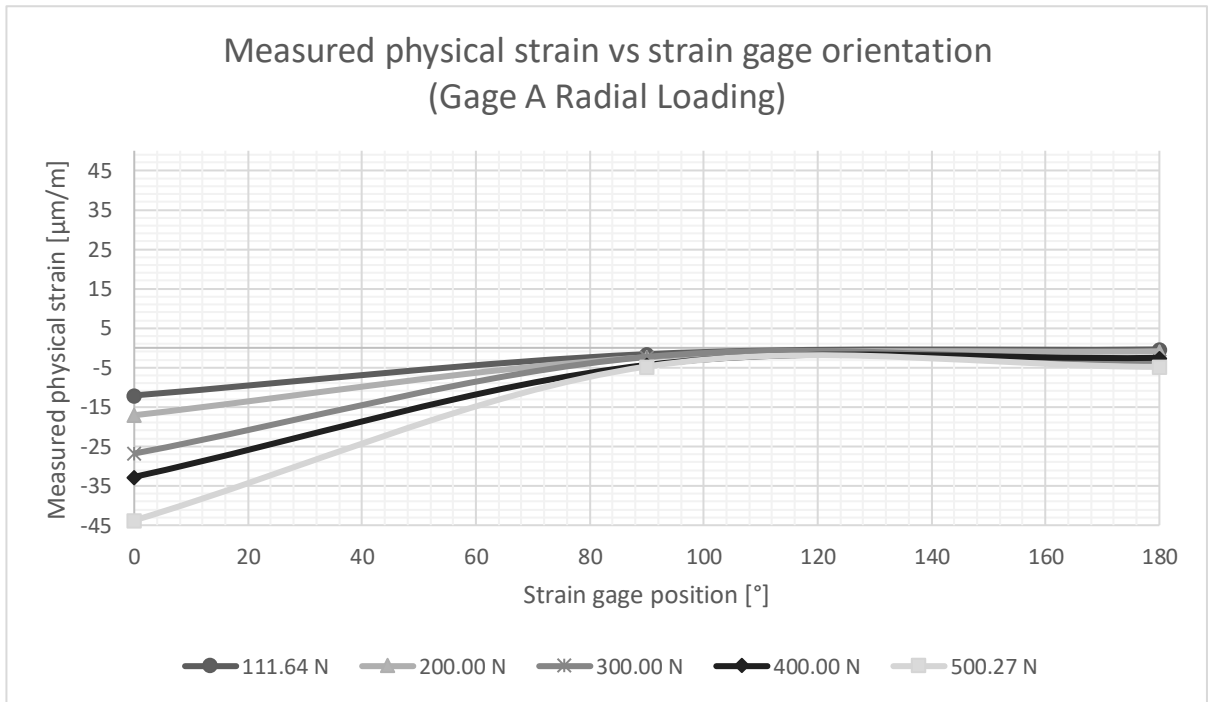
Figure 51 - Measured physical strain induced by each applied radial loading magnitude against tangential strain gage position *(gage A)*

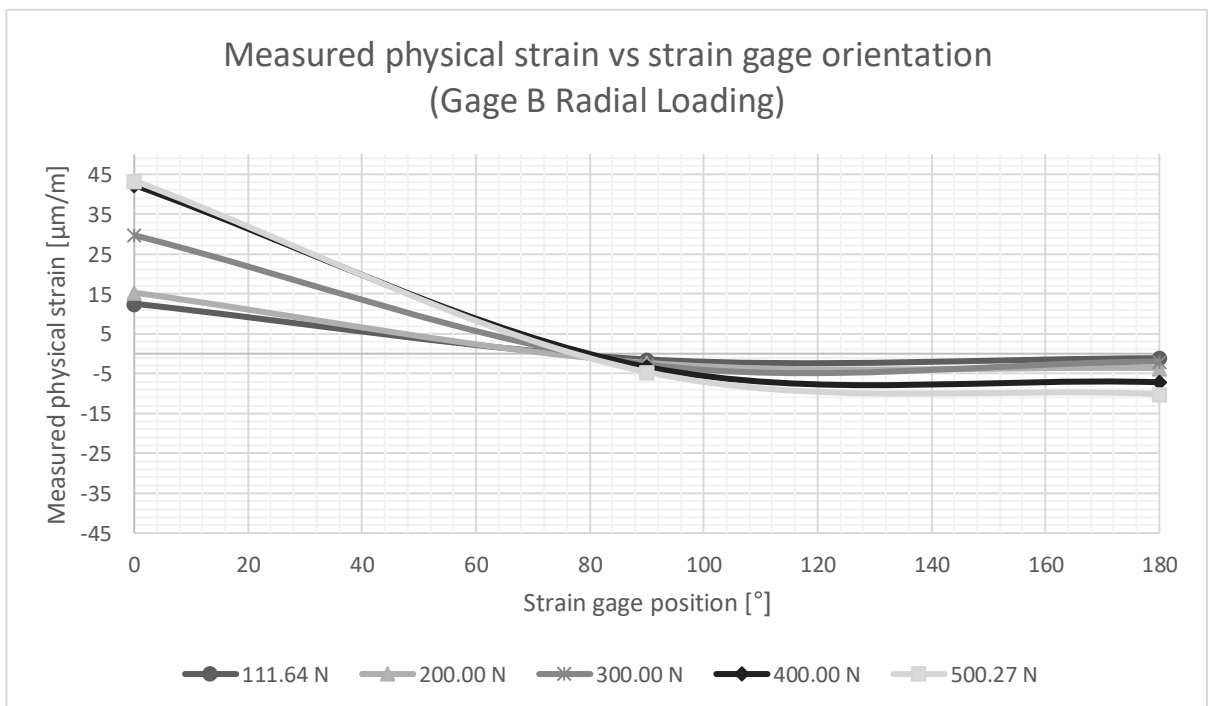**Figure 52 - Measured physical strain induced by each applied radial loading magnitude against tangential strain gage position *(gage B)***

Figure 51 indicates that for applied radial loads of 111.64 N and 500.27 N, the physical strains for *gage A* became respectively more tensile by 10.47 µm/m and 39.04 µm/m as the strain gage position moved from 0° to 90°. This

corresponds to respective decreases in compressive strain of approximately 7.5 and 9.3 times those of the original strain magnitudes of 12.07 µm/m and 43.77µm/m. Additionally, *Figure 51* shows that as the strain gage position was changed from 90° to 180°, the physically measured strains became respectively more compressive by 0.10 µm/m and - 0.73 µm/m.

For *gage B* at these applied loads, it is shown in *Figure 52* that as the strain gage position changed from 0° to 90°, the respective physically measured strains decreased by 13.96 µm/m and 53.53 µm/m. Hereafter, they are shown to have become respectively more compressive by 0.3 µm/m and 5.53 µm/m as the position of the strain gage was rotated from 90° to 180° relative to the applied loading.

It is suggested by these figures that the influence which the alignment of the wheel in the testing apparatus has on the physically recorded strain measurements for both gages is greatest between the 0° and 90° for all of the applied loading magnitudes. Additionally, these figures show that this influence became greater as the magnitude of applied radial load increased between 0° and 90°. It seems that each radial load produces a different gradient between 0° and 90°. These trends do not properly quantify the influence which misalignment of the wheel in the testing apparatus has on the recorded strain measurements. The variation in strain is approximately less than 1 µm/m per degree for all loads applied, and is likely to have a negligible effect on a combined loading scenario.

These strain values were also dependent on the magnitude of applied radial load. As such, the gradients defining the linear regressions in *Figure 49* and *Figure 50* were utilized to quantify the influence of any possible testing apparatus inefficiencies contributing towards inaccurately applied radial load magnitudes during physical testing.

In *Figure 49* these gradients indicate that for *gage A* at 0°, 90°, and 180°, a 1N increase in applied radial load respectively decreased the induced strains by 0.081 µm/m, 0.0084 µm/m, and 0.0108 µm/m. For *gage B*, the gradients presented in *Figure 50* show respective changes in strain of 0.0909 µm/m, -

0.0074 µm/m, and -0.0221 µm/m for each 1N increase in applied radial load. If the testing apparatus altered the magnitude of applied loading, the recorded strain measurements could be influenced by these amounts for each Newton of effective inefficiency.

The validity of these trends is dependent on the percentage of variation in strain which may be attributed to the applied radial load in the regression models. These percentages are indicated by the respective coefficients of determination as 98.92, 89.46, and 82.68 percent for *gage A*, and as 93.71, 95.50, and 82.86 percent for *gage B* at 0°, 90°, and 180°.

Furthermore, the accuracy of any strain estimates made using these regression equations, as well as the repeatability of the experiment, may be quantified by the prediction and regression intervals presented in *Table 13* for a 95 percent confidence.

Table 13 - Confidence and prediction intervals for regressions modelling strains induced by radial loading

Tangential strain gage position [°]	Radial load [N]	Gage A			Gage B		
		Strain magnitude estimated using regression [µm/m]	95% CI half-width for regression repeatability [µm/m]	Prediction interval half-width for 95% confidence [µm/m]	Strain magnitude estimated using regression [µm/m]	95% CI half-width for regression repeatability [µm/m]	Prediction interval half-width for 95% confidence [µm/m]
0	100.00	-10.10	3.82	6.14	10.25	10.60	17.06
	150.00	-14.15	3.20	5.78	14.79	8.90	16.06
	200.00	-18.20	2.68	5.51	19.34	7.44	15.30
	250.00	-22.25	2.30	5.33	23.88	6.39	14.82
	300.00	-26.30	2.15	5.27	28.42	5.98	14.64
	350.00	-30.35	2.28	5.32	32.97	6.32	14.79
	400.00	-34.40	2.63	5.49	37.51	7.32	15.24
	450.00	-38.45	3.15	5.75	42.06	8.75	15.97
	500.00	-42.50	3.75	6.10	46.60	10.43	16.95
90	100.00	-1.37	1.30	2.17	-1.38	0.73	1.17
	150.00	-1.79	1.09	2.06	-1.75	0.61	1.10
	200.00	-2.21	0.91	1.87	-2.12	0.51	1.05
	250.00	-2.63	0.78	1.82	-2.49	0.44	1.02
	300.00	-3.05	0.73	1.79	-2.87	0.41	1.01
	350.00	-3.47	0.77	1.81	-3.24	0.43	1.01
	400.00	-3.89	0.90	1.87	-3.61	0.50	1.05
	450.00	-4.32	1.07	1.96	-3.98	0.60	1.10
	500.00	-4.74	1.28	2.08	-4.36	0.72	1.16
180	100.00	-0.24	2.22	3.57	-0.32	4.63	7.45
	150.00	-0.78	1.86	3.36	-1.43	3.89	7.01
	200.00	-1.32	1.56	3.20	-2.53	3.25	6.68
	250.00	-1.86	1.34	3.10	-3.64	2.79	6.47
	300.00	-2.39	1.25	3.06	-4.75	2.61	6.40
	350.00	-2.93	1.32	3.09	-5.85	2.76	6.46
	400.00	-3.47	1.53	3.19	-6.96	3.20	6.66
	450.00	-4.01	1.83	3.34	-8.07	3.82	6.98
	500.00	-4.55	2.18	3.55	-9.18	4.56	7.41

The regression interval half-widths presented in *Table 13* indicate the maximum amount by which each point on the regression line may vary if the experiment is repeated. They indicate that for applied radial loads of 100 N and 500 N, the estimated strains on the regression lines corresponding to *gage A* at 0° should not vary by more than 3.82 µm/m and 3.75 µm/m. Additionally, these respective variations should be no more than 1.3 µm/m and 1.8 µm/m at 90°, and 2.22 µm/m and 2.18 µm/m at 180°. *Table 13* also indicates that for *gage B*, repeating the experiment should produce respective regression lines which do not vary from those presented in *Figure 50* by more than 10.60 µm/m at 0°, 0.73 µm/m at 90°, and 4.63 µm/m at 180° in the radial loading range from 100N to 500N.

The amount by which any strain estimate determined using these regression equations could vary from those measured physically in the applied loading range is indicated by the prediction interval half-widths shown in *Table 13*. These half-widths indicate that for *gage A* at 0°, 90°, and 180°, these differences should be no more than 6.14 µm/m, 2.17 µm/m, and 3.57 µm/m respectively. For *gage B* at these respective orientations, the maximum corresponding differences are shown to be 17.06 µm/m, 1.17 µm/m, and 7.45 µm/m.

In comparison to the physically measured strain magnitudes for *gages A* and *B* at 0°, the computational *FEA* strains show respective variations in compressive and tensile strain of approximately 3.5 times within the range of applied radial loads. These variations both differ to those shown by the physical strain measurements by approximately 0.1 times. Additionally, *Table 12* indicates that for both gages at 0°, the greatest percentage difference between the computational *FEA* strains and those measured physically is 2.66 percent. These differences may be deemed acceptable according to the acceptability criteria of less than 10 percent deviation in strain put forward by the *FAA*.

For a tangential position of 90°, *Table 12* indicates that an increase in applied radial load of 388.63 N resulted in the respective *FEA* strains corresponding to each of these gages becoming more compressive by approximately 4.0 and 3.0 times. These respectively differ from the corresponding physical strain variations by 0.58 µm/m and 0.67 µm/m for the range of applied radial loads.

Table 12 indicates that the greatest percentage difference between the measured physical and *FEA* strains at this orientation is 56.51 percent. This corresponds to a difference in strain of 3.47 µm/m for *gage B* at an applied radial load of 300 N. According to the *FAA* acceptability criteria, this percentage difference is 46.51 percent greater than the maximum permissible 10 percent.

Additionally, this acceptability range is exceeded by 1.89 and 19.79 percent for *gage A* at the applied radial loads of 111.64 N and 300.00 N, and by 15.52, 42.90, and 10.14 percent for *gage B* at 111.64 N, 400.00 N, and 500.27 N.

Lastly, the computational *FEA* strains for both gages at 180° show respective increases in compressive strain of 4.12 µm/m and 8.65 µm/m over the range of applied radial loads. These variations differ from those of the corresponding physical strains (*gage A* = 4.43 µm/m and *gage B* = 9 µm/m) by 0.31 µm/m and 0.35 µm/m respectively.

It is shown in *Table 12* that at this position, the greatest percentage difference between physically measured and *FEA* strains is 55.83 percent (2.49 µm/m) corresponding to *gage B* at 300 N. This percentage difference exceeds the *FAA* acceptability criteria by 45.83 percent. Further differences failing to meet this criteria are indicated for *gage A* at the four applied load magnitudes between 111.64 N and 400 N, and for *gage B* at 111.64 N, 200 N, and 400 N. These differences respectively exceed the *FAA* criteria by 45.06, 32.00, 7.23, and 21.81 percent for *gage A*, and by 39.55, 0.45, and 4.34 percent for *gage B*.

Although some of the presented strain measurements exceed the allowable difference presented by the *FAA*, their magnitudes are small when compared to strain values induced by pressure load. These differences were insignificant in a combined loading scenario.
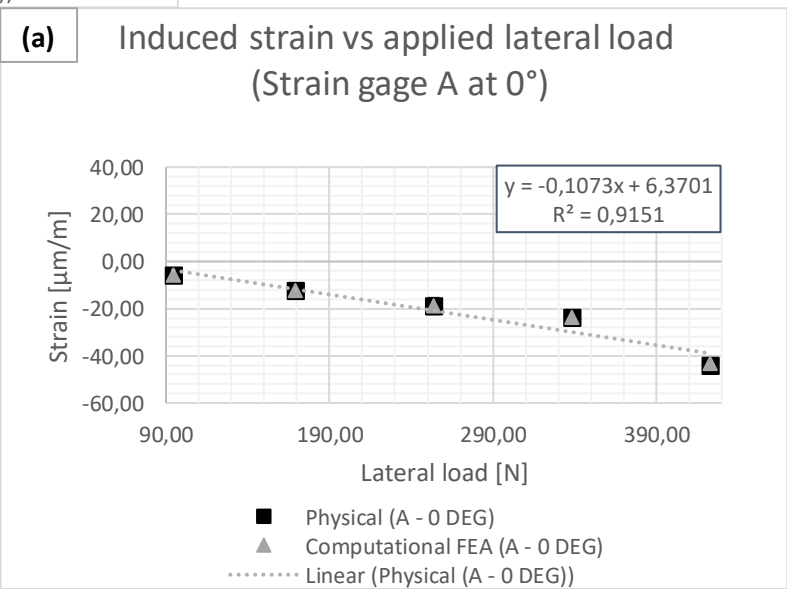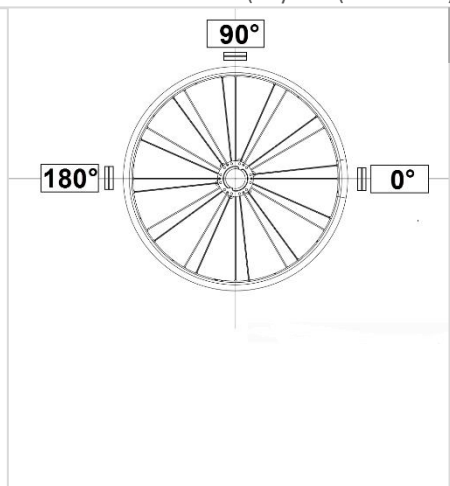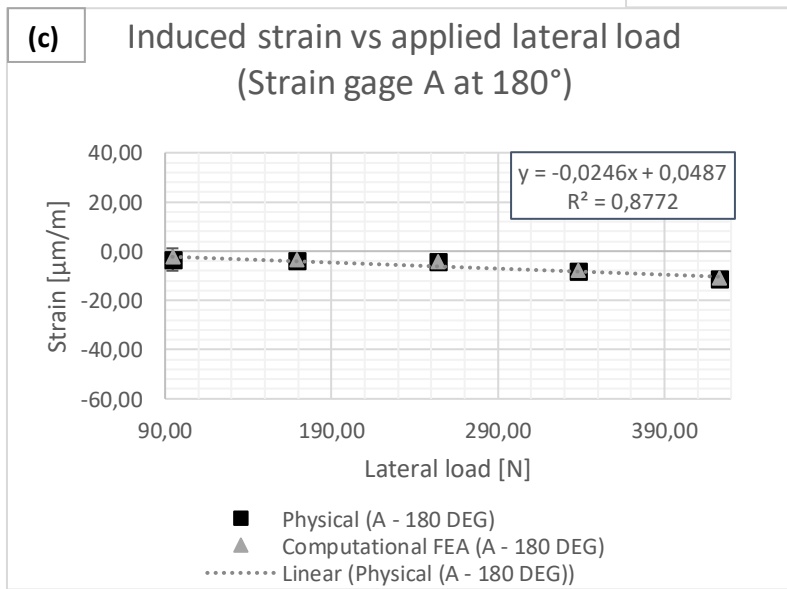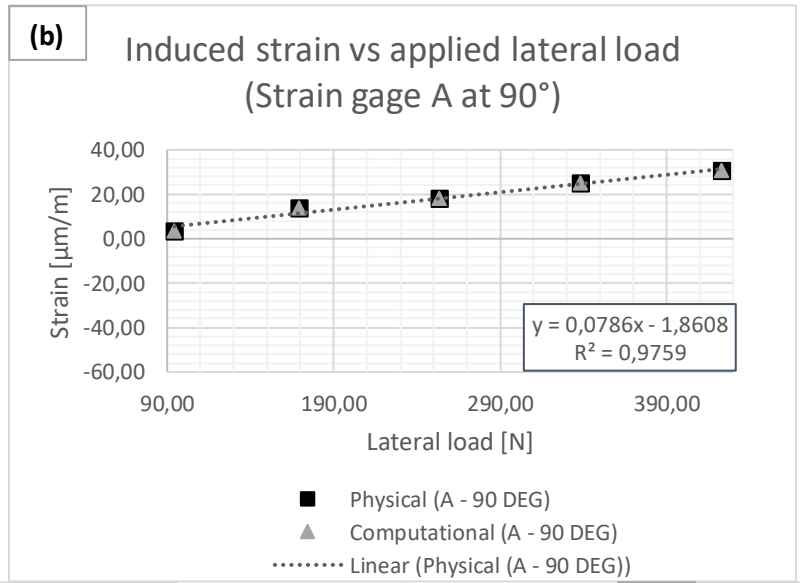
4.4 Wheel rim strain behaviour induced by applied lateral loading

The physical and computational wheel rim strains induced in the commercial wheel by means of applied lateral load only are presented against one another in Table 14.

Table 14 – Measured physical and computational *FEA* strains induced in the commercial wheel rim by applied lateral loading at tangential orientations of 0°, 90°, and 180°

Load [N]	Gage	Physically measured strain [μm/m]	Standard deviation of physical strain measurements [μm/m]	Error bar half-width [μm/m]	Computational *FEA* strain [μm/m]	Difference between physically measured and *FEA* strains [μm/m]	Percentage difference between physically measured and *FEA* strains*
Lateral loading 0 degrees							
94.39	A	-5.73	0.52	1.04	-5.89	0.16	2.72
	B	-2.03	0.18	0.36	-2.64	0.61	23.11
169.10	A	-12.53	1.20	2.4	-12.54	0.01	0.08
	B	-5.83	0.65	1.3	-5.81	0.02	0.34
253.64	A	-18.90	1.75	3.5	-18.97	0.07	0.37
	B	-10.33	0.99	1.98	-10.56	0.23	2.18
338.19	A	-23.83	0.38	0.76	-23.75	0.08	0.34
	B	-13.07	0.25	0.5	-12.86	0.21	1.63
422.97	A	-44.27	1.20	2.4	-43.37	0.90	2.08
	B	-14.17	0.38	0.76	-13.60	0.57	4.19
Lateral loading 90 degrees							
94.39	A	3.63	0.48	0.96	7.82	4.19	53.58
	B	0.33	2.28	4.56	1.72	1.39	80.81
169.10	A	13.87	0.32	0.64	16.06	2.19	13.64
	B	2.03	0.69	1.38	3.21	1.18	36.76
253.64	A	17.97	0.67	1.34	19.64	1.67	8.50
	B	2.00	0.00	0.00	4.20	2.20	52.38
338.19	A	25.10	0.96	1.92	26.29	1.19	4.53
	B	3.10	0.31	0.62	5.50	2.40	43.64
422.97	A	30.60	0.62	1.24	24.07	6.53	27.13
	B	3.00	0.00	0.00	2.47	0.53	21.46
Lateral loading 180 degrees							
94.39	A	-3.40	2.28	4.56	-2.40	1.00	41.67
	B	-2.37	1.63	3.26	-7.31	4.94	67.58
169.10	A	-3.93	0.69	1.38	-3.38	0.55	16.27
	B	-2.97	0.77	1.54	-2.27	0.70	30.84
253.64	A	-4.33	0.55	1.10	-4.37	0.04	0.92
	B	-3.23	0.43	0.86	-2.92	0.31	10.62
338.19	A	-8.20	0.41	0.82	-7.99	0.21	2.63
	B	-6.17	0.38	0.76	-3.83	2.34	61.10
422.97	A	-11.37	0.56	1.12	-10.99	0.38	3.46
	B	-8.93	0.52	1.04	-5.45	3.48	63.85

*Percentage difference between physically measured and *FEA* strains determined relative to computational *FEA* strain

(b) Induced strain vs applied lateral load (Strain gage A at 90°)

y = 0,0786x - 1,8608
R² = 0,9759

■ Physical (A - 90 DEG)
▲ Computational (A - 90 DEG)
········· Linear (Physical (A - 90 DEG))

(c) Induced strain vs applied lateral load (Strain gage A at 180°)

y = -0,0246x + 0,0487
R² = 0,8772

■ Physical (A - 180 DEG)
▲ Computational FEA (A - 180 DEG)
········· Linear (Physical (A - 180 DEG))

90°
180° **0°**

112

(a) Induced strain vs applied lateral load (Strain gage A at 0°)

y = -0,1073x + 6,3701
R² = 0,9151

■ Physical (A - 0 DEG)
▲ Computational FEA (A - 0 DEG)
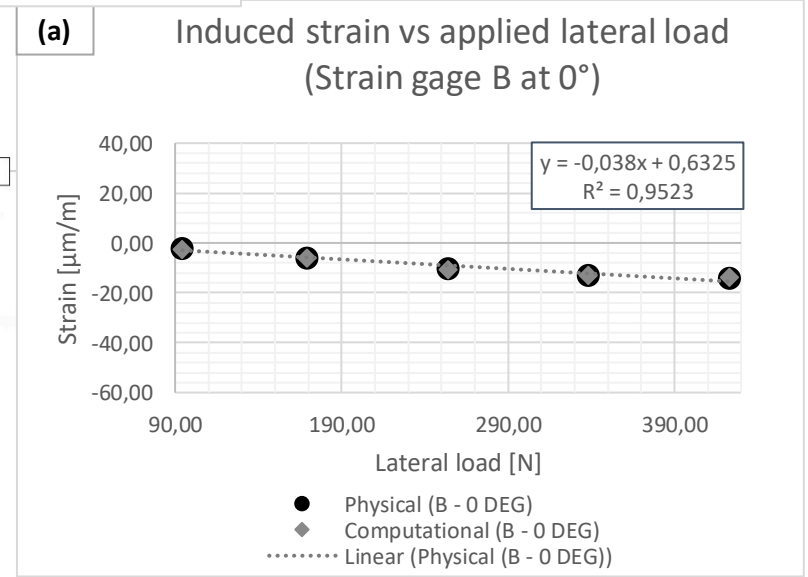········· Linear (Physical (A - 0 DEG))

Figure 53 (a) - Measured strain against applied lateral load (strain gage A; tangential orientation 0°; commercial wheel rim)
(b) - Measured strain against applied lateral load (strain gage A; tangential orientation 90°; commercial wheel rim)
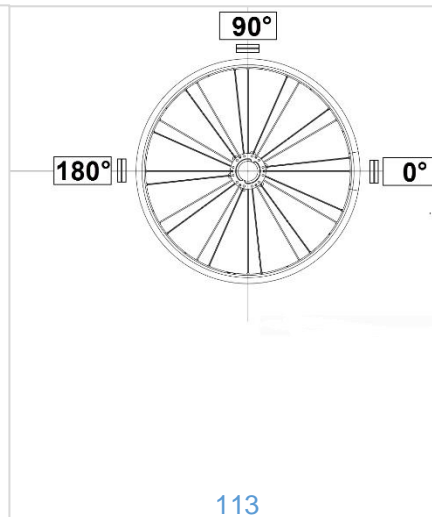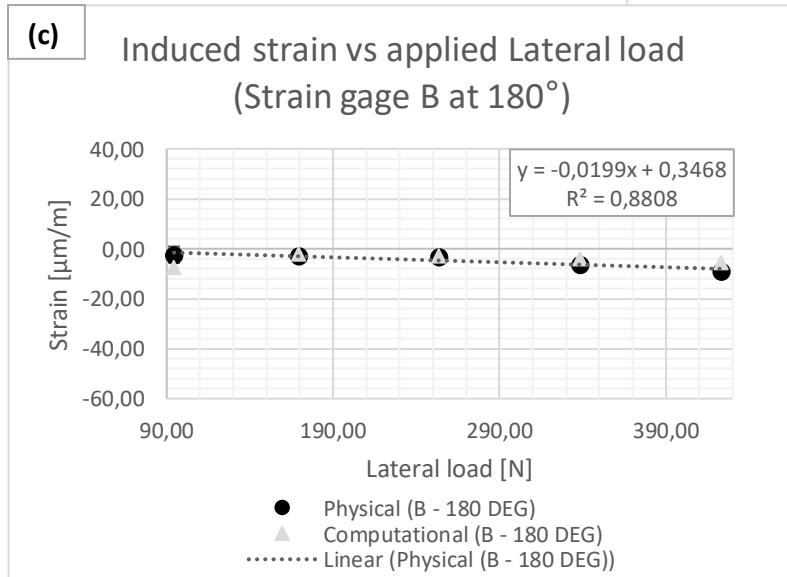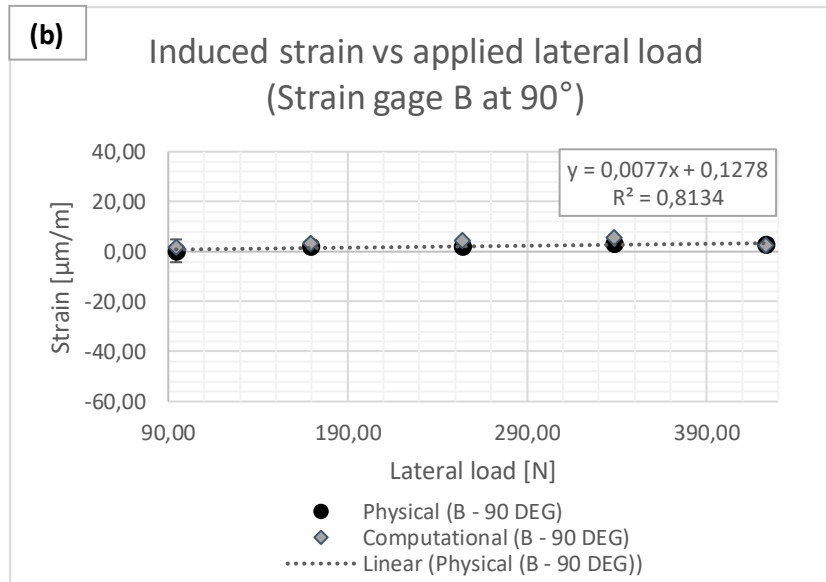**(c) - Measured strain against applied lateral load (strain gage A; tangential orientation 180°; commercial wheel rim)**

(b)

Induced strain vs applied lateral load
(Strain gage B at 90°)

$y = 0{,}0077x + 0{,}1278$
$R^2 = 0{,}8134$

Strain [μm/m] vs Lateral load [N]

● Physical (B - 90 DEG)
◆ Computational (B - 90 DEG)
········· Linear (Physical (B - 90 DEG))

90°

180°　**0°**

(c)

Induced strain vs applied Lateral load
(Strain gage B at 180°)

$y = -0{,}0199x + 0{,}3468$
$R^2 = 0{,}8808$

Strain [μm/m] vs Lateral load [N]

● Physical (B - 180 DEG)
▲ Computational (B - 180 DEG)
········· Linear (Physical (B - 180 DEG))

113

(a)

Induced strain vs applied lateral load
(Strain gage B at 0°)

$y = -0{,}038x + 0{,}6325$
$R^2 = 0{,}9523$

Strain [μm/m] vs Lateral load [N]

● Physical (B - 0 DEG)
◆ Computational (B - 0 DEG)
········· Linear (Physical (B - 0 DEG))

Figure 54 (a) - Measured strain against applied lateral load (strain gage B; tangential orientation 0°; commercial wheel rim)
(b) - Measured strain against applied lateral load (strain gage B; tangential orientation 90°; commercial wheel rim)
(c) - Measured strain against applied lateral load (strain gage B; tangential orientation 180°; commercial wheel rim)

The results presented in *Table 14* and *Figure 53* display a directly proportional relationship between the magnitudes of applied lateral load and compressive strains induced in the wheel rim for *gage A* at 0° and 180°. *Figure 53 (a)* and *(c)* indicate that a 328.52 N increase in applied lateral load respectively increased the physically measured compressive strains at these positions by 38.54 µm/m and 7.97 µm/m. For this same variation in applied lateral load, Figure 53 *(b)* shows that the recorded strain measurement for *gage A* at 90° became more tensile by 26.97 µm/m. These variations correspond to respective increases in compressive and tensile strain of approximately 7.7, 8.4, and 3.3 times more than the initially measured strain magnitudes (0° = -5.73 µm/m, 90° = 3.63 µm/m, and 180° = -3.4 µm/m) in the range of lateral loads from 94.39 N to 422.97 N.

Additionally, *Figure 54* shows that for the same variation in applied loading magnitude, the physical strain measurements for *gage B* at 0°, 90°, and 180° became respectively more compressive by 12.14 µm/m, -2.67 µm/m, and 6.56 µm/m. These variations correspond to increases in compressive strain of approximately 7.0 and 3.8 times more than the originally measured strains for *gage B* at 0° and 180°, and a corresponding growth in tensile strain of 9.1 times for *gage B* at 90°.

These results indicate that the applied lateral load has the greatest influence on the induced strains for both gages at 0°. This could mean that the wheel is most likely to fail at this tangential position if the applied lateral load is large enough to induce failure.

The accuracy with which the wheel was aligned relative to the applied lateral load at 0° in the testing apparatus could have influenced the measured physical strains. The variation in measured physical strain at *gages A* and *B* for each applied lateral load are shown against angle position in *Figure 55* and *Figure 56.*
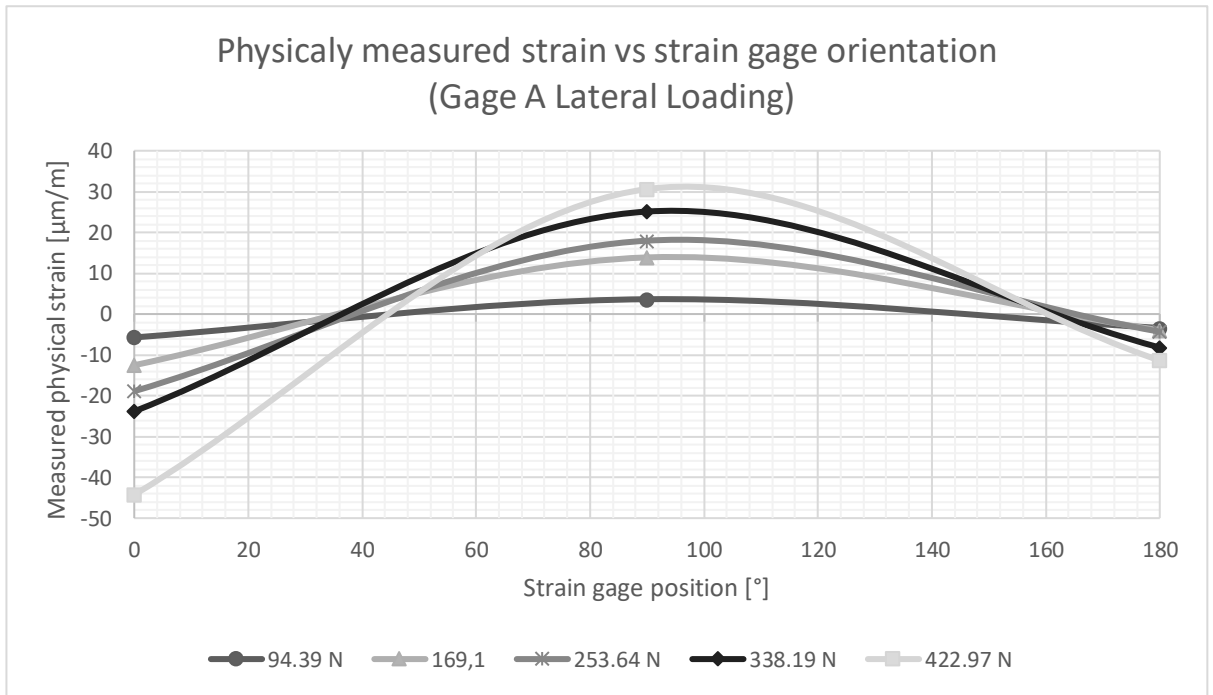
Figure 55 – Measured physical strain induced by each applied lateral loading magnitude against tangential strain gage position (*gage A*)
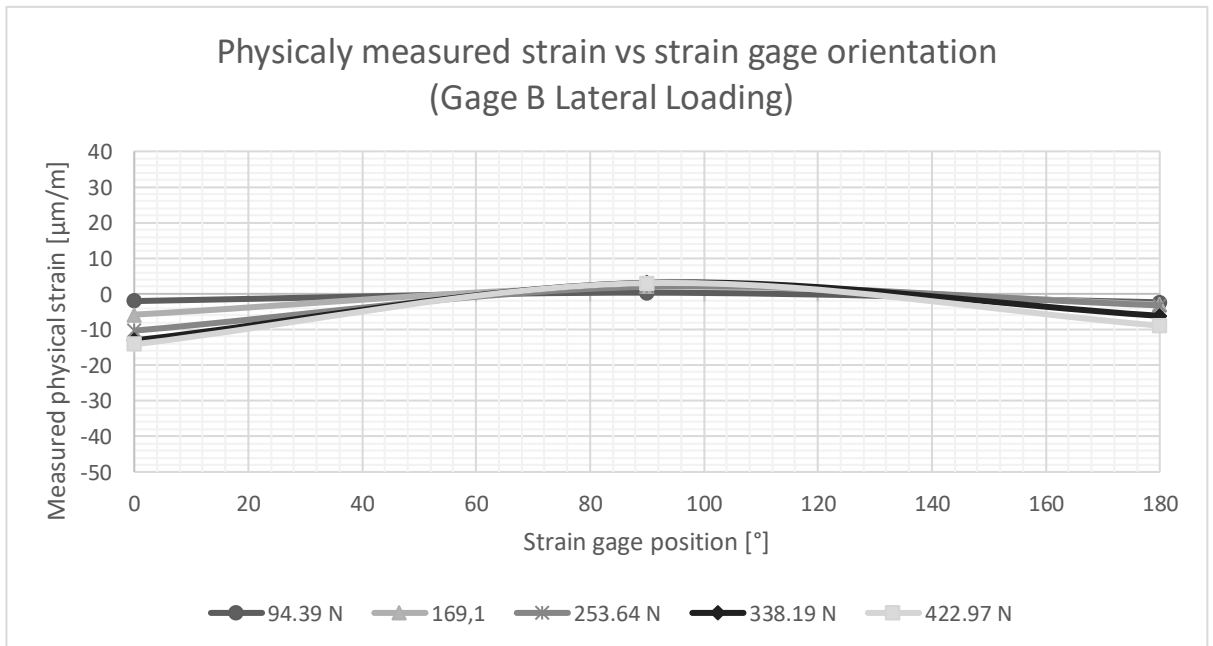

Figure 56 – Measured physical strain induced by each applied lateral loading magnitude against tangential strain gage position (*gage B*)

Figure 55 shows that as the strain gage position moved from 0° to 90°, the measured physical strains for *gage A* at 94.39 N and 422.97 N became respectively more tensile by 9.36 µm/m and 74.87 µm/m. Additionally, this

figure indicates that moving the strain gage position from 90° to 180° resulted in the measured physical strains becoming respectively more compressive by 7.03 µm/m and 41.97 µm/m.

For the same applied loads, it is shown in *Figure 56* that the physical strain measurements for *gage B* at 90° are 2.36 µm/m and 17.17 µm/m respectively more tensile than those at 0°. This figure also indicates that these strain measurements became increasingly more compressive by 2.7 µm/m and 11.93 µm/m as the strain gage position was changed to 180°.

These results suggest that the accuracy of the wheel alignment in the testing apparatus has the greatest influence on the physical strain measurements corresponding to *gage A* for all applied radial loads. This influence appears greatest between 0° and 90°. It seems that the gradients presented in both figures become steeper as the applied lateral load increases. These trends are unable to properly describe the influence which possible wheel misalignment in the testing apparatus has on the magnitude of recorded strain measurements. These strain variations are likely to have negligible influence in a combined loading scenario as they all appear to be less than 1.5 µm/m per degree.

The magnitudes of the recorded physical strain measurements were also dependent on the accuracy of the applied lateral loads. The gradients of the linear regressions shown in *Figure 53* and *Figure 54* may describe the effects of any possible inefficiency in the testing apparatus which could have altered the magnitudes of the loads applied during testing.

The regression gradients shown in *Figure 53 (a)* and *(c)* indicate that a 1 N increase in applied lateral load caused the measured strains for *gage A* at 0° and 180° to become respectively more compressive by 0.1073 µm/m and 0.0246 µm/m.

Additionally, *Figure 53 (b)* indicates that the same increase in applied load should result in a 0.0786 µm/m increase in tensile strain for *gage A* at 90°. For *gage B* at these respective positions, *Figure 54* shows that the corresponding

strain measurements are influenced by -0.038 µm/m, 0.0077 µm/m, and -0.0199 µm/m per 1 N increase in applied radial load.

These gradients indicate that the strain measurements at 0° would be influenced the most if any testing apparatus inefficiencies affected the magnitudes of the loads applied during testing. The greatest of these variations in strain corresponds to *gage A*, and is indicated as 0.1073 µm/m per 1 N of possible inefficiency. As such, they are likely to be negligible in a combined loading scenario.

The percentage of strain variation which each regression model may relate to the magnitude of applied lateral load is indicated by the coefficients of determination presented in *Figure 53* and *Figure 54.* At tangential positions of 0°, 90°, and 180°, they are respectively presented as 91.51, 97.59, and 87.72 percent for *gage A*, and as 95.23, 81.34, and 88.08 percent for *gage B*. This means that the regression models accurately describe the data in the range of applied radial loads.

Strain estimates made using these regression models may be utilized to determine confidence intervals which describe the repeatability of the experiment with a 95 percent certainty in the range of applied lateral loads. Additionally, the accuracy of these strain estimates may be quantified by means of prediction intervals of the same confidence. These intervals are shown in *Table 15* for both gages at tangential orientations of 0°, 90°, and 180°, and were calculated for 65 N intervals in the lateral load range from 95 N to 420 N.

Table 15- Confidence and prediction intervals for regressions modelling strain induced by lateral loading

Tangential strain gage position [°]	Lateral load [N]	Gage A			Gage B		
		Strain magnitude estimated using regression [µm/m]	95% CI half-width for regression repeatability [µm/m]	Prediction interval half-width for 95% confidence [µm/m]	Strain magnitude estimated using regression [µm/m]	95% CI half-width for regression repeatability [µm/m]	Prediction interval half-width for 95% confidence [µm/m]
0	95.00	-3.82	11.93	19.71	-2.98	3.11	5.13
	160.00	-10.79	9.07	18.12	-5.45	2.36	4.72
	225.00	-17.76	7.25	17.29	-7.92	1.89	4.50
	290.00	-24.74	7.31	17.31	-10.39	1.90	4.51
	355.00	-31.71	9.21	18.19	-12.86	2.40	4.74
	420.00	-38.68	12.11	19.82	-15.33	3.15	5.16
90	95.00	5.61	4.51	7.46	0.86	1.34	2.22
	160.00	10.72	3.43	6.86	1.36	1.02	2.04
	225.00	15.82	2.75	6.54	1.86	0.82	1.95
	290.00	20.93	2.77	6.55	2.36	0.82	1.95
	355.00	26.04	3.48	6.88	2.86	1.04	2.05
	420.00	31.15	4.58	7.50	3.35	1.36	2.23
180	95.00	-2.29	3.36	5.56	-1.54	2.67	4.41
	160.00	-3.89	2.56	5.11	-2.83	2.03	4.06
	225.00	-5.49	2.05	4.87	-4.12	1.62	3.87
	290.00	-7.09	2.06	4.88	-5.42	1.64	3.87
	355.00	-8.69	2.60	5.13	-6.71	2.06	4.07
	420.00	-10.29	3.41	5.59	-8.00	2.71	4.44

The presented confidence interval half-widths indicate that the respective strain co-ordinates of the regression lines corresponding to *gage A* at 0°, 90°, and 180° should not vary by more than 12.11 µm/m, 4.58 µm/m, and 3.41 µm/m if the experiment is repeated. For *gage B*, the corresponding half-widths were respectively determined as 3.15 µm/m, 1.36 µm/m, and 2.71 µm/m. This suggests that any regression models determined by repeating the experiment are likely to best resemble those in this dissertation for *gage B* at 90°. Conversely, the greatest variation between the regression models presented in this section and those formed by repeating the experiment is likely to correspond to *gage A* at 0°.

For *gage A* at 0°, 90°, and 180°, the prediction interval half-widths presented in *Table 15* indicate that strain estimates determined using these regressions should not vary from those measured physically by more than 19.82 µm/m, 7.5 µm/m, and 5.59 µm/m in the range of applied lateral loads. These half-widths are respectively presented for *gage B* as 5.16 µm/m, 2.23 µm/m, and 4.44 µm/m.

In comparison to the measured physical strains presented in *Table 14*, all of the corresponding *FEA* strains differed in magnitude. *Figure 53* indicates that an increase in applied lateral load of 328.58 N resulted in the *FEA* strains corresponding to *gage A* at 0° and 180° becoming respectively more compressive by 37.48 µm/m and 8.59 µm/m. These variations differ to those measured physically by 1.06 µm/m and 0.62 µm/m, and correspond to approximately 7.4 and 4.6 times more than the initial *FEA* strain magnitudes (0° = -5.89 µm/m, 180° = -2.40 µm/m).

For *gage A* at 90°, *Figure 53* illustrates an increase in tensile *FEA* strain of 16.25 µm/m in the radial load range from 94.39 N to 422.97 N. This increase in *FEA* strain corresponds to approximately 3.1 times more than the initial *FEA* strain of 7.82 µm/m. It differed to the corresponding variation in measured physical strain by 10.48 µm/m.

Figure 54 shows that for the same increase in applied lateral load, the *FEA* strains corresponding to *gage B* at 0° became more compressive by 10.96 µm/m. This variation in *FEA* strain corresponds to approximately 5.2 times more than the initial *FEA* strain magnitude of -2.64 µm/m. It was 1.18 µm/m less compressive than the corresponding variation in measured physical strain of -12.14 µm/m.

At 90° and 180°, the *FEA* strains corresponding to *gage B* became increasingly tensile as the magnitude of applied lateral load was increased from 94.39 N to 422.97 N. Respectively, the magnitudes of these variations are illustrated in *Figure 54* as 0.75 µm/m and 1.86 µm/m. They correspond to 1.4 and 0.7 times more than the initial *FEA* strain magnitudes of 1.72 µm/m and -7.31 µm/m, and differed to the corresponding physical strain variations by 1.92 µm/m and 8.42 µm/m.

According to the *FAA* acceptability criteria, some of the results presented in *Table 14* were acceptable. It is indicated that all of the measured physical strains corresponding to *gage A* at 0° differed from those determined through *FEA* by less than 3 percent. For *gage B* at this tangential position, the *FAA*

acceptability criteria was exceeded by 13.11 percent for the measured physical and *FEA* strains corresponding to an applied lateral load of 94.39 N.

Table 14 goes on to show that five of the differences between the measured physical and *FEA* strains at 90° and 180° were acceptable according to the *FAA* criteria. These five differences all correspond to *gage A*. Additionally, they correspond to lateral loads of 253.64 N and 338.19 N at 90°, and 253.64 N, 338.19 N, and 422.97 N at 180°. Their magnitudes respectively represent 8.5, 4.5, 0.92, 2.63, and 3.46 percent of the corresponding *FEA* strain magnitudes.

These differences imply that for lateral loading only, the *FEA* strains were not accurately representative of those measured physically. This means that either the physical test method utilized was inaccurate, or that the manner in which the loads and constraints were applied to the *FEA* model was incorrect. Although the differences between measured physical and *FEA* strains corresponding to applied lateral loading only were unacceptable according to the *FAA* criteria, they had negligible influence in a combined loading scenario.

4.5 Wheel rim strain behaviour induced by applied combined loading

The measured physical and *FEA* strains in the commercial wheel rim resulting from an applied combined loading scenario are compared to one another in *Table 16*.

Table 16 – Measured physical and computational *FEA* strains induced in the commercial wheel rim by combined loading at tangential orientations of 0°, 90°, and 180°

Tangential strain gage position [°]	Gage	Physically measured strain [µm/m]	Standard deviation of physical strain measurements [µm/m]	Computational *FEA* strain [µm/m]	Difference between physically measured and *FEA* strains [µm/m]	Percentage difference between physically measured and *FEA* strains*
0	A	-207.60	2.41	-205.00	2.60	1.27
	B	-8.90	2.83	-8.10	0.80	9.88
90	A	-146.40	4.93	-145.80	0.60	0.41
	B	-53.80	3.27	-52.15	1.65	3.16
180	A	-154.80	1.48	-151.40	3.40	2.25
	B	-62.60	2.65	-59.16	3.44	5.81

*Percentage difference between physically measured and *FEA* strains determined relative to computational *FEA* strain

In *Table 16*, the greatest of the presented physical strains induced by combined loading corresponds to *gage A* at 0°. It was measured as -207.60 μm/m, and was more compressive than the *FEA* strain at this position by 2.6 μm/m. This difference of 2.6 μm/m is presented in *Table 16* as 1.27 percent of the corresponding *FEA* strain magnitude. Although there is a difference between these strains, they both imply that the commercial wheel is likely to fail at 0° if the combined load magnitude is large enough to induce failure.

Additionally, *Table 16* indicates that the greatest percentage difference between the measured physical and *FEA* strains corresponds to *gage B* at 0°. This percentage difference was determined as 9.88 percent of the corresponding *FEA* strain magnitude.

According to the *FAA* acceptability criteria, the correlation between the measured physical and *FEA* strains corresponding to a combined loading scenario was acceptable. Since all of the subsequent *FEA* analyses and optimizations were performed according to a combined loading scenario, the *FEA*s and constraint methods applied in this chapter were utilized throughout the remainder of this study.

4.6 Chapter summary and conclusion

In this chapter, measured physical strains induced in a commercial wheel rim by means of a static-load test rig were compared to *FEA* strains. These strains were induced according to pressure, radial, lateral, and combined loads, and measured using two strain gages, *A* and *B*, at tangential positions of 0°, 90° and 180° relative to the applied loading. In doing so, a comparative benchmark was established against which the strain behaviour of all other wheels produced in this dissertation could be compared. This comparison was also utilized to investigate how accurately the applied *FEA* loads and constraints represented reality, as well as the quality of the physical strain measurements obtained by utilizing the static load test rig.

Increasing the tyre inflation pressure from 180 kPa to 250 kPa resulted in the measured physical strains in each gage becoming respectively more

compressive by approximately 2.4 and 2.3 times more than the originally measured strain magnitudes of -57.6 µm/m and -17.23 µm/m. This variation in compressive strain was significant and showed that pressure loading did need to be included in the *FEA*s and optimizations performed for this dissertation. The *FEA* strains in the commercial wheel model differed from those measured physically by between 1.0 and 9.59 percent. This was acceptable according to the *FAA* acceptability criteria of 10 percent allowable deviation between measured physical and *FEA* strains, and implied that the static load test rig could produce acceptable results for pressure loads.

For *gage A*, increasing the applied radial load from 111.64 N to 500.27N caused the measured physical strains in the commercial wheel rim at 0°, 90°, and 180° to become respectively more compressive by approximately 3.6, 2.9, and 10.8 times that of the originally measured strain magnitudes of -12.07 µm/m, -1.60 µm/m, and -0.40 µm/m. The same increase in applied radial load caused the measured physical strain in *gage B* at 0° to become more tensile by 3.5 times when compared to the originally measured strain magnitude of 12.54 µm/m. For *gage B* at 90° and 180°, this increase in applied radial load resulted in the originally measured strains of -1.43 µm/m and -1.13 µm/m becoming more compressive by 3.2 and 9.0 times. The *FEA* strains corresponding to both gages differed from those measured physically by between 0.05 and 56.51 percent. This indicated that the static load test rig could not be utilized for physical strain measurements corresponding to applied radial loads only. Although these differences were unacceptable according to the *FAA* acceptability criteria, they had negligible effect in a combined loading scenario.

As the magnitude of applied lateral load increased from 94.39 N to 422.97 N, the measured physical strains corresponding to *gage A* at 0° and 180° became more compressive by 7.7 and 3.3 times when compared to the originally measured strain magnitudes of -5.73 µm/m and -3.4 µm/m. For *gage A* at 90°, the same increase in applied lateral load resulted in the originally measured physical strain magnitude of 3.63 becoming more tensile by 8.4 times. The strain magnitudes corresponding to *gage B* at 0°, 90°, and 180° respectively increased by approximately 7.0, 9.10, and 3.8 times more than the originally

measured strain magnitudes of -2.03 µm/m, 0.33 µm/m, and -2.37 µm/m in the range of applied lateral loads. These measured physical strains differed from those determined through *FEA* by up to 80.81 percent, and indicated that the static load test rig could not be used to record physical strains induced by lateral loading only. However, these differences had a negligible effect in a combined loading scenario.

Finally, measured physical strains induced by a combined loading scenario consisting of a 200 kPa tyre inflation pressure, and radial and lateral loads of 500.27 N and 422.97 N were compared to corresponding *FEA* strains. The magnitudes of these physical strains varied from those determined through *FEA* by between 0.41 and 9.88 percent. This indicated that according to the *FAA* acceptability criteria, good correlation existed between the measured physical and *FEA* strains corresponding to a combined loading scenario. All of the subsequent *FEA*s, optimizations, and physical strain measurements in this dissertation corresponded to a combined loading scenario.

Chapter 5: Results of wheel designs produced by structural topology optimization

5.1 Introduction

In this chapter, the mass and stiffness of wheel designs produced by means of structural topology optimization software are presented. The following themes addressed in this chapter include:

I.   Strain behaviour of the established base model

II.   The mass and stiffness of wheel geometries produced by means of computationally applied structural topology optimization techniques

III.   The refinement of the optimum geometry for manufacture as a composite structure

5.2 Structural topology optimization base model

The mass of the 13.40 kg 6061-T6 aluminium alloy wheel base model corresponds to 17.34 times that of the 722.61 gram commercial wheel. Such a gross difference in component mass suggests that the wheel base model should be inherently stiffer than the commercial wheel owing to the presence of more material. The computational *FEA* strain behaviour of the wheel base model is shown against that of the commercial wheel in *Table 17*.

Table 17 - Comparative *FEA* strain behaviour of wheel base model for structural topology optimization against commercial wheel rim

13.40 kg Wheel base model				0.722 kg Commercial wheel model	Difference between base model and commercial wheel rim *FEA* strains [μm/m]	Percentage difference between average base model and commercial wheel rim *FEA* strains*
Strain Gage Orientation [°]	Mesh	*FEA* strain [μm/m]	Mean *FEA* strain [μm/m]	*FEA* Strain [μm/m]		
0	Standard	-2.564	-2,63	-205.00	202.37	98.72
	1mm Refinement	-2.491				
	0.5mm Refinement	-2.840				
90	Standard	-0.007	-0.57	-145.80	145.24	99.61
	1mm Refinement	-1.338				
	0.5mm Refinement	-0.349				
180	Standard	-2.314	-2,46	-151.40	148.94	98.38
	1mm Refinement	-2.517				
	0.5mm Refinement	-2.542				

*Percentage difference between average base model and commercial wheel rim *FEA* strains determined relative to *FEA* strains in commercial wheel model

The results presented in *Table 17* indicate that the mean *FEA* strains in the rim of the wheel base model at 0°, 90°, and 180° were less than those in the commercial wheel model by 202.37 μm/m, 145.24 μm/m, and 148.94 μm/m respectively. These differences respectively correspond to 98.72, 99.61, and 98.38 percent of the *FEA* strains in the commercial wheel rim (0° = -205.00 μm/m, 90° = -145.80 μm/m, and 180° = -151.40 μm/m). This implies that the wheel base model is stiffer than the commercial wheel model. Specifically, this comparison served to verify that the wheel base model to which structural topology optimization techniques were applied was adequately stiff to allow for feasible optimization solutions to be produced.

The von Mises stresses in the wheel base model are shown in *Figure 57* as determined through linear static *FEA*. They were determined to investigate whether or not yielding would be initiated in the model as a result of the applied loading.
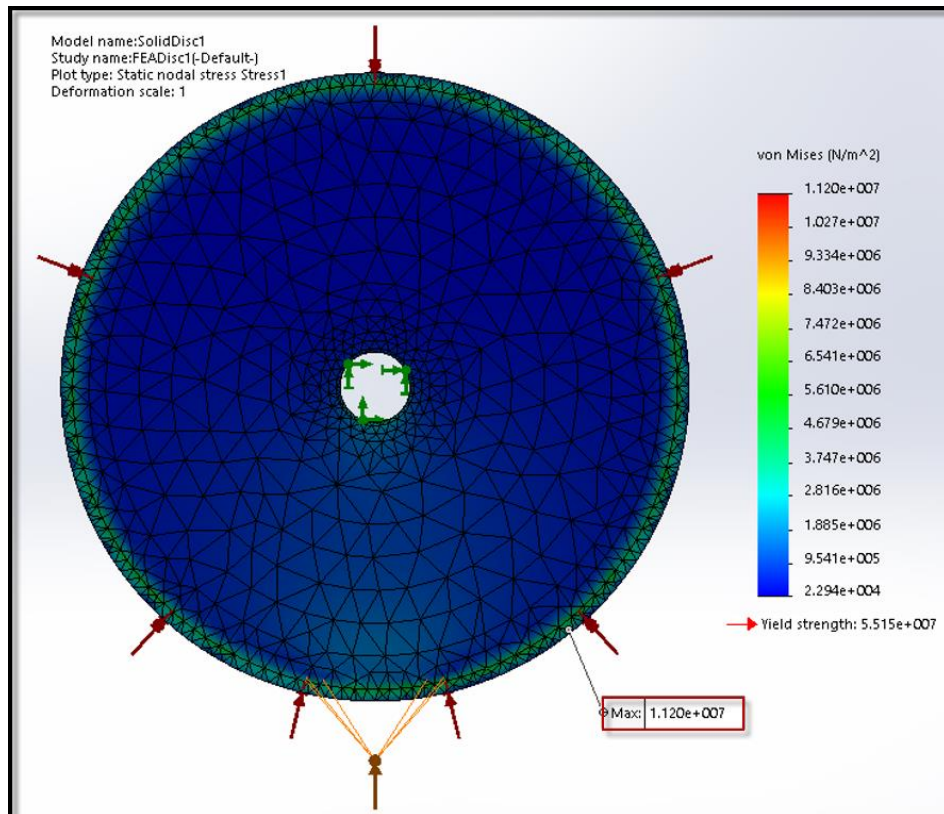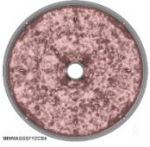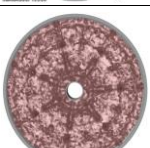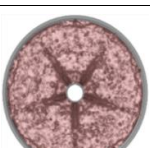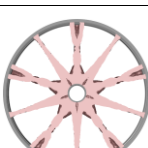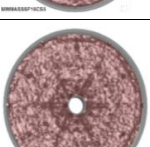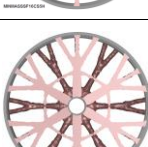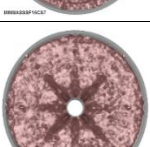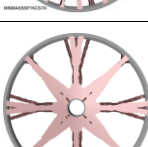
Figure 57 - Maximum von Mises stress induced in wheel base model (combined loading: *Table 7, Dassault Systèmes SolidWorks*)

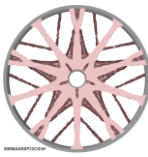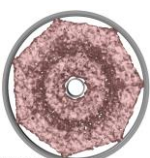The maximum von Mises stress in the wheel base model is shown in *Figure 57* as 11.20 MPa. This corresponds to 20.31 percent of the material yield strength (55.15 MPa). Additionally, the von Mises stresses induced in the wheel base model illustrated that it would not fail. These results implied that the wheel base model had significant potential for mass reduction through structural topology optimization. The wheel designs formed from this base model during structural topology optimization are presented in the following section.

5.3 Mass and stiffness of wheel geometries designed using structural topology optimization software

In accordance with the governing factors summarized in *Table 7*, the mass and stiffness of each of the 48 wheel geometries produced by means of the structural topology optimization software are presented in *Table 18*. The following paragraphs aim to describe the selection process utilized to identify a solution which was ideally suited to the purpose of this study.

Table 18 - Summary of wheel designs produced by means of structural topology optimization

Safety factor	Cyclic symmetry	No hole				Hole allowed			
		Wheel geometry	Mass [kg]	Stiffness [N/m]	Specific stiffness [N/m]	Wheel geometry	Mass [kg]	Stiffness [N/m]	Specific stiffness [N/m]
1.2	4		5.648	0.675	0.120		1.146	0.338	0.295
	5		5.553	0.536	0.097		1.336	0.405	0.303
	6		5.611	0.842	0.150		1.824	0.904	0.496
	7		5.639	0.597	0.106		1.814	0.642	0.354
1.6	4		5.675	0.771	0.136		1.737	0.642	0.370
	5		5.954	0.826	0.139		1.908	0.679	0.356
	6		5.744	1.000	0.174		2.071	0.975	0.471
	7		5.817	0.805	0.138		2.127	0.931	0.438
2.0	4		5.944	1.025	0.172		2.458	1.077	0.438

Design volume	Cyclic symmetry	No hole				Hole allowed			
		Wheel geometry	Mass [kg]	Stiffness [N/m]	Specific stiffness [N/m]	Wheel geometry	Mass [kg]	Stiffness [N/m]	Specific stiffness [N/m]
	5		5.954	1.032	0.173		3.037	1.198	0.394
	6		6.001	1.362	0.227		4.542	1.443	0.318
	7		6.031	1.042	0.173		2.879	1.340	0.465

Maximum stiffness study									
		No hole				**Hole allowed**			
Design volume	**Cyclic symmetry**	**Wheel geometry**	**Mass [kg]**	**Stiffness [N/m]**	**Specific stiffness [N/m]**	**Wheel geometry**	**Mass [kg]**	**Stiffness [N/m]**	**Specific stiffness [N/m]**
5	4		0.276	0.215	0.779		0.383	0.371	0.969
	5		0.276	0.202	0.732		0.511	0.345	0.675
	6		0.276	0.321	1.163		0.476	0.545	1.145
	7		1.594	0.301	0.189		0.405	0.368	0.909
25	4		3.423	1.003	0.293		2.890	4.183	1.447
	5		3.885	1.204	0.310		1.771	2.561	1.446
	6		3.962	1.080	0.273		2.828	5.145	1.819

	7		3.887	1.199	0.308		1.723	2.397	1.391
50	4		7.176	13.449	1.874		6.708	15.234	2.271
	5		7.145	14.474	2.026		6.769	13.123	1.939
	6		7.502	19.062	2.541		6.852	19.387	2.829
	7		7.808	15.256	1.954		6.985	11.404	1.633

Three of the 48 wheel solutions presented in *Table 18* appeared to be infeasible as they possessed no visible means of connection between the wheel hub and rim circumference. These solutions were produced according to a '*Maximum Stiffness*' objective function with a target design volume of 5 percent, an applied '*No Hole*' split draw constraint, and respective cyclic symmetry constraints of 4, 5, and 6 degrees. As they were functionally infeasible, they were not considered further in this study.

The remaining 45 wheel designs presented in *Table 18* were required by the *Nelson Mandela University Eco Car Project* to be at least 50 percent lighter (6.70 kg) than the original base model (13.40 kg), and have a stiffness of at least 1 N/m for each kilogram of component mass. This stiffness parameter is presented in *Table 18* as '*Specific stiffness*', and was defined as the ratio of component stiffness to mass.

Table 18 shows that all of the wheel designs corresponding to a '*Maximum Stiffness*' optimization function with a target design volume of 50 percent weighed more than 6.70 kilograms. As these eight wheel designs were not 50

percent lighter than the original base model, they did not meet the requirements necessary for the optimum wheel geometry.

Additionally, it is indicated that none of the 24 wheel designs satisfying a 'Minimum Mass' objective function met the stiffness requirement of at least 1 N/m for each kilogram of component mass. This requirement was also not met by the wheel designs corresponding to a 'Maximum Stiffness' objective function with the following additional parameters:

I.   A 'No Hole' split draw constraint with a target design volume of 5 percent and 7 degrees of cyclic symmetry

II.   A 'No Hole' split draw constraint with a target design volume of 25 percent and respective cyclic symmetry degrees of 4, 5, 6, and 7

III.   A 'Hole Allowed' split draw constraint with a target design volume of 5 percent and respective cyclic symmetry degrees of 4, 5, and 6

Although 43 wheel designs did not meet the necessary requirements, 5 potentially suitable wheel designs were produced. The geometry, degrees of cyclic symmetry, mass, and stiffness of each of these 5 wheel designs are presented in Table 19.

Table 19 - Most efficient wheel geometries produced through structural topology optimization
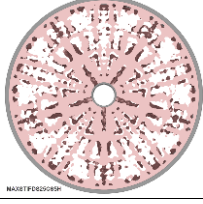
Produced geometry		Degrees of cyclic symmetry	Component mass [kg]	Component stiffness [N/m]	Specific stiffness [(N/m)/kg]
MAXSTIFDS05CS6H		6	0.476	0.545	1.145
MAXSTIFDS25CS7H		7	1.723	2.397	1.447
MAXSTIFDS25CS5H		5	1.771	2.561	1.446
MAXSTIFDS25CS4H		4	2.890	4.184	1.391
MAXSTIFDS25CS6H		6	2.828	5.145	1.819

Table 19 indicates that *MAXSTIFDS05CS6H* had a mass of 476 grams and a stiffness of 0.545 N/m. This corresponds to a specific stiffness of 1.145 N/m for each kilogram of component mass. In comparison to the other 4 wheel designs presented, this wheel had the lowest specific stiffness. This means that of the 5 wheel geometries presented in *Table 19*, *MAXSTIFDS05CS6H* offered the least stiffness in return for component mass. As such, it was not selected as the wheel geometry most suited to the intention of this dissertation.

Secondly, inspection of *MAXSTIFDS25CS7H* and *MAXSTIFDS25CS5H* (seen in greater detail in *Figure 58*) highlights a vast number of intricately shaped voids and discontinuities. It was put forward by local composites experts that, in accordance with manufacturing experience and knowledge, the presence of such voids may contribute to poor component structural integrity consequential of reinforcement fibre discontinuities.
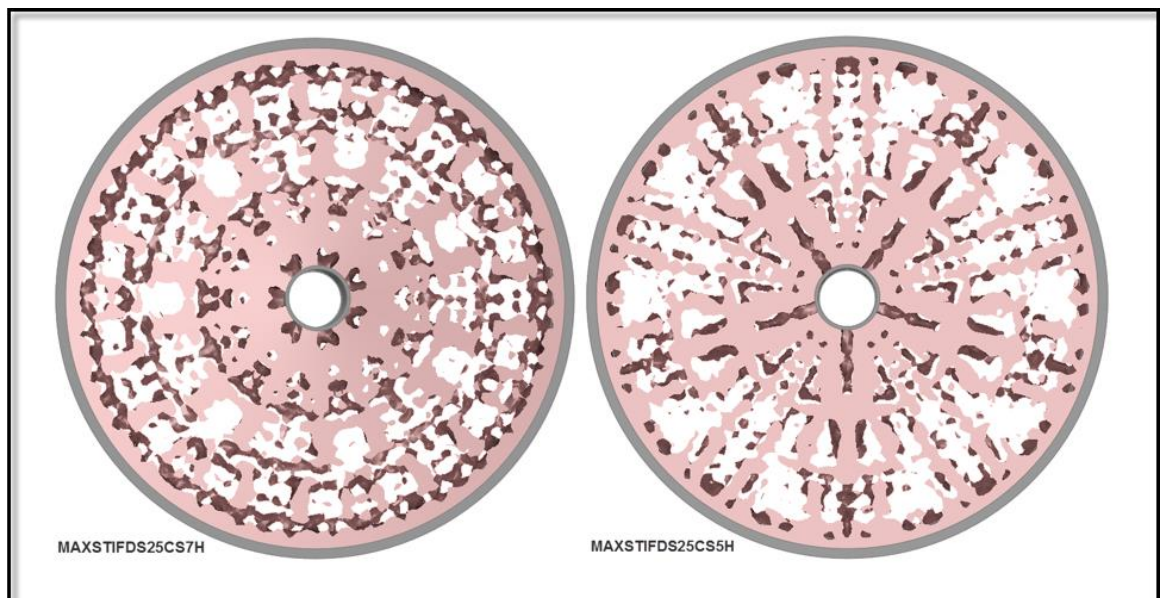
Figure 58 - MAXSTIFDS25CS7H & MAXSTIFDS25CS5H Wheel geometries (*solidThinking Inspire*)

If these wheels were manufactured as composite components, they would have required a great number of small laminae to form the intricate geometric features mentioned in the previous paragraph. These small laminae would have had to be joined by the matrix material in an overlapping, or butt-type fashion. This means that loads applied to the wheel could not be transferred between the wheel hub and rim continuously through the reinforcement fibres. As such, the load bearing capability of the wheels would likely be governed by the strength of the epoxy-resin utilized during component manufacture. Since the tensile strength of the matrix material utilized in this study was less than that of the reinforcement material, these wheels were likely to be weaker than a wheel constructed using continuous fibres to connect the wheel rim hub and circumference.

The next wheel design reviewed was *MAXSTIFDS25CS4H*. This wheel had a mass of 2.890 kg, and a stiffness of 4.184 N/m. The corresponding specific stiffness is presented in *Table 19* as 1.391N/m for each kilogram of component mass. In comparison to the other four wheels presented, it had the second-lowest specific stiffness. Additionally, it is shown to be 2 grams heavier than *MAXSTIFDS25CS6H,* and less stiff by 0.961 N/m. Consequently, this wheel was not selected as the most ideally suited to this study.

Table 19 indicates that *MAXSTIFDS25CS6H* (presented in greater detail in the *Figure 59)* had a mass of 2.828 kg. This corresponds to a 78.9 percent mass reduction when compared to the original base model. The stiffness of this wheel is presented in *Table 19* as 5.145 N/m, and corresponds to a specific stiffness of 1.819 N/m for each kilogram of component mass. In comparison to the four other wheels presented, *MAXSTIFDS25CS6H* had both the greatest stiffness, and specific stiffness.
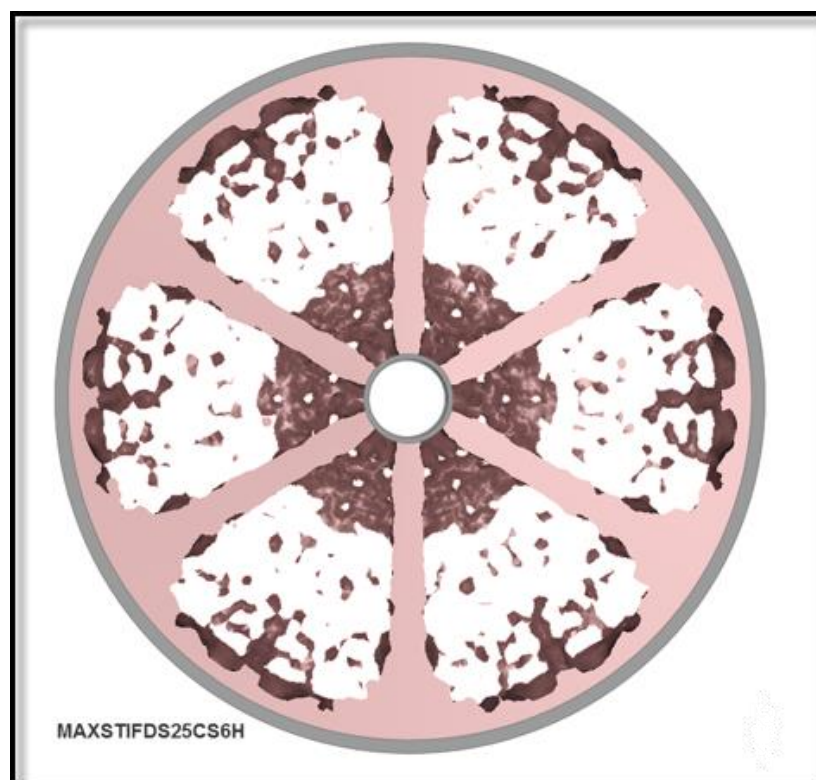
Figure 59 - MAXSTIFDS25CS6H Wheel geometry (*solidThinking Inspire*)

Local composites experts stated that this wheel geometry possessed great potential for manufacture as a composite component owing to its well defined

continuous sections, and relatively large *'organically'* shaped voids. These characteristics would allow for the wheel to be constructed as a composite component consisting of continuous reinforcement fibres between the wheel hub and rim. This would most likely be the strongest means of connecting these two entities as it would allow for applied loads to be transferred continuously through the reinforcement fibres.

Additionally, it was stated that the relatively large *'organically'* shaped voids were suited to the geometry of a well-designed composite component. The shape of these voids produced gradual cross-sectional changes of the wheel spokes. This was likely to reduce the influence of stress concentrations brought about by sharp bends in the reinforcement fibres.

In summary, *MAXSTIFDS25CS6H* met all of the necessary requirements of the optimum wheel geometry. Of the 5 wheel designs presented in *Table 19*, it offered the greatest component stiffness, both overall, and for each kilogram of component mass. Additionally, it was seen by local composites experts as the wheel geometry most well suited to manufacture as a composite component. For these reasons, it was selected as the 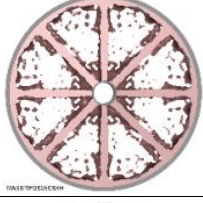optimum wheel geometry produced using structural topology optimization software. The influence which further geometric refinement had on the mass and strain behaviour of this component is presented in the following section.

5.4 Refinement of optimum geometry for manufacture as a composite

The previously identified *MAXSTIFDS25CS6H* was geometrically refined for the purpose of improving its suitability towards being manufactured as a composite component. *FEA* software was utilized to investigate whether or not this refinement was capable of withstanding the applied combined loading scenario as shown in *Figure 60*.
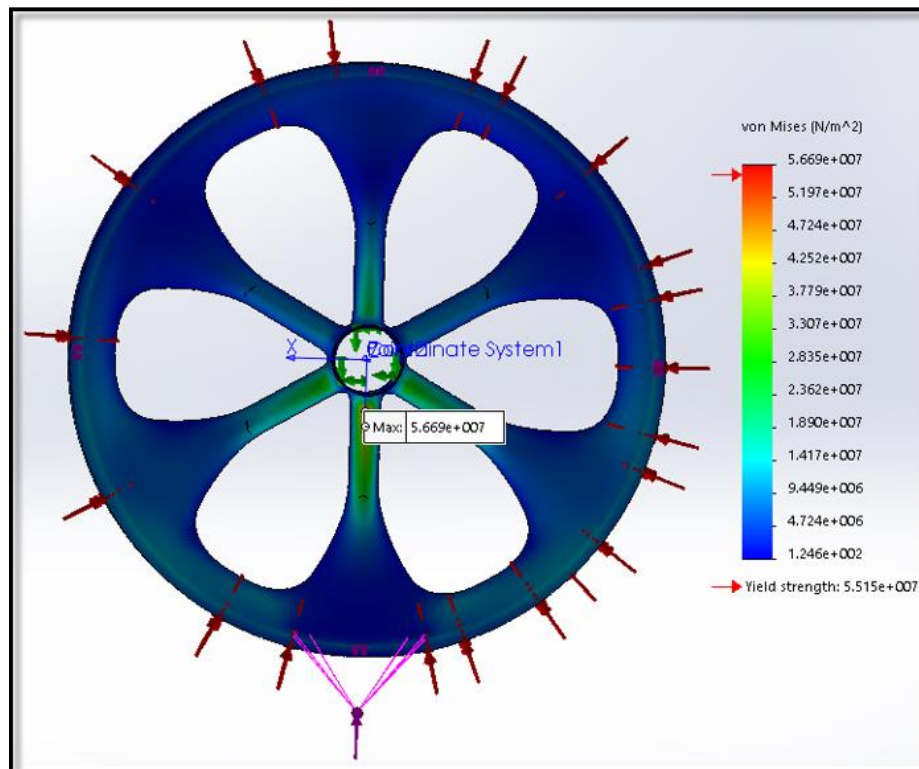
**Figure 60 - Finite element analysis of first proposed geometric refinement
(MAXSTIFDS25CS6H, *Dassault Systèmes SolidWorks*)**

A review of *Figure 60* indicates that the maximum von Mises stress induced in this proposed refinement exceeded the yield strength of the 6061-T6 aluminium alloy (55.15 MPa) by approximately 1.54 MPa. This means that the refined alloy wheel geometry would fail as a result of yielding if it experienced the anticipated loading scenario.

Additionally, *Figure 60* illustrates that this yielding would occur in the wheel spokes close to the wheel hub. This was most likely due to a stress concentration produced by the relatively small radius between each of the wheel spokes at the position where they joined to the wheel hub.

As such, the wheel geometry was further refined by means of increasing the fillet radius in this vicinity as shown in *Figure 61*. *FEA* software was again utilized to determine whether or not this second geometric refinement would reduce the stress concentration in the wheel spokes. The von Mises stresses determined during this *FEA* are shown in *Figure 62*.
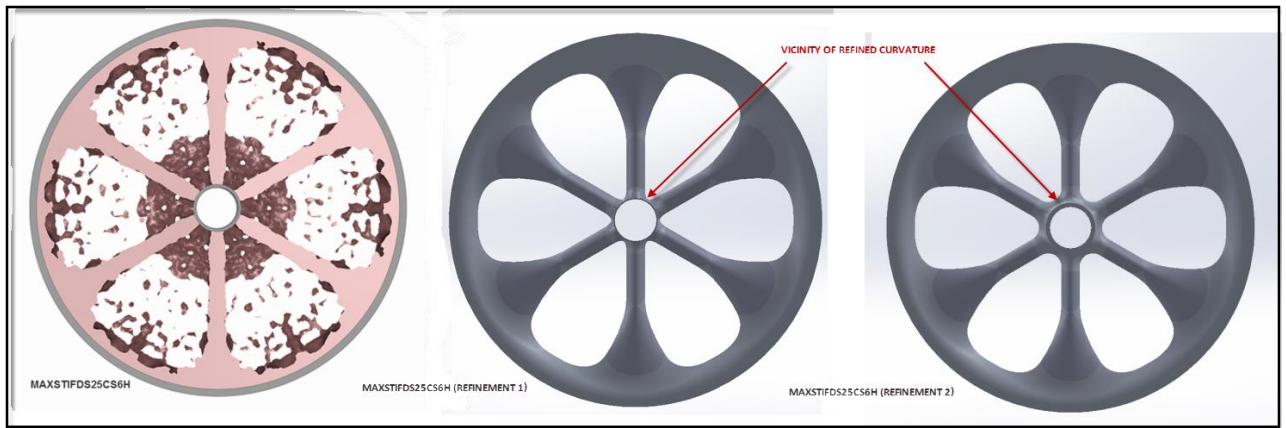
Figure 61 - MAXSTIFDS25CS6H alongside first and second proposed refinements
(*solidThinking Inspire*)
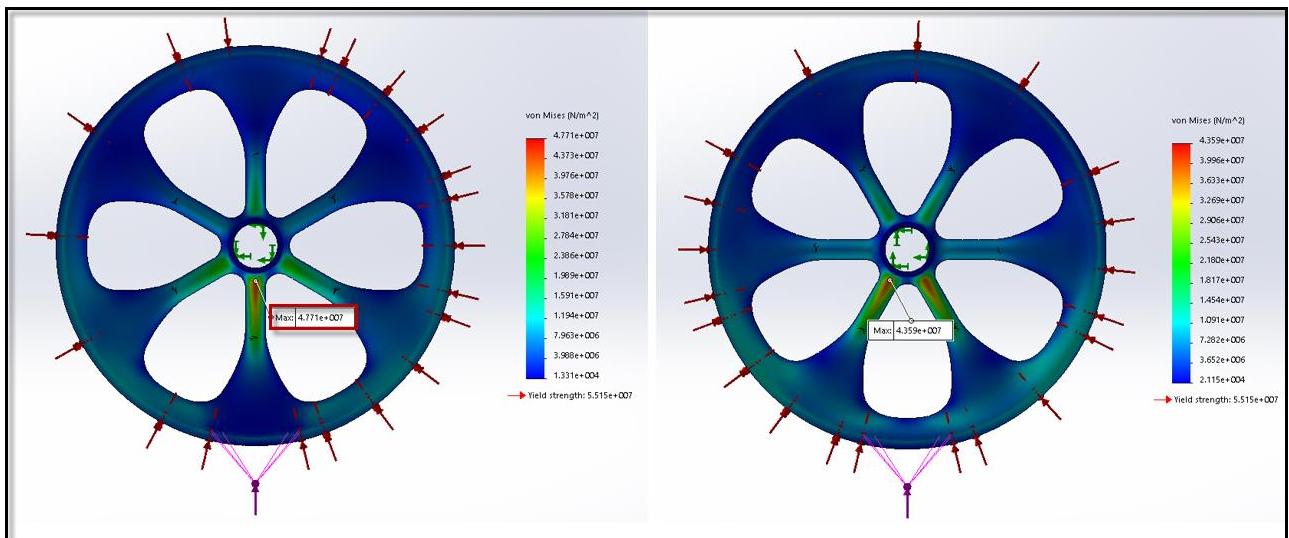
Figure 62 - Finite element analysis of second proposed refinement
(MAXSTIFDS25CS6H, *Dassault Systèmes SolidWorks*)

Figure 62 indicates that maximum von Mises stresses in the second geometric refinement were determined using *FEA* software as 47.71 MPa when the loading was applied directly in-line with a wheel spoke, and 43.59 MPa when directly midway between two spokes. These values correspond to approximately 87 and 79 percent of the 6061-T6 aluminium alloy yield strength (55.15 MPa) respectively. Additionally, they showed that this wheel would not fail as a result of yielding during normal operation. As such, no further refinements were made to the geometry of *MAXSTIFDS25CS6H.*

The mass of this geometrically refined wheel model is shown alongside those of *MAXSTIFDS25CS6H* and the optimization base model in *Figure 63*. This figure

aims to serve as a simple means of illustrating how each stage structural of topology optimization influenced component mass.
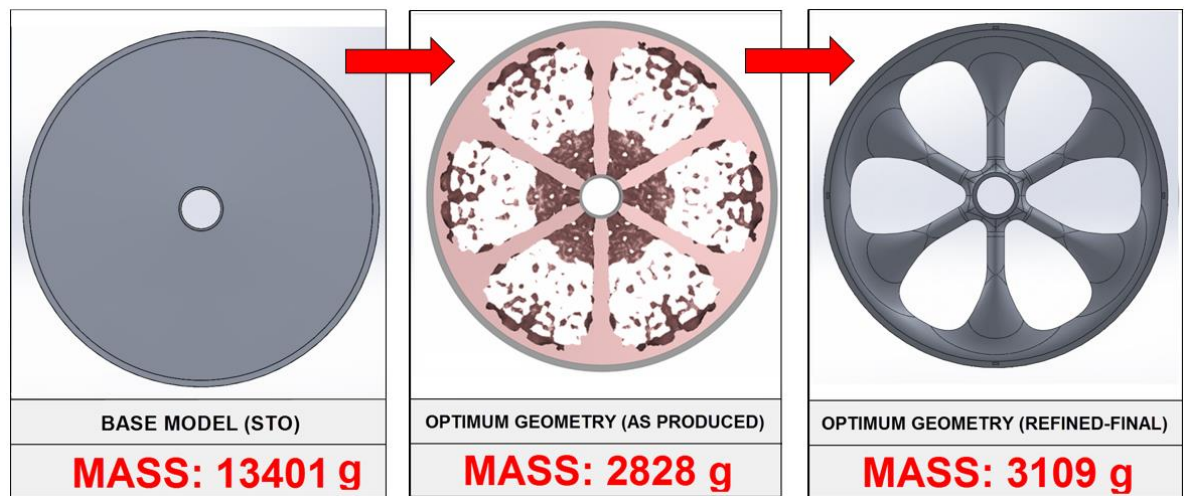
Figure 63 - Variance in component mass produced by each stage of structural topology optimization (*solidThinking Inspire*)

Figure 63 shows that the mass of the refined optimum wheel model was determined using *FEA* software as 3.11 kg. This corresponds to an increase in mass of 281 grams, or 9.9 percent, when compared to *MAXSTIFDS25CS6H* (2.83 kg). Additionally, it shows that component mass may increase during the geometric refinement of a solution produced using structural topology optimization software.

In comparison to the mass of the initial base model (13.40 kg), this refined geometry was 10.29 kg lighter. This represents a decrease in component mass of approximately 77 percent during the entire optimization process. Additionally, it confirms that a significant reduction in component mass may be achieved by using structural topology optimization software.

The computational *FEA* strain behaviour of this geometrically refined wheel model is shown against that of the initial base model and commercial wheel in *Table 20*. These *FEA* strains were determined according to loading applied directly in-line with a wheel spoke, and exactly mid-way between two spokes at tangential strain gage orientations of 0°, 90°, and 180°.

Table 20 – Comparison of *FEA* strain behaviour for refined optimum wheel geometry against base model and commercial wheel models

Tangential strain gage position [°]	*FEA* strain [µm/m]		Difference in *FEA* strains between refined optimum wheel geometry and base model [µm/m]	Percentage difference in *FEA* strains between refined optimum wheel geometry and base model*
	Refined optimum wheel geometry (loading applied in-line with a spoke)	Base Model		
0	-1.14	-2.63	1.49	56.65
90	-88.50	-0.57	87.93	15426.84
180	-55.90	-2.46	53.44	2172.40
Tangential strain gage position [°]	*FEA* strain [µm/m]		Difference in *FEA* strains between refined optimum wheel geometry and base model [µm/m]	Percentage difference in *FEA* strains between refined optimum wheel geometry and base model*
	Refined optimum wheel geometry (Loading applied mid-way between two spokes)	Base model		
0	-28.04	-2.63	25.41	966.16
90	-62.36	-0.57	61.79	10840.35
180	-69.64	-2.46	67.18	2730.89
Tangential strain gage position [°]	*FEA* strain [µm/m]		Difference in *FEA* strains between refined optimum wheel geometry and commercial wheel model [µm/m]	Percentage difference in *FEA* strains between refined optimum wheel geometry and commercial wheel model**
	Refined optimum wheel geometry (loading applied in-line with a spoke)	Commercial wheel model		
0	-1.14	-205.00	203.86	99.44
90	-88.50	-145.80	57.30	39.30
180	-55.90	-151.40	95.50	63.08
Tangential strain gage position [°]	*FEA* strain [µm/m]		Difference in *FEA* strains between refined optimum wheel geometry and commercial wheel model [µm/m]	Percentage difference in *FEA* strains between refined optimum wheel geometry and commercial wheel model**
	Refined optimum wheel geometry (Loading applied mid-way between two spokes)	Commercial wheel model		
0	-28.04	-205.00	176.96	86.32
90	-62.36	-145.80	83.44	57.23
180	-69.64	-151.40	81.76	54.00

*Percentage difference in FEA strains between refined optimum wheel geometry and base model determined relative to FEA strains in base model

**Percentage difference in FEA strains between refined optimum wheel geometry and commercial wheel model determined relative to FEA strains in commercial wheel model

Table 20 indicates that for refined wheel geometry with loading applied directly in-line with a spoke, the *FEA* strains at tangential orientations of 0°, 90°, and 180° were respectively determined as -1.14 µm/m, -88.50 µm/m, and -55.90 µm/m. These *FEA* strains were more compressive than those in the initial base model by -1.49 µm/m, 87.93 µm/m, and 53.44 µm/m respectively.

This means, that at a tangential orientation of 0°, the refined wheel does not deform as much as the initial base model when loading is applied directly in-line with a spoke. However, at tangential orientations of 90°, and 180°, the refined wheel deforms compressively by approximately 108 and 27 times more than the initial base model.

For loading applied exactly mid-way between two spokes, the *FEA* strains in the refined wheel model were respectively determined as -28.04 µm/m, -62.36 µm/m, and -69.64 µm/m for tangential orientations of 0°, 90°, and 180°. They were respectively more compressive than those in the initial base model by 25.41 µm/m, 61.79 µm/m, and 67.18 µm/m.

These results confirm theoretical knowledge by showing that removing material from a component reduces its stiffness. Additionally, they show that the deformation of a wheel rim does not remain constant during rotation. As such, it is important to analyse a wheels response to loading applied directly in-line with a spoke, and exactly mid-way between two spokes.

Table 20 goes on to show that for loading applied in-line with a spoke, the *FEA* strains in the refined model were respectively less compressive than those in the rim of the commercial wheel model by 203.86 µm/m, 57.30 µm/m, and 95.50 µm/m at tangential orientations of 0°, 90°, and 180°. For the same loading applied exactly mid-way between two spokes, these *FEA* strains were respectively less compressive than those in the commercial wheel model by 176.96 µm/m, 83.44 µm/m, and 81.76 µm/m.

These results show that in response to the same applied loading, the rim of the commercial wheel model would deform more than the refined model. This implies that the refined model is stiffer than the commercial wheel model, and that it should be capable of withstanding greater magnitudes of applied loading.

Additionally, the mass of the refined wheel model (3109.00 grams) is 2386.39 grams greater than that of the commercial wheel model (722.61 grams). This suggests that, as both the mass and stiffness of the refined model were greater than those of the commercial wheel, the model could have been lightened even

further during optimization. In doing so, it could be investigated whether or not structural topology optimization software alone could be utilized to produce a wheel design of lower mass and greater stiffness when compared to a commercial wheel regardless of its potential suitability for manufacture as a composite component. However, this exceeds the scope of this dissertation. As such, it is recommended as a potential topic for future research.

5.5 Chapter summary and conclusion

In this chapter, it was found that the 13.40 kg 6061-T6 aluminium alloy base model did not fail as a result of the applied loading. Additionally, it was verified by means of *FEA* software that this base model was stiffer than the commercial wheel, and that it had significant potential for design improvement.

Structural topology optimization software was utilized to generate 48 different wheel geometries from this base model. They were produced according to various combinations of objective function, safety factor, target design volume, cyclic symmetry, and split draw constraints.

Of these 48 wheel geometries, 5 met the requirements of the *Nelson Mandela University Eco Car Project*. These requirements included a minimum mass reduction of 50 percent when compared to the original base model, and a stiffness of at least 1 N/m for kilogram of component mass (specific stiffness).

These 5 wheel geometries were evaluated on the basis of mass, specific stiffness, and potential suitability for manufacture as a composite component. Ultimately, the wheel geometry produced according to a '*Maximum Stiffness*' objective function with a target design volume of 25 percent, 6 degrees of cyclic symmetry, and a *'Hole Allowed'* split-draw constraint was selected as the optimum design.

The geometry of this wheel design was further refined to enhance its suitability towards being manufactured as a composite component. During this process, its mass was increased from 2.83 kg to 3.10 kg. This corresponded to an overall decrease in mass of 10.30 kg when compared to the original base model.

FEA software was utilized to investigate whether or not this refined wheel model would fail as a result of yielding during operation. The maximum von Mises stresses corresponding to loading applied directly in-line with a wheel spoke, and exactly midway between two spokes, were determined as 47.71 MPa and 43.59 MPa respectively.

These von Mises stresses corresponded to approximately 87 and 79 percent of the 6061-T6 aluminium alloy yield strength (55.15 MPa). They indicated that that the wheel model would not fail during rotation, and confirmed that wheel rim deformation does not remain constant during rotation.

The *FEA* strain behaviour of this refined wheel model implied that it was significantly stiffer than the commercial wheel, but less stiff than the original base model. Additionally, these results confirmed that structural topology optimization software could be utilized to significantly reduce component mass, and generate a wheel geometry which could be manufactured as a composite component.

Lastly, it was noted that both the mass and stiffness of the refined wheel geometry were greater than those of the commercial wheel model. This suggested that the design could have been lightened even further during the optimization process. However, this exceeded the scope of this dissertation. As such it was recommended as a potential topic for future research.

Chapter 6: Results of wheel designs produced by composites optimization

6.1 Introduction

In the previous chapter, structural topology optimization software was utilized to produce a wheel geometry which could be optimized and manufactured as a composite component. The *FEA* strain behaviour and mass corresponding to each stage of composites optimization applied to this wheel geometry are presented in this chapter. Additionally, the corresponding physical strain and mass measurements of two wheels manufactured according to the optimized composite layup are also presented. The following themes addressed in this chapter include:

I.   The established composites optimization base model

II.   The *FEA* strain behaviour and mass of the optimized composite wheel

III.   The physical strain behaviour and mass of the optimized composite wheel

6.2 Composites optimization base model

The masses of three wheels produced through composites free size optimization are shown against those of their respective base models in *Figure 64*. These wheels were optimized according to allowable lamina angle intervals of 15°, 30°, and 60° respectively.

OPTIMIZATION BASE MODEL	FREE SIZE OPTIMIZATION	OPTIMIZATION BASE MODEL	FREE SIZE OPTIMIZATION	OPTIMIZATION BASE MODEL	FREE SIZE OPTIMIZATION
MASS: 6528 g	MASS: 454.8 g	MASS: 3273 g	MASS: 439.9 g	MASS: 1645 g	MASS: 446.5 g
(a)	15° LAMINA INTERVALS	(b)	30° LAMINA INTERVALS	(c)	60° LAMINA INTERVALS
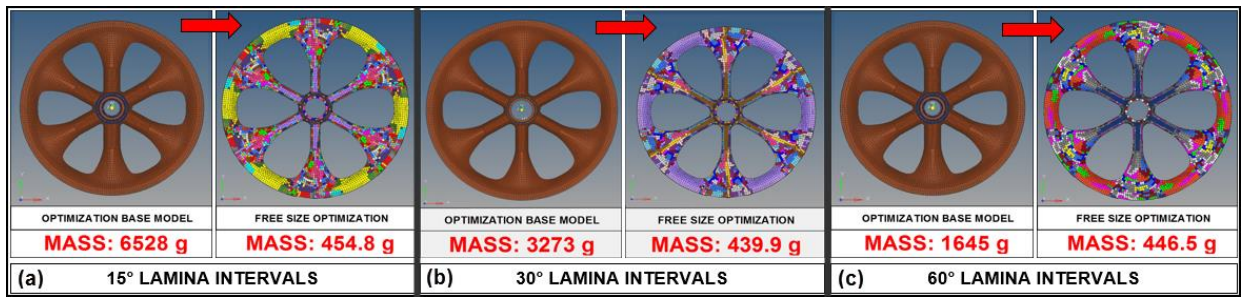
Figure 64 (a) - Masses of initial base model and corresponding wheel produced through composite free size optimization for laminae varied at 15

(b) - Masses of initial base model and corresponding wheel produced through composite free size optimization for laminae varied at 30°

(c) - Masses of initial base model and corresponding wheel produced through composite free size optimization for laminae varied at 60°

Figure 64 shows that the composite wheel base models consisting of 2 mm thick laminae stacked at respective intervals of 15°, 30°, and 60° weighed 6528, 3273, and 1645 grams respectively. Performing software based free size optimizations varied the thickness of the elements in each base model such that their respective masses were reduced by 6073.2, 2833.1, and 1198.5 grams. These differences correspond to decreases in component mass of approximately 14.4, 7.5, and 3.7 times.

Although the mass of the base model corresponding to 15° lamina intervals was reduced the most, the lightest wheel model produced through free size optimization consisted of 30° intervals. This wheel model is shown to be lighter than those generated according to lamina intervals of 15° and 60° by 14.9 and 6.6 grams respectively.

These results indicate that the range of lamina intervals allowed during composites optimization does influence the outcome of composite free size optimization. Additionally, they indicate that the lightest base model does not guarantee the lightest solution, and that the lightest solution does not necessarily correspond to the greatest number of lamina angles.

The wheel base model consisting of 30° lamina intervals was selected for further optimization in this study. The *FEA* strain behaviour of this base model is compared to those of the refined 6061-T6 aluminium alloy model (identified in the previous chapter) and commercial wheel in *Table 21*.

Table 21 - *FEA* strain behaviour of composites optimization base model compared to refined 6061-T6 aluminium alloy and commercial wheel models

Tangential strain gage orientation [°]	*FEA* strain [µm/m] (loading In-line with spoke)		Difference in *FEA* strain between Refined 6061-T6 and composite base models [µm/m]	Percentage difference of *FEA* strain between refined 6061-T6 and composite base models*
	Composite wheel base model	Refined 6061-T6 aluminium alloy model		
0	-17.41	-1.14	16.27	1427.19
90	-17.23	-88.50	71.27	80.53
180	-9.27	-55.90	46.63	83.42
Tangential strain gage orientation [°]	*FEA* strain [µm/m] (loading mid-way between two spokes)		Difference in *FEA* strain between Refined 6061-T6 and composite base models [µm/m]	Percentage difference of *FEA* strain between refined 6061-T6 and composite base models*
	Composite wheel base model	Refined 6061-T6 aluminium alloy model		
0	-27.85	-28.04	0.19	0.68
90	-11.45	-62.36	50.91	81.64
180	-8.99	-69.64	60.65	87.09
Tangential strain gage position [°]	*FEA* strain [µm/m] (loading In-line with spoke)		Difference in *FEA* strain between commercial wheel and composite base models [µm/m]	Percentage difference of *FEA* strain between commercial wheel and composite base models**
	Composite wheel base model	Commercial wheel model		
0	-17.41	-205.00	187.59	91.51
90	-17.23	-145.80	128.57	88.18
180	-9.27	-151.40	142.13	93.88
Tangential strain gage position [°]	*FEA* strain [µm/m] (loading mid-way between two spokes)		Difference in *FEA* strain between commercial wheel and composite base models [µm/m]	Percentage difference of *FEA* strain between commercial wheel and composite base models**
	Composite wheel base model	Commercial wheel model		
0	-28.04	-205.00	176.96	86.32
90	-62.36	-145.80	83.44	57.23
180	-69.64	-151.40	81.76	54.00

*Percentage difference of *FEA* strains between refined 6061-T6 and composite base models determined relative to FEA strains in refined 6061-T6 model

**Percentage difference of *FEA* strains between commercial wheel model and composite base model determined relative to FEA strains in commercial wheel model

Table 21 indicates that for a combined loading scenario applied directly in-line with a wheel spoke, the *FEA* strains in the composite base model at 0°, 90°, and 180° were compressive. Their magnitudes are respectively presented as -17.41 µm/m, -17.23 µm/m, and -9.27 µm/m. Applying the loading mid-way between two wheel spokes produced respective *FEA* strains of -27.85 µm/m, -11.45 µm/m, and -8.99 µm/min in this model at the same tangential positions.

In comparison to the 6061-T6 aluminium alloy model, the *FEA* strain in the composite base model at 0° was more compressive by 16.27 µm/m when the loading was applied directly in-line with a wheel spoke. At 90° and 180°, the *FEA* strains in the composite base model were respectively less compressive than those in the aluminium model by 71.27 µm/m and 46.63 µm/m. Applying the loading directly mid-way between two wheel spokes produced *FEA* strains in the composite base model at 0°, 90°, and 180° which were less compressive than those in the aluminium model by 0.19 µm/m, 50.91 µm/m, and 60.65 µm/m respectively.

These results show that for the composite base model, the greatest of the three *FEA* strains determined for each loading scenario corresponded to 0°. At this position, the compressive *FEA* strain was greatest when loading was applied mid-way between two wheel spokes. In the 6061-T6 aluminium alloy model, the greatest of the six recorded *FEA* strains corresponded to a tangential position of 90° when the loading was applied in-line with a spoke. This means that during rotation, the 6061-T6 aluminium alloy and composite base models deformed differently to one another in both nature and magnitude.

Additionally, *Table 21* shows that when the loading was applied in-line with a wheel spoke, the *FEA* strains in the composite base model at 0°, 90°, and 180° were respectively less compressive than those in the commercial wheel by 187.59 µm/m, 128.57 µm/m, and 142.13 µm/m. The magnitudes of these differences changed to 176.96 µm/m, 83.44 µm/m and 81.76 µm/m when the loading was applied mid-way between two of the composite base model spokes.

This implied that the composite base model was stiffer than the commercial wheel model. Additionally, these strain values implied that the composite base model was adequately stiff to allow for feasible optimization solutions to be produced. The *FEA* strain behaviour and mass corresponding to each stage of composites optimization applied to this base model are presented in the following section.

6.3 *FEA* strain behaviour and mass of the optimized composite wheel

The composite wheel masses corresponding to each stage of the composites optimization process is presented in *Figure 65*. These masses, along with the corresponding *FEA* strains at 0°, 90°, and 180° are then presented in *Table 22* for loading applied both in-line with a wheel spoke, and mid-way between two spokes.
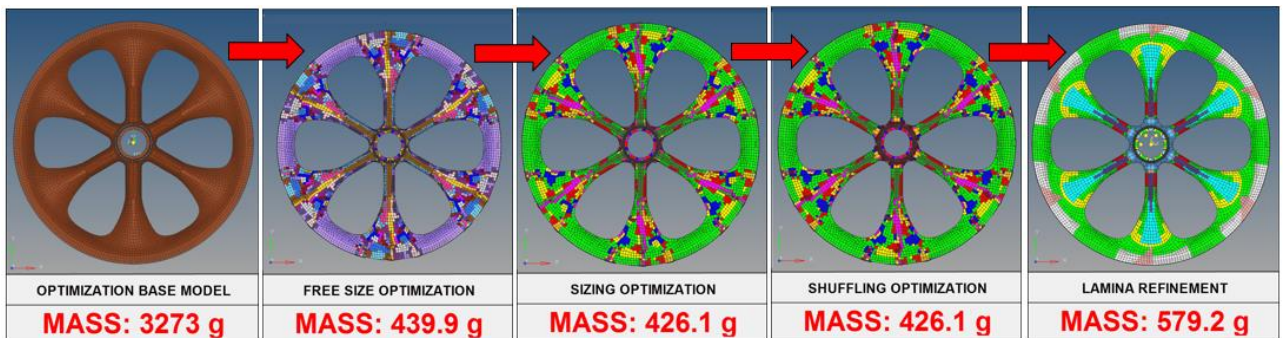
Figure 65 – Software model masses corresponding to each stage of applied composites optimization (*Altair HyperMesh*)

Table 22 – *FEA* strain behaviour of wheel models corresponding to each stage of composites optimization

Wheels corresponding to each stage of composites optimization		composite wheel base model	Wheel model produced by free size optimization	Wheel model produced by sizing optimization	Wheel model produced by shuffling optimization	Wheel model produced by manual lamina refinement
Mass [g]		3273.00	439.90	426.10	426.10	579.20
Location of applied loading	**Tangential strain gage position [°]**	*FEA* strain [µm/m]				
In-line with a wheel spoke	0.00	-17.41	-1118.00	-2332.10	-2135.00	-342.70
	90.00	-17.23	-89.00	-313.80	-306.80	-299.30
	180.00	-9.27	-209.70	-615.34	-497.60	-540.90
Mid-way between two wheel spokes	0.00	-27.85	-492.40	-2870.00	-2766.00	-727.75
	90.00	-11.45	-414.30	-1236.00	-608.40	-444.30
	180.00	-8.99	-658.10	-2041.00	-2003.00	-1044.95

The FEA strain values presented in *Table 22* imply that the stiffness of the wheel base model was reduced during free size optimization. This process resulted in the *FEA* strains at 0°, 90°, and 180° becoming respectively more compressive than those in the initial base model by 1100.59 µm/m, 71.77

µm/m, and 200.43 µm/m for a combined loading scenario applied directly in-line with a wheel spoke. These variations in *FEA* strain correspond to respective increases of approximately 64, 5, and 23 times more than the *FEA* strains in the base model (0° = -17.41 µm/m, 90° = -17.23 µm/m, 180° = -9.27 µm/m). When the loading was applied mid-way between two wheel spokes, the *FEA* strains at these tangential positions became more compressive than those in the base model by 464.55 µm/m, 402.85 µm/m, and 649.11 µm/m respectively.

These results confirm theoretical knowledge by showing that reducing component mass by decreasing cross sectional thickness produces deterioration in component stiffness. Additionally, these results confirm that changes in strain produced by free size optimization are consequential of the manner in which element thickness is varied according to the applied loading during optimization. This means that the location of maximum strain in the base model may not necessarily correspond to location of maximum strain in the solution produced by free size optimization.

Table 22 goes on to show that the mass of the composite wheel model was further reduced from 439.9 grams to 426.1 grams through composite sizing optimization. This mass reduction corresponds to 13.8 grams, and may be attributed to further variation of element thickness to resemble a realistic laminate. This means that while forming the shape of each lamina, the thickness of each element was varied to the multiple of 0.31mm which best resembled the corresponding element thickness produced during free size optimization.

Additionally, the generation of individual lamina shapes during this process appeared to further reduce the stiffness of the wheel. When loading was applied in-line with a wheel spoke, the *FEA* strains in the sizing optimization model at 0°, 90°, and 180° were respectively more compressive than those in the free size optimization model by 1214.10 µm/m, 224.80 µm/m, and 405.64 µm/m. These variations correspond to increases in compressive strain of approximately 2, 4, and 3 times more than those in the model produced by free size optimization.

When the loading was applied mid-way between two of the wheel spokes, the *FEA* strains corresponding to 0°, 90°, and 180° were reduced by sizing optimization to -2870 µm/m, -1236 µm/m, and -2041 µm/m respectively. These changes correspond to respective increases in compressive strain of approximately 6, 3, and 3 times more than those in the model produced by free size optimization (0° = -492.4 µm/m, 90° = -414.3 µm/m, and 180° = -658.1 µm/m).

These variations in strain could possibly be attributed to the sizing optimization process reducing the presence of certain fibre directions within the elements. If the material properties of a composite component remain constant, its stiffness is dependent on its geometry and laminate properties. These properties include the shape and direction of each lamina, as well as the sequence in which they are stacked. Since the thickness of each lamina is constant, reducing the thickness of an element representing a composite laminate suggests the removal of laminae. The resultant change in component stiffness is both dependent on the number of laminae removed, as well as their fibre direction. The magnitude of the corresponding change in strain is likely to be greatest if the fibre direction of the removed laminae corresponds to the direction of measured strain.

The following stage of composites optimization presented in *Table 22* corresponds to shuffling optimization. During this process, the mass of the composite wheel model was not altered, as no material was added to or removed from the model. Rather, the *FEA* strain behaviour of the model was altered through optimizing the stacking sequence of the laminae within the model.

Table 22 indicates that during this process, the *FEA* strains corresponding to an in-line loading scenario became less compressive than those in the sizing optimization model by 197.10 µm/m, -7.00 µm/m, and -117.74 µm/m at respective orientations of 0°, 90°, and 180°. Additionally, when the loading was applied mid-way between two spokes, the *FEA* strains at these orientations were respectively less compressive than those in the sizing optimization model by 104.00 µm/m, 627.60 µm/m, and 38.00 µm/m.

The manner in which the stacking sequence of the laminae was altered during this process is shown in *Figure 66*. In this figure, STACK 1 and STACK 2 refer to the laminates of the wheel body and circumference respectively. Each cell in *Figure 66* represents a single lamina. The numbers shown in each cell were generated by the optimization software.

The first three numbers in each cell represent the fibre orientation of the lamina which that cell represents. This means that the cells belonging to STACK 1 in *Figure 66*, which begin with the numbers 107, 108, 109, 111, and 112 represent laminae with respective fibre orientations of 0°, -30°, 30°, -60°, and 90°. In STACK 2, cells beginning with the numbers 214 have a fibre orientation of 0°, while those beginning with the numbers 215 have a fibre orientation of 90°. The remaining digits in each of the cells shown in *Figure 66* refer to the shape of the lamina.

Stacking sequence for STACK 1 (wheel body)

Iteration 0	Iteration 1	Iteration 2		Legend
107101	107101	107101		90.0 degrees
109201	112301	112301		30.0 degrees
107301	109201	109201		0.0 degrees
108301	108301	108301		-30.0 degrees
112301	109401	109401		-60.0 degrees
112302	107301	107301		
107401	112302	112302		
107402	109402	109402		
107403	109403	109403		
107404	109404	109404		
109401	107401	107401		
109402	112401	112401		
109403	109405	109405		
109404	109406	109406		
109405	108401	108401		
109406	107402	107402		
108401	112402	112402		
108402	108402	108402		
108403	108403	108403		
108404	108404	108404		
108405	107403	107403		
111401	112403	112403		
111402	108405	108405		
112401	111401	111401		
112402	111402	111402		
112403	107404	107404		

Stacking sequence for STACK 2 (wheel rim circumference)

Iteration 0	Iteration 1	Iteration 2		Legend
214101	214101	214101		90.0 degrees
215301	215301	215301		0.0 degrees
214401	214401	214401		
214402	215401	215401		
214403	214402	214402		
214404	215402	215402		
214405	214403	214403		
215401	215403	215403		
215402	214404	214404		
215403	215404	215404		
215404	214405	214405		
215405	215405	215405		

Figure 66 – Changes in composite laminate stacking sequences during shuffling optimization (*Altair HyperWorks*)

Figure 66 indicates that the first iteration of the shuffling optimization process produced the optimum stacking sequence for both the wheel body and circumference. During this process, the laminae were re-ordered such that no more than three consecutive plies of the same fibre direction were present in the laminate. Additionally, inspection of *Iteration 0* for STACK 1 shows that no 60° laminae were present in the solution produced during sizing optimization.

These results confirm that the sequence in which laminae are stacked in a composite component does influence the strain behaviour of the component.

Additionally, they confirm that composites optimization software may be utilized to reduce the mass of a composite component without inducing failure.

Lastly, *Table 22* indicates that by manually refining the shape of each lamina, the mass of the wheel was increased from 426.1 grams to 579.2 grams. This increase in mass resulted from the addition of elements to each lamina to eliminate small voids which would have been impractical to manufacture. The *FEA* strains at 0°, 90° and 180° are respectively presented as -342.70 μm/m, -299.30 μm/m, and -540.90 μm/m for the refined model subject to loading applied in-line with a wheel spoke. These magnitudes correspond to respective decreases in compressive *FEA* strain of 1792.3 μm/m and 7.5 μm/m at 0° and 90°. The variation in *FEA* strain at 180° indicates an increase in compressive strain of 43.3 μm/m for the same loading. Additionally, the *FEA* strains at these orientations were less compressive than those in the shuffling optimization model by 2038.25 μm/m, 164.10 μm/m, and 958.05 μm/m respectively when loading was applied mid-way between two wheel spokes.

These results show that the stiffness and mass of a software based composite model can be altered by manually editing the element selections defining each lamina. If any lamina in a model produced through composites optimization is altered, the model should be re-evaluated by means of *FEA* to check for possible failure.

The major and minor principal *FEA* strains corresponding to combined loading scenarios including pressure loads of 200 kPa and 700 kPa are respectively shown in *Table 23* and *Table 24* for the refined composite wheel model. These strains were determined using *FEA* software to check for component failure according to the unit-circle failure envelope put forward by Tsai et al [44]. The principal strains corresponding to the combined loading scenario consisting of 700 kPa inflation pressure were determined to investigate whether or not the wheel would fail if utilized with *Michelin 45/75 R16* tyres.

Table 23 – Principal composite strains determined by *FEA* for a combined loading scenario including a 200 kPa tyre inflation pressure (*Altair HyperWorks*)

Location of applied loading	In-line with a wheel spoke
Principal strain (P1)**	5168 μm/m

(a)

Location of applied loading	Mid-way between two wheel spokes
Principal strain (P1)**	5494 μm/m

(b)

Location of applied loading	In-line with a wheel spoke
Principal strain (P2)**	-7285 μm/m

(c)

Location of applied loading	Mid-way between two wheel spokes
Principal strain (P2)**	-5670 μm/m

(d)

*P1 represents principal composite strain in the fibre direction

**P2 represents principal composite strain transverse to the fibre direction

Table 24 – Principal composite strains determined by *FEA* for a combined loading scenario including a 700 kPa tyre inflation pressure (*Altair HyperWorks*)

Location of applied loading	In-line with a wheel spoke
Principal strain (P1)*	5195 μm/m

(a)

Location of applied loading	Mid-way between two wheel spokes
Principal strain (P1)*	5821 μm/m

(b)

Location of applied loading	In-line with a wheel spoke
Principal strain (P2)**	-7421 μm/m

(c)

Location of applied loading	Mid-way between two wheel spokes
Principal strain (P2)**	-5688 μm/m

(d)

*P1 represents principal composite strain in the fibre direction

**P2 represents principal composite strain transverse to the fibre direction

Table 23 (a) shows that for the combined loading scenario (consisting of a 200 kPa pressure load) applied directly in-line with a wheel spoke, the greatest magnitude of principal strain in the fibre direction was recorded as 5168 µm/m. Additionally, for this same loading scenario, the greatest magnitude of principal strain transverse to the fibre direction was recorded in *Table 23 (c)* as -7285 µm/m. When this loading was applied mid-way between two wheel spokes, these principal strains were respectively determined through *FEA* as 5494 µm/m and -5670 µm/m as shown in *Table 23 (b)* and *(d)* .

For the combined loading scenario including a 700 kPa pressure, *Table 24 (a)* indicates that the greatest magnitude of principal composite strain in the fibre direction was determined through *FEA* as 5195 µm/m. *Table 24 (c)* indicates that the greatest magnitude of principal composite strain transverse to the fibre direction was determined as -7421 µm/m for the same applied loading. Additionally, *Table 24 (b)* and *(d)* show that when this loading was applied mid-way between two wheel spokes, the corresponding principal composite strains were determined through *FEA* as 5821 µm/m and -5688 µm/m.

These results indicate that by increasing the pressure magnitude in the combined load applied in-line with a spoke by 500 kPa, the maximum major and minor principal strains in the composite wheel model became respectively more tensile and compressive by 27 µm/m and 136 µm/m. The influence of this pressure increase on the major and minor principal strains for a mid-way loading scenario corresponds to 327 µm/m and 18 µm/m respectively.

The greatest magnitudes of principal strain in the wheel rim correspond to the combined loading scenario including a 700 kPa pressure load. These magnitudes are presented on the unit-circle failure envelope in *Figure 67* and were normalized according to the respective tensile and compressive failure strains. Both of these failure strains correspond to 13000 µm/m as determined using *Normalized Trace Theory*.
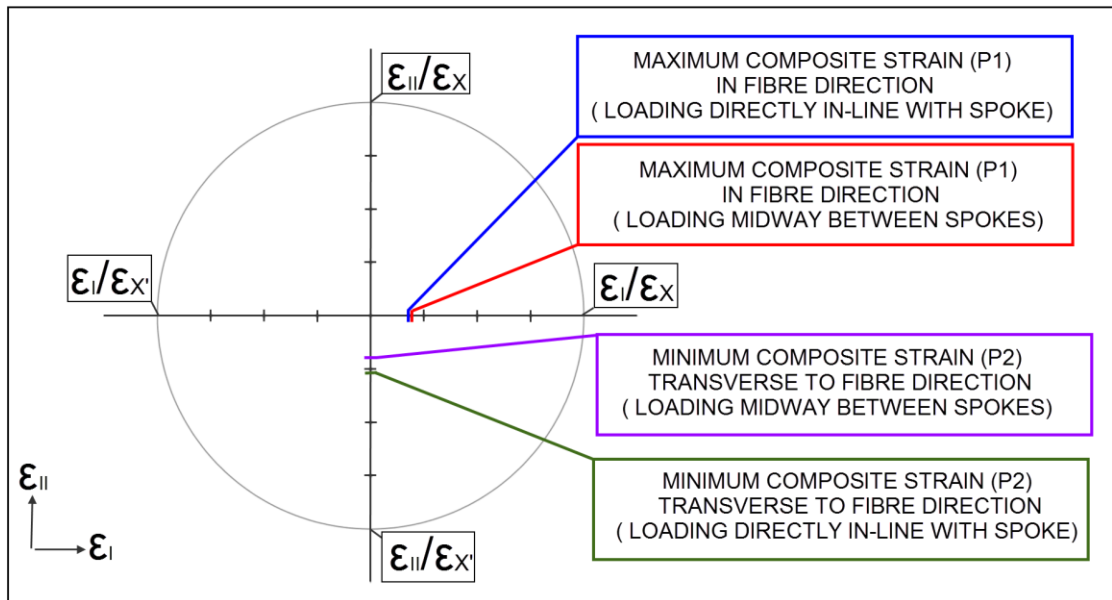
Figure 67 – Normalized maximum and minimum principal strains plotted on unit circle failure envelope

Figure 67 illustrates that the principal *FEA* strains presented in *Table 24* would not result in component failure according to the unit-circle failure envelope. This means that the optimized composite wheel should be capable of withstanding the applied loading scenario for both standard bicycle tyres and the *Michelin 45/75 R16* tyres. The physical strain behaviour of two wheels manufactured according to this composite wheel model is presented in the following section.

6.4 Physical strain behaviour and mass of the optimized composite wheel

Two wheels were physically manufactured according to the lamina shapes and stacking sequence of the refined composite wheel model discussed in the previous section. Their physically measured mass and strain behaviour are respectively compared to those of the software based model (*LAMINA REFINEMENT*) in *Table 25* and *Table 26*.

Table 25 – Comparison of masses between the manufactured composite wheels and software model

	Physically measured Mass [g]	Difference between masses of manufactured wheel and software model* [g]	Percentage difference between masses of manufactured wheel and software model**
Manufactured wheel A	652.45	73.25	12.65
Manufactured wheel B	627.60	48.40	8.36

*Mass of refined lamina software model equal 579.20 grams

** Percentage difference between masses of manufactured wheel and software model determined relative to mass of software model

Table 25 indicates that the manufactured composite wheels *A* and *B* were heavier than the software model by 73.25 and 48.40 grams respectively. These differences correspond to 12.65 and 8.36 percent of the software model mass. They suggest either the presence of excess material, or an incorrect fibre volume fraction obtained during manufacture. The presence of excess carbon fibre should cause the manufactured wheels to be stiffer than the software model. This means that the manufactured wheel *A* should be stiffer than *B*.

Physically measured strains for each of these wheels are compared to those predicted through *FEA* software in *Table 26*. These strain measurements were recorded at tangential strain gage positions of 0°, 90° and 180° for loading applied directly in-line with a wheel spoke, and exactly midway between two spokes.

Table 26 – Comparison of physically measured and *FEA* strains for both manufactured composite wheels

	Manufactured wheel A				
Location of loading	**Tangential strain gage position [°]**	**Measured physical strain [µm/m]**	***FEA* strain [µm/m]**	**Difference between measured physical and *FEA* strain [µm/m]**	**Percentage difference between measured physical and *FEA* strain***
In-line with a wheel spoke	0	-153.20	-342.70	189.50	55.30
	90	-84.60	-299.30	214.70	71.73
	180	-249.00	-540.90	291.90	53.97
Mid-way between two wheel spokes	0	-178.5	-727.75	549.25	75.47
	90	-165.8	-444.3	278.5	62.68
	180	-321.6	-1044.95	723.35	69.22
	Manufactured wheel B				
Location of loading	**Tangential strain gage position [°]**	**Measured physical strain [µm/m]**	***FEA* strain [µm/m]**	**Difference between measured physical and *FEA* strain [µm/m]**	**Percentage difference between measured physical and *FEA* strain***
In-line with a wheel spoke	0	-313.60	-342.70	29.10	8.49
	90	-285.60	-299.30	13.70	4.58
	180	-593.30	-540.90	52.40	9.69
Mid-way between two wheel spokes	0	-698.20	-727.75	29.55	4.06
	90	-470.20	-444.30	25.90	5.83
	180	-947.80	-1044.95	97.15	9.30

* Percentage difference between measured physical and *FEA* strains determined relative to *FEA* model

Table 26 shows that for loading applied directly in-line with one of wheel spokes of wheel *A*, the physical strain measurements at 0°, 90° and 180° were recorded as -153.2 µm/m, -84.60 µm/m, and -249.00 µm/m respectively. They were less compressive than those predicted using *FEA* software by 189.50 µm/m, 214.70 µm/m, and 291.9 µm/m. These differences correspond to 55.30, 71.73, and 53.97 percent of the *FEA* strain magnitudes.

When the loading was applied exactly mid-way between two of wheel *A*'s spokes, the physical strain measurements at 0°, 90° and 180° were respectively less compressive than those predicted through *FEA* software by 549.25 µm/m, 278.50 µm/m, and 723.35 µm/m. These differences represent 75.47, 62.68, and 69.22 percent of the predicted *FEA* strains.

These results indicate that wheel *A* was considerably stiffer than the optimized software model. This means that it should be capable of withstanding greater load magnitudes than what it was optimized to. Although these differences indicate greater stiffness, they violate the *FAA* acceptability criteria of 10 percent allowable strain deviation between the *FEA* model and physical

component. This means that the *FEA* did not accurately represent the manufactured wheel. Since the physical wheel was manufactured according to the *FEA*, these results suggest a flawed manufacturing process. Five possible factors contributing towards this may have included:

I.   Inaccurately cut laminae

II.   Fibre distortion during layup

III.   Inaccurately placed laminae (position of each lamina in mould)

IV.   Inaccurately aligned laminae (to either lamina template or mould)

V.   Inaccurately obtained fibre volume fraction

Since both the mass and stiffness of wheel *A* were greater than those of the computational *FEA* model, it is probable that excess carbon fibre was introduced during the manufacturing process. Excess carbon fibre could have been introduced if laminae were cut larger than their corresponding templates. This could have enhanced component stiffness by either altering the fibre volume fraction, or by increasing the wall thickness of the wheel in areas of lamina overlap.

For wheel *B*, *Table 26* shows that the physical strains at 0°, 90° and 180° were measured as -313.60 µm/m, -285.60 µm/m, and -593.30 µm/m when the loading was applied in-line with a wheel spoke. These strain measurements were respectively less compressive than those predicted through *FEA* by 29.10 µm/m, 13.70 µm/m, and -52.40 µm/m. These differences represent 8.49, 4.58, and 9.69 percent of the corresponding *FEA* strain magnitudes.

The physical strains measured at 0°, 90° and 180° in wheel *B* are shown in *Table 26* as -692.80 µm/m, -470.20 µm/m, and -947.80 µm/m for loading applied mid-way between two spokes. At 0° and 180°, these strains were respectively less compressive than those in the *FEA* model by 29.55 µm/m and 97.15 µm/m. At 90°, the physically measured strain was more compressive than the corresponding *FEA* strain by 25.9 µm/m. This means that the physical

strains at 0°, 90° and 180° differed from those predicted through *FEA* by 4.06, 5.83, and 9.30 percent respectively.

The differences between all of the physical and *FEA* strains for wheel *B* were less than 10 percent. This shows that according to the *FAA* acceptability criteria, the *FEA* model adequately represents the physically manufactured component.

Additionally, all of the physically measured strains in wheel *A* were less than those corresponding to wheel *B*. This implied that wheel *A* was stiffer than wheel *B*, and indicates that excess carbon fibre was introduced during the manufacturing process.

The measured physical strains in both of the manufactured composite wheels are compared to the *FEA* strains in the commercial wheel model in *Table 27*. The physical strains in each manufactured composite wheel were measured at tangential positions of 0°, 90° and 180° for loading applied in-line with a wheel spoke, and mid-way between two spokes.

Table 27 – Comparison of measured physical strains in manufactured composite wheels against *FEA* strains in commercial wheel model

Location of loading	Tangential strain gage position [°]	Measured physical strain in manufactured wheel *A* [µm/m]	*FEA* strain in commercial wheel model [µm/m]	Difference between measured physical strain in manufactured wheel *A* and *FEA* strain in commercial wheel model [µm/m]	Percentage Difference between measured physical strain in manufactured wheel *A* and *FEA* strain in commercial wheel model*
In-line with a wheel spoke	0	-153.20	-207.60	54.40	26.20
	90	-84.60	-146.40	61.80	42.21
	180	-249.00	-154.80	94.20	60.85
Mid-way between two wheel spokes	0	-178.50	-207.60	29.10	14.02
	90	-165.80	-146.40	19.40	13.25
	180	-321.60	-154.80	166.80	107.75

Location of loading	Tangential strain gage position [°]	Measured physical strain in manufactured wheel *B* [µm/m]	*FEA* strain in commercial wheel model [µm/m]	Difference between measured physical strain in manufactured wheel *B* and *FEA* strain in commercial wheel model [µm/m]	Percentage Difference between measured physical strain in manufactured wheel *B* and *FEA* strain in commercial wheel model*
In-line with a wheel spoke	0	-313.60	-207.60	106.00	51.06
	90	-285.60	-146.40	139.20	95.08
	180	-600.60	-154.80	445.80	287.98
Mid-way between two wheel spokes	0	-698.20	-207.60	490.60	236.32
	90	-470.20	-146.40	323.80	221.17
	180	-947.80	-154.80	793.00	512.27

* Percentage difference between measured physical and *FEA* strains determined relative to *FEA* model

In comparison to the *FEA* strains in the commercial wheel model at 0°, 90° and 180°, *Table 27* shows that the physical strains in the rim of wheel *A* were respectively less compressive by 54.40 µm/m, 61.80 µm/m, and -94.20 µm/m when loading was applied in-line with a spoke. The magnitudes of these differences correspond to 26.20, 42.21, and 60.85 percent of the respective *FEA* strains in the commercial wheel model.

For loading applied midway between two spokes, the physical strains in wheel *A* at the same strain gage positions are shown to be less compressive than those in the commercial wheel rim by 29.10 µm/m, 19.40 µm/m, and -166.80 µm/m respectively. These differences are equivalent to 14.02, 13.25, and 107.75 percent of the *FEA* strains in the rim of the commercial wheel. From these results, it appears that for both loading scenarios, the composite wheel *A* deformed less than the commercial wheel at the strain gage positions of 0° and 90°. At the strain gage position of 180°, these results indicate that for both

loading scenarios, the composite wheel *A* deformed more than the commercial wheel rim.

For the composite wheel *B*, *Table 27* indicates that the physical strains at 0°, 90° and 180° were respectively more compressive than those in the commercial wheel model by 106.00 µm/m, 139.20 µm/m, and 445.80 µm/m for loading applied in-line with a wheel spoke. Additionally, it is indicated that for loading applied mid-way between two spokes, these strains were more compressive than those in the rim of the commercial wheel model by 490.60 µm/m, 323.80 µm/m, and 793.00 µm/m. These differences correspond to 51.06, 95.08, and 287.98 percent of the corresponding *FEA* strains in the commercial wheel model for loading applied in-line with a spoke, and to 236.32, 221.17, and 512.00 percent for loading applied mid-way between two spokes.

These results imply that the composite wheel *B* was not as stiff as the commercial wheel. This means that the composite wheel deformed more than the commercial wheel in response to the applied load.

Additionally, these results show that for both loading scenarios, the greatest magnitude of physically measured strain in the rim of wheel *B* corresponded to a strain gage position of 180°. The greatest of the three compressive strain magnitudes recorded in both wheel *A* and the composite *FEA* model also corresponded to 180° for each loading scenario. Of the three strain gage positions, both the physically measured and *FEA* strains in the commercial wheel rim were greatest at 0°. This means that the commercial aluminium wheel rim deformed differently to the composite wheel rims in response to the same applied loading.

For a unidirectional lamina subject to a given load, the magnitude of strain induced in a particular direction depends on both its shape and fibre orientation if its thickness and material properties remain constant. It is possible that the position of maximum strain in a composite wheel rim may be altered if the shape and fibre orientation of its laminae are varied. This means that the manner in which a composite wheel deforms in response to a particular applied load is related its constituent ply properties.

Lastly, the masses of the software based optimized composite wheel model and the two manufactured wheels are compared to that of the commercial wheel model in *Table 28*. This comparison was performed to investigate whether or not structural topology and composites optimization techniques could be sequentially utilized to produce a manufacturable wheel of lower mass than a commercially available wheel constructed using pre-tensioned spokes.

Table 28 – Mass comparison of software based optimized composite wheel model and manufactured wheels *A* and *B* against commercial wheel model

	Mass [g]	Difference between masses of composite wheels (software based and manufactured) and commercial wheel model* [g]	Percentage difference between masses of composite wheels (software based and manufactured) and commercial wheel model**
software model of optimized composite wheel	579.20	143.41	19.846113
Manufactured wheel *A*	652.45	70.16	9.7092484
Manufactured wheel *B*	627.60	95.01	13.148171

*Mass of commercial wheel model equal to 722.61 grams
** Percentage difference between masses of manufactured wheel and software model determined relative to mass of commercial wheel model

Table 28 indicates that the software based optimized composite wheel model was lighter than the commercial wheel model by 143.41 grams. This difference corresponds to 19.85 percent of the commercial wheel mass. Additionally, *Table 28* shows that the manufactured wheels *A* and *B* respectively weighed 70.16 and 95.01 grams less than the commercial wheel model.

These results show that structural topology and composites optimization techniques can be sequentially utilized to produce a manufacturable wheel of lower mass than a commercially available wheel constructed using pre-tensioned spokes. Although the software based and manufactured optimized composite wheels were not as stiff as the commercial wheel, they were still capable of withstanding the required load magnitudes. This means that the mass of the wheels on the *Nelson Mandela University Eco Car* could be reduced by between 9.7 and 19.9 percent without negatively affecting its performance.

6.5 Chapter summary and conclusion

In this chapter, three composite wheel base models were created according to the refined wheel geometry produced through structural topology optimization in the previous chapter. These three base models were created according to 2 mm thick laminae stacked at respective fibre orientation intervals of 15°, 30°, and 60°.

The thickness of the elements in each model was varied through composite free size optimization. It was found that the solution generated according to 30° lamina orientation intervals had the lowest mass. The mass of this solution was produced as 439.9 grams, and corresponded to a decrease of 7.5 times when compared to that of the 3273 gram base model.

This showed that the outcome of composites free size optimization is influenced by the range of lamina orientation intervals specified in the base model. Additionally, they showed that the lightest solution produced by free size optimization does not always correspond to the lightest base model, or the greatest range of allowable fibre orientations.

The composite wheel base model consisting of laminae stacked at 30° fibre orientation intervals was optimized further by means of composites sizing and shuffling optimizations. In doing so, it was implied that the stiffness of a composite component may be increased by re-ordering the stacking sequence of the laminae from which it is constructed.

The lamina shapes produced during the composites optimization process would have been impractical to manufacture. As such, they were manually edited to eliminate small voids and discontinuities. This process altered both the mass and stiffness of the composite wheel model.

To investigate whether or not this alteration would result in component failure, *FEA* software was utilized to determine the principal composite strains in both the direction of the fibres, and the direction transverse to the fibres. These principal strain values were determined according to two combined loading scenarios including respective pressure loads of 200 kPa and 700 kPa. These

loading scenarios respectively represented normal operation with standard practice tyres, and *Michelin 45/75 R16* tyres. By plotting these values on a unit-circle failure envelope, it was found that the optimized composite wheel should not fail during operation.

Two wheels, *A* and *B*, were manufactured according to the lamina shapes and stacking sequence produced during the composites optimization process. The strain behaviour and mass of each of these wheels was then measured and compared to those of the software based model.

It was found that the masses of these wheels exceeded that of the software model by 12.65 and 8.36 percent respectively. This suggested that excess carbon fibre had been introduced during the manufacturing process. Additionally, this suggested that both manufactured wheels should be stiffer than the software based model, and that wheel *A* should be stiffer than wheel *B*.

The physical strain values measured in wheel *A* were considerably less compressive than those in the software based model at tangential positions of 0°, 90°, and 180°. These results showed that the strain behaviour of wheel *A* violated the acceptability criteria of 10 percent allowable deviation between *FEA* and physical strains as put forward by the *FAA*. Additionally, they suggested that the first wheel had been improperly manufactured.

The strain behaviour of wheel *B* did not violate the *FAA* acceptability criteria. This showed that it is possible to physically manufacture an optimized software component. Additionally, the physical strain values measured in this wheel rim showed that it was stiffer than the software based model, but not as stiff as wheel *B*.

Following this, the measured physical strains in the manufactured wheels were compared to those of the commercial wheel rim model. This comparison showed that the strains in wheel *A* were less compressive than those in the commercial wheel model at 0° and 90°. The strains in the rim of wheel *A* at 180° were greater than those in the commercial wheel model.

Repeating this comparison for wheel *B* showed that it was not as stiff as the commercial wheel model. Although the commercial wheel model appeared stiffer, both wheels *A* and *B* were capable of withstanding the applied loading. This confirmed that they would not fail during operation.

Comparing the masses of the software based optimized composite wheel model and physically manufactured wheels to that of the commercial wheel indicated that a mass reduction of up to 19.9 percent could be achieved through software based optimization. This showed that structural topology and composites optimization software can be utilized produce a manufacturable solution of adequate stiffness and reduced mass when compared to a commercial wheel constructed using pre-tensioned spokes.

Chapter 7: Conclusion and recommendations

7.1 Introduction

In this dissertation, structural topology and composites optimization software packages were sequentially utilized to reduce the mass of a purpose built eco-car wheel. During this process, the changes in structural integrity resulting from altering component geometry, lamina shape, and stacking sequence were investigated. This had not been done before. In addition, the supporting objectives of this dissertation were met as follows:

I.   A combined static load test rig was designed and manufactured to determine physical strains induced by actual loadings for the purpose of calibrating computational analyses

II.   A topologically optimized 6061-T6 aluminium alloy wheel geometry which did not fail when subjected to load was produced

III.   A multi-part mould for composite component fabrication was designed and manufactured

IV.   A composite wheel of the same geometry which did not fail when subjected to the same applied loading was produced

7.2 Summary and conclusions

Physical strains measured in the rim of a 722.61 gram commercial wheel were compared against those determined through *FEA* to investigate the accuracy of the strain measurements produced by means of a static load test rig, as well as how closely the methods utilized to apply *FEA* loads and constraints represented reality. These measured physical strains indicated that radial, lateral, pressure, and combined loading scenarios induced significant strains in the commercial wheel rim. Adversely, the magnitudes of the measured physical strains corresponding to torsional loading were found to be too small to record.

Some of the measured physical strains corresponding to radial and lateral loading scenarios differed from those determined through *FEA* by more than 10 percent. This indicated that according to the *FAA* acceptability criteria of 10 percent allowable deviation between *FEA* and physical strains, the static load test rig could not be utilized to measure physical strains induced by radial or lateral loading scenarios only. For pressure and combined loading scenarios, the measured physical strains in the commercial wheel rim differed from those determined through *FEA* software by less than 10 percent. This indicated that the static load test rig utilized to induce and measure physical strains could produce acceptable results for both pressure and combined loading scenarios. The magnitudes of both the measured physical and *FEA* strains were greatest for a combined loading scenario. The greatest of these strains was measured physically as -207.60 μm/m, and corresponded to a tangential strain gage position of 0°.

Structural topology optimization software was utilized to produce 48 different wheel geometries from a 13.40 kg 6061-T6 aluminium alloy base model subjected to the combined loading scenario. An *FEA* of this base model implied that it was stiffer than the commercial wheel model, and indicated that it would not fail if subjected to the combined loading scenario.

Of the 48 different wheel geometries produced using structural topology optimization software, 5 met the requirements of the *Nelson Mandela University Eco Car Team*. By evaluating these 5 wheel geometries on the basis of specific stiffness and suitability towards being manufactured as a composite component, it was identified that the optimum geometry corresponded to a *'Maximum Stiffness'* objective function with a target design volume of 25 percent, 6 degrees of cyclic symmetry, and an applied *'Hole-Allowed'* split draw constraint.

Manually refining this geometry enhanced its suitability towards being manufactured as a composite component and increased its mass from 2.83 kg to 3.10 kg. The final mass of this refined wheel geometry corresponded to a 10.29 kg decrease in mass when compared to the original base model.

The maximum von Mises stresses determined through *FEA* indicated that this refined wheel geometry would not fail when the combined loading was applied both in-line with a wheel, spoke and exactly mid-way between two spokes. These von Mises stresses were respectively determined as 47.71 MPa and 43.59 MPa.

When loading was applied in-line with a wheel spoke, the *FEA* strain in the commercial wheel rim at 0° was less compressive than the corresponding *FEA* strain in the initial base model by 1.49 µm/m. For this same loading scenario, the *FEA* strains in this wheel model were more compressive than those in the base model by 87.93 µm/m and 53.44 µm/m respectively. Comparing the *FEA* strains in this refined wheel geometry at these three strain gage positions indicated that they were more compressive than those in the initial base model by between 25.41 µm/m and 67.18 µm/m when loading was applied exactly mid-way between two wheel spokes. This strain behaviour implied that the refined wheel geometry produced through structural topology optimization was not as stiff as the initial base model. Additionally, the *FEA* strains in this refined wheel model were less compressive than those in the commercial wheel model by between 57.30 µm/m and 203.86 µm/m. This implied that this refined wheel base model was stiffer than the commercial wheel model.

Three composite wheel base models with laminae stacked at fibre orientation intervals of 15°, 30°, and 60° were created according to this refined geometry, and lightened using composite free size optimization. The lightest of these three solutions corresponded to allowable fibre orientation intervals of 30°, and a mass reduction of 7.5 times when compared to the original base model. This showed that the lightest solution produced by composite free size optimization does not necessarily correspond to the lightest base model, or the greatest range of allowable fibre orientations.

Composite sizing and shuffling optimizations were utilized to further reduce the mass of this composite wheel model to 426.10 grams. All of the *FEA* strains recorded in the solution produced through composite shuffling optimization were less than those in the solution produced using composite sizing optimization.

This implied that optimizing the stacking sequence of the laminae within the wheel model increased its stiffness.

Manually refining the element selections of each lamina in the solution produced through composite shuffling optimization made it practical to manufacture and altered both its mass and strain behaviour. The mass of this refined composite wheel model was determined as 579.20 grams, 19.85 percent lighter than the commercial wheel. It was shown by means of a unit-circle failure envelope that manually refining these laminae geometries would not cause the component to fail as a result of the applied combined loading scenario.

Two wheels were manufactured according to the lamina geometries and stacking sequences produced during the composites optimization process. The masses of these manufactured composite wheels were measured to be greater than that of the optimized software model by 12.65 and 8.36 percent, and lighter than the commercial wheel by 9.70 and 13.15 percent.

The measured physical strains in the first manufactured wheel were less compressive than the corresponding *FEA* strains by more than 10 percent. This suggested that it had been improperly manufactured. However, all of the measured physical strains in the second wheel were within 10 percent of *FEA* strains in the optimized software model. This showed that it was possible to manufacture a composite wheel according to the lamina geometries and stacking sequences produced during the composites optimization process.

In comparison to the *FEA* strains in the rim of the commercial wheel, the measured physical strains in the first wheel were less compressive at tangential strain gage positions of 0° and 90°, and more compressive at 180°. For the second manufactured wheel, all of the measured physical strains were more compressive than the *FEA* strains in the rim of the commercial wheel model by between 106.00 μm/m and 793.00 μm/m. This implied that the second manufactured composite wheel was not as stiff as the commercial wheel.

Although both the software based and manufactured optimized composite wheels appeared to be less stiff than the commercial wheel, they were capable of withstanding the intended loading resulting from operation. These results showed that structural topology and composites optimization software can be sequentially utilized to produce a manufacturable eco-car wheel which is sufficiently stiff, and lighter by up to 19.85 percent when compared to a commercial wheel constructed using pre-tensioned spokes.

7.3 Recommendations for future research

Possible recommendations for future areas of research which may expand upon the work presented in this dissertation include:

I.   Sequentially utilizing structural topology and composites optimization software to reduce the mass of a commercial automotive wheel while investigating the changes in structural integrity due to altering component geometry, lamina shape and stacking sequence

II. Investigating whether or not structural topology optimization software alone could be utilized to produce a wheel design of lower mass and equal stiffness when compared to a commercially available wheel constructed using pre-tensioned spokes

III. Investigating the influence which altering ply geometry and fibre direction has on the position of maximum strain in a wheel rim

IV. Investigating the influence which different manufacturing processes have on the correlation between measured physical and *FEA* strains for optimized composite components

V.   Investigating the fatigue and damage characteristics of a wheel designed through the sequential use of structural topology and composites optimization software packages

References

1.   Barbero E. Introduction to composite materials design. 2nd ed. Taylor and Francis Group CRC Press; 2011.

2.   Brandt J, Sheffield S. Bicycle Wheel Bicycle Wheel. Third. Avocet Inc; 2010. 139 p.

3.   Fagan M. Finite Element Analysis - Theory and Practice. PEARSON Prentice Hall; 1992.

4.   Mott R. Machine Elements in Mechnaical Design. Fourth. PEARSON Prentice Hall; 2004.

5.   Altair. Practical Aspects of Finite Element Simulation. 2015;

6.   Dorworth L, Gardiner G, Mellema G. Essentials of ADVANCED COMPOSITE FABRICATION & REPAIR. Newcastle, WA: Aviation Supplies & Academics, Inc; 2009.

7.   Gibson RF. Principles of Composite Material Mechanics. Isbn0070234515 9780070234512 [Internet]. 1994;(205):xxvii, 579 . Available from: http://www.loc.gov/catdir/toc/ecip0714/2007013616.html

8.   Eric Greene Associates. Marine Composites [Internet]. 1999. 377 p. Available from: www.marinecomposites.com

9.   Hibbeler R. Mechanics of Materials. Ninth. PEARSON; 2014.

10.   ASTM. Standard Guide for Installing Bonded Resistance Strain Gages 1. Vol. 93, Strain. 2004.

11.   Bendsoe MP, Sigmund O. Topology Optimization Theory, Methods and Applications. 2nd ed. New York: Springer; 2004.

12.   Tsai SW, Daniel J, Melo D. An invariant-based theory of composites. Compos Sci Technol. 2014;100:237–43.

13. Pacejka HB. Tire and Vehicle Dynamics. Second. Warrendale: Society of Automobile Engineers, Inc.; 2006.

14. Jape RK, Jadhav SG. CAD Modeling and FEA Analysis of Wheel Rim for Weight Reduction. Int J Eng Sci Comput. 2016;6(6):7404–11.

15. Prasad TS, Krishnaiah T, Iliyas J, Reddy MJ. A Review on Modeling and Analysis of Car Wheel Rim using CATIA & ANSYS. 2014;(6):2–6.

16. Keller J. Optimisation of the Spoked Bicycle Wheel. 2013;

17. Paropate SM, Deshmukh SJ. Modelling and Analysis of a Motorcycle Wheel Rim. Int J Mech Eng Robot Res. 2013;2.

18. Kumar CPVR, Meher PRS. Topology Optimization of Aluminium Alloy Wheel. 2013;3:1548–53.

19. Maserumele LF. Design of a carbon fibre passanger car rim. University of the Witwatersrand; 2015.

20. Sabri M, Rezal M, Mu A, Shahril K, Ihsan J. Deformation Behaviour Analysis Of Car Wheel Rim Under Different Loading Using Finite Element Method. Int J Eng Technol. 2015;5(3):181–4.

21. Koch N. Shell Eco-Marathon 2016 Official Rules. 2015;51. Available from: http://s06.static-shell.com/content/dam/shell-new/local/corporate/ecomarathon/downloads/pdf/global/sem-2016-global-rules-chapter1-010715.pdf

22. Santin JJ, Onder CH, Bernard J, Isler D, Kobler P, Kolb F, et al. THE WORLD'S MOST FUEL EFFICIENT VEHICLE DESIGN AND DEVELOPEMENT OF PAC CAR 2. 1st ed. Zurich: vdf Hochschulverlag AG an der ETH Zurich; 2007.

23. Borase K, Deore E. Studying Effect of Pressure on Rim Introduction : Effect of Tyre Air Pressure on Rim : Finite Element Analysis of Automobile Wheels : Int J Innov Res Multidiscip F. 2016;2(6):95–9.

24. Doyle M. The Design of an aluminium alloy wheel using three dimensional Finite Element Analysis and Fatigue Life Prediction . 1996.

25. Patel H, Satankar K. Failure analysis of steel wheel by using finite Element Method. Int J Res Aeronaut Mech Eng. 2014;2(6):106–15.

26. Das S, Analyst CAE. Design and Weight Optimization of Aluminium Alloy Wheel. 2014;4(6):1–12.

27. Hong HT, Chun HJ, Choi HS. Optimal strength design of composite bicycle wheels. Int J Precis Eng Manuf. 2014;15(8):1609–13.

28. Akin JE. Finite Element Analysis Concepts via SolidWorks [Internet]. 2009. Available from: https://www.clear.rice.edu/mech517/old_pdf/FEAC_final.pdf

29. Aviation F. Finite Element Modeling and Analysis Validation. (425).

30. Radha KK, Kumar GS, Babu JPR. Modeling and Structural Analysis of Alloy Wheel Using COSMOS. 2015;2(3):1–6.

31. Mariappan DD, Vijay S, Ramamurti V. An efficient algorithm for solving spoked wheels. Adv Eng Softw. 2003;34(1):25–30.

32. Xiao D, Zhang H, Liu X, He T, Shan Y. Novel steel wheel design based on multi-objective topology optimization. J Mech Sci Technol. 2014;28(3):1007–16.

33. Kalyanasundaram S, Lowe a., Watters a. J. Finite element analysis and optimization of composite wheelchair wheels. Compos Struct. 2006;75(1–4):393–9.

34. Siefert H, Threlfall W. SEIFERT AND THRELFALL: A TEXTBOOK OF TOPOLOGY AND SIEFERT: TOPOLOGy OF 3-DIMENSIONAL FIBERED SPACES. Vol. 7. New York: ACADEMIC PRESS, INC; 1980. 956-963 p.

35. Zhou M, Fleury R, Patten S, Stannard N. Topology Optimization-Practical Aspects for Industrial Applications. 9th World Congr Struct Multidiscip Optim [Internet]. 2011;1–10. Available from: http://scholar.google.com/scholar?hl=en&btnG=Search&q=intitle:Topology+Optimization+-+Practical+Aspects+for+Industrial+Applications#8

36. Mylett D, Gardner S. Principle Roll Structure Design Using Non-Linear Implicit Optimisation in Radioss. 2011;1–8.

37. Guest J, Lotfi R, Gaynor A, Jalalpour M. Structural Topology Optimization: Moving Beyond Linear Elastic Design Objectives. 20th Anal Comput Spec Conf [Internet]. 2012;245–56. Available from: http://ascelibrary.org/doi/abs/10.1061/9780784412374.022

38. Academic Program: Practical Aspects of Structural Optimization. 2nd ed. Altair University; 2015.

39. Brackett D, Ashcroft I, Hague R. Topology optimization for additive manufacturing. Solid Free Fabr Symp. 2011;348–62.

40. Satya Prasad BGN, Anil Kumar M. Topology Optimization of Alloy Wheel. Altair Technol Conf. 2013;1–7.

41. Degenhardt R, Castro SGP, Arbelo MA, Zimmerman R, Khakimova R, Kling A. Future structural stability design for composite space and airframe structures. Thin-Walled Struct [Internet]. 2014;81:29–38. Available from: http://dx.doi.org/10.1016/j.tws.2014.02.020

42. Zhou M, Patten S, Kemp M, Yancey R, Mestres E, Mouillet J. Applications of Advanced Composite Simulation and Design Optimization. Altair Eng. :1–14.

43. Gay D, Hoa S. Composite Materials. Boca Raton, Florida: CRC Press; 2007.

44. Tsai SW, Daniel J, Melo D. A unit circle failure criterion for carbon fi ber reinforced polymer composites. Compos Sci Technol. 2016;123:71–8.

45. Stegmann J, Lund E. Discrete material optimization of general composite shell structures. Int J Numer Methods Eng [Internet]. 2005 Apr 14 [cited 2016 Jan 13];62(14):2009–27. Available from: http://doi.wiley.com/10.1002/nme.1259

46. Zhou M, Fleury R, Dias W. Composite Design Optimization- from Concept to Ply-Book Details. 8th World Congr Struct Multidiscip Optim. 2009;1–8.

47. Chen S, Lin Z, An H, Huang H, Kong C. Stacking sequence optimization with genetic algorithm using a two-level approximation. Struct Multidiscip Optim. 2013;48(4):795–805.

48. Toropov V V, Jones R, Willment T, Funnell M. Weight and Manufacturability Optimization of Composite Aircraft Components Based on a Genetic Algorithm. Proc 6th World Congr Struct Multidiscip Optim. 2005;(June).

49. Huang X, Zhou SW, Xie YM, Li Q. Topology optimization of microstructures of cellular materials and composites for macrostructures. Comput Mater Sci. 2013;67:397–407.

50. Allaire G, Delgado G. Stacking sequence and shape optimization of laminated composite plates via a level-set method. arXiv. 2015;1–33.

51. Pedersen P. On thickness and orientational design with orthotropic materials. Struct Optim. 1991;3(2):69–78.

52. Funnell M. Targeting Composite Wing Performance – Optimum Location of Laminate Boundaries. 2007;1–15.

53. Patten S. Targeting Composite Wing Performance – Optimising the Composite Lay-Up Design. 2009;1–15.